University of Alberta

An Enclosed Turbulent Jet Near a Solid Wall: Initial Flow Development

by

Kevin Ness

A thesis submitted to the Faculty of Graduate Studies and Research in partial fulfillment of the requirements for the degree of Master of Science.

Department of Mechanical Engineering

Edmonton, Alberta

Spring 2007

Canada

Abstract

LDV measurements were taken of a turbulent jet inside an enclosure. Measurements were taken in the development region of the turbulent jet at the varying downstream stations. The enclosure fixed the position of the jet but contained a moveable interior wall. Measurements were taken with the wall at three different positions relative to the jet exit. The jet being studied had an exit Reynolds number of 20000.

It was found that the turbulent jet studied in this thesis shared some characteristics with a free jet. One of these similarities was that the eddy viscosity is constant across the jet being studied. It was also found to differ from free jets. Most notably it was found at 20 diameters downstream the jet only had 53% of its initially supplied momentum thus failing to satisfy the integrated momentum equation. This result is commonly seen in confined jets because of the recirculation that occurs inside the enclosure. Further analysis of the experimental results also indicates that the jet contained a mild amount of swirl.

Table of Contents

List of Figures

Nomenclature

d	jet exit diameter (m)
f	frequency (Hz)
h	distance from wall to jet centerline (m)
g	acceleration due to gravity (m/s^2)
p	pressure (N/m^2)
t	time (s)
U	mean velocity in x direction (m/s)
V	mean velocity in y direction (m/s)
u'	turbulent velocity in x direction (m/s)
v'	turbulent velocity in y direction (m/s)
x_o	virtual origin of jet (m)
ρ	density (kg/m^3)
τ	shear stress (N/m^2)
μ	viscosity (kg/m•s)
ν	kinematic viscosity (m^2/s)

Chapter 1: Introduction

1.1 Background

Problems in Fluid Mechanics can be explained by three sets of linked equations: Mass Conservation, Energy Conservation & the Momentum equation. For an incompressible flow, the instantaneous continuity (mass conservation) equation can be expressed as

$$\frac{\partial u}{\partial x} + \frac{\partial v}{\partial y} + \frac{\partial w}{\partial z} = 0 \tag{1.1}$$

where u is the instantaneous velocity in the x direction, v is the instantaneous velocity in the y direction, and w is the instantaneous velocity in the z direction. The momentum equation (used together with the assumption that viscous stresses are proportional to strain rate and the coefficient of viscosity) can be expressed as the differential Navier Stokes equations: These equations are

$$\rho g_x - \frac{\partial p}{\partial x} + \mu\left(\frac{\partial^2 u}{\partial x^2} + \frac{\partial^2 u}{\partial y^2} + \frac{\partial^2 u}{\partial z^2}\right) = \rho\frac{du}{dt} \tag{1.2a}$$

$$\rho g_y - \frac{\partial p}{\partial y} + \mu\left(\frac{\partial^2 v}{\partial x^2} + \frac{\partial^2 v}{\partial y^2} + \frac{\partial^2 v}{\partial z^2}\right) = \rho\frac{dv}{dt} \tag{1.2b}$$

$$\rho g_z - \frac{\partial p}{\partial z} + \mu\left(\frac{\partial^2 w}{\partial x^2} + \frac{\partial^2 w}{\partial y^2} + \frac{\partial^2 w}{\partial z^2}\right) = \rho\frac{dw}{dt} \tag{1.2c}$$

If there are no density variations in the flow, which is the case for the isothermal liquid studied in this thesis, there is no coupling between the energy equation and the continuity - momentum conservation equations given above.

The velocities given above (u, v and w) are instantaneous velocities. In most engineering problems the flow field being studied is turbulent. This is due to the low critical Reynolds number at which a flow regime undergoes a transition from laminar to turbulent flow. A flow's Reynolds number is a measure of the relative magnitude of its inertial forces compared with the internal viscous forces. The viscous forces in a flow can be thought of as stabilizing forces while the inertial forces are destabilizing forces within a flow.

For an arbitrary flow its destabilizing inertial force is a function of the fluid's density (ρ), the average velocity of the flow (V), and a characteristic length (D).

$$F_{inertial} \sim \rho V^2 D^2 \tag{1.3}$$

The viscous forces present in a flow of a Newtonian fluid can be thought of as the product of the shear stress in the flow (τ) and the area over which this force acts (A).

$$F_{viscous} = \tau A \tag{1.4}$$

2

Considering a Newtonain Fluid, the shear stress can be approximated by $\tau = \mu \dfrac{dV}{dy}$,

and the area A can be assumed proportional to D^2. The above substitutions can now

be made in Equation 1.4 to yield

$$F_{viscous} \sim \left(\mu \frac{dV}{dy} \right) D^2 \qquad (1.5)$$

Finally the differential $\dfrac{dV}{dy}$ can be scaled by $\dfrac{V}{D}$. The ultimate result for $F_{viscous}$ is

shown below.

$$F_{viscous} \sim \left(\mu \frac{V}{D} \right) D^2 \sim \mu V D \qquad (1.6)$$

To determine Reynolds number the ratio of the inertial and viscous forces must now

be taken. Dividing Equation 1.3 by Equation 1.6 give us

$$\text{Re} \sim \frac{F_{inertial}}{F_{viscous}} = \frac{\rho V^2 D^2}{\mu V D} = \frac{VD}{v} \qquad (1.7)$$

1.2 Reynolds Velocity Decomposition

Turbulent flows are characterized by rapid fluctuations in a flows instantaneous

velocity at any given point. Osborne Reynolds suggested decomposing the

3

instantaneous velocity into two components; the mean velocity and fluctuating
velocity. In this regard u, v and w can be expressed as

$$u = u' + \overline{u} \qquad (1.8a)$$

$$v = v' + \overline{v} \qquad (1.8b)$$

$$w = w' + \overline{w} \qquad (1.8c)$$

where $\overline{u}$, $\overline{v}$ and $\overline{w}$ are the time averaged mean velocities given by the following
definition

$$\overline{u} = \lim_{t \to 0} \left(\frac{1}{T} \int_0^T u \, dt \right) \qquad (1.9a)$$

$$\overline{v} = \lim_{t \to 0} \left(\frac{1}{T} \int_0^T v \, dt \right) \qquad (1.9b)$$

$$\overline{w} = \lim_{t \to 0} \left(\frac{1}{T} \int_0^T w \, dt \right) \qquad (1.9c)$$

In order for this definition of time average mean velocity to be useful, the period T
over which the average is taken must be considerably larger than the period of the
turbulent fluctuations being considered. The variables u', v' and w' are the turbulent
velocities that fluctuate about the mean velocity. It should be noted that
$$\overline{u'} = \overline{v'} = \overline{w'} = 0$$

Substitution of the above 'decomposed' velocities into the continuity Equation (1.1)
gives the following

4

$$\frac{\partial \bar{u}}{\partial x} + \frac{\partial \bar{v}}{\partial y} + \frac{\partial \bar{w}}{\partial z} = 0 \qquad (1.10)$$

It can be seen that Equation 1.10 is identical to the laminar version of the continuity equation. However, this is not the case for the momentum equation. When the Reynolds decomposed velocities (1.8) are substituted into the Navier Stokes Equations (1.2) the following result is seen:

$$\rho\left(\frac{D\bar{u}}{Dt} + \frac{\partial \overline{u'^2}}{\partial x} + \frac{\partial \overline{u'v'}}{\partial y} + \frac{\partial \overline{u'w'}}{\partial z}\right) = -\frac{\partial \bar{p}}{\partial x} + \mu\left(\frac{\partial^2 u}{\partial x^2} + \frac{\partial^2 u}{\partial y^2} + \frac{\partial^2 u}{\partial z^2}\right) \qquad (1.11a)$$

$$\rho\left(\frac{D\bar{v}}{Dt} + \frac{\partial \overline{u'v'}}{\partial x} + \frac{\partial \overline{v'^2}}{\partial y} + \frac{\partial \overline{v'w'}}{\partial z}\right) = -\frac{\partial \bar{p}}{\partial y} + \mu\left(\frac{\partial^2 v}{\partial x^2} + \frac{\partial^2 v}{\partial y^2} + \frac{\partial^2 v}{\partial z^2}\right) \qquad (1.11b)$$

$$\rho\left(\frac{D\bar{w}}{Dt} + \frac{\partial \overline{u'w'}}{\partial x} + \frac{\partial \overline{v'w'}}{\partial y} + \frac{\partial \overline{w'^2}}{\partial z}\right) = -\frac{\partial \bar{p}}{\partial x} + \mu\left(\frac{\partial^2 u}{\partial x^2} + \frac{\partial^2 u}{\partial y^2} + \frac{\partial^2 u}{\partial z^2}\right) \qquad (1.11c)$$

Equation 1.11a, b and c contain the terms $\overline{u'^2}$, $\overline{v'^2}$, $\overline{w'^2}$, $\overline{u'v'}$, $\overline{u'w'}$ and $\overline{v'w'}$. These terms are referred to as Reynolds stresses or turbulent stresses. Although these terms have the units of stress when multiplied by ρ, they are not actually stresses. They are convective acceleration terms but have the same effect as stresses from a mathematical standpoint. In most literature these terms are referred to as Reynolds stresses so this Thesis will use the same terminology.

5

1.3 Self Similarity

Self similarity is a concept that requires relevant mean velocities (U and V) as well as the Reynolds stresses ($\overline{u'^2}$, $\overline{v'^2}$ and $\overline{u'v'}$) all to scale with the same local mean velocity scales as the flow evolves downstream (for example the local jet centerline velocity and the downstream distance). The mean flow velocities U and V become self similar long before the Reynolds stress terms. From a theoretical standpoint (Tennekes and Lumley 1997), the normal stresses $\overline{u'^2}$ and $\overline{v'^2}$ should become self similar after the mean velocities. The shear stress term $\overline{u'v'}$ will then become self similar after the normal stresses. The third order moments then follow suit. It should be noted that when a flow is in its self similar state, the primary link between the mean flow and the turbulence is through the turbulence production term, $\mathcal{P}$, given by the following equation

$$\mathcal{P} = -\overline{u'v'}\frac{\partial U}{\partial y} - (\overline{u'^2} - \overline{v'^2})\frac{\partial U}{\partial x} \tag{1.12}$$

1.4 The Axisymmetric Jet

An axisymmetric jet is a flow field that has been extensively studied in the area of fluid mechanics. A schematic of a free axisymmetric jet is shown in Figure 1.1.

6
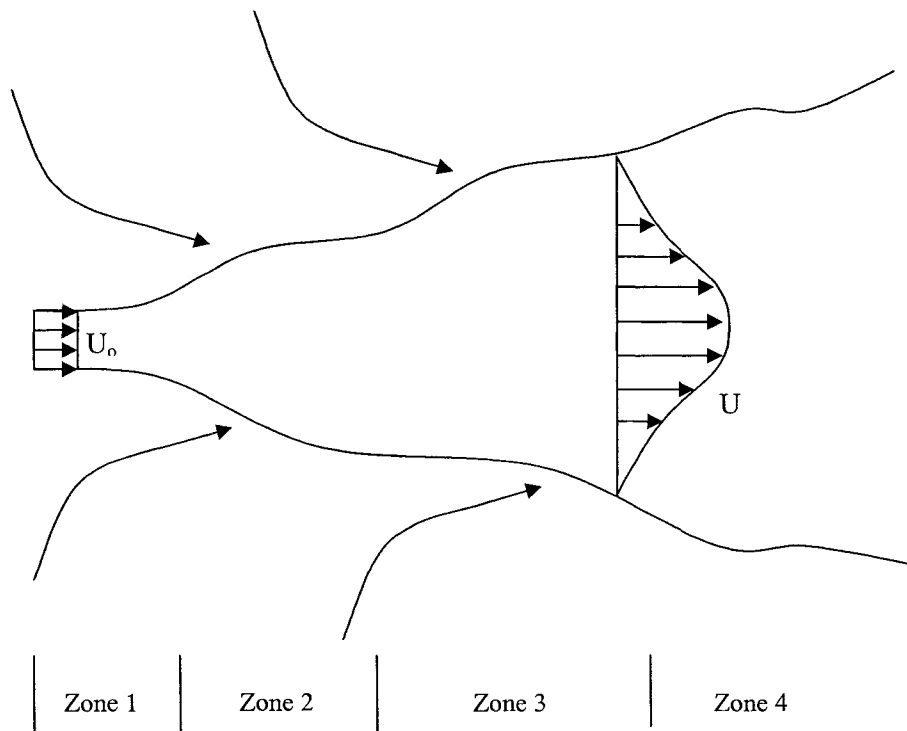
Figure 1.1: A schematic of an axisymmetric free jet.

A turbulent jet consists of four main zones (Yue 2002). Zone 1 is closest to the exit of the nozzle and contains the potential core of the jet. The potential core is a region where the velocity of the jet remains equal to the exit velocity. This core of fluid gets smaller in diameter as the fluid moves downstream which results in the core having a cone shape. This development region can be thought of as a cylindrical mixing layer with the outside having the velocity of the free stream fluid and the inside have the velocity of the jet exit. This mixing layer grows until the inside layer combines with itself on the opposite side of the jet. This results in the termination of the potential core region. Zone 2 is known as the transitional zone. This transition zone is characterized by a velocity decay that is often approximated as being proportional to

7

$x^{-0.5}$. The third zone is typically the main region of interest inside the jet. Zone 3 is known as the self similar region because normalized velocity profiles collapse on each other in this region. Centerline velocity decay is ideally proportional to x^{-1} inside of the self similar region. This decay is notably faster than the decay in the transition region. The fourth zone is called the termination zone. This zone is where the centerline velocity begins rapid decay as the jet degenerates & combines with its surroundings.

Figure 1.2 shows a schematic of a wall jet. A wall jet has been defined as "a shear flow directed along a wall where, by virtue of the initially supplied momentum, at any station, the streamwise velocity over some region within the shear flow exceeds that in the external stream" (Tachie Balachandar and Bergstrom 1999). The wall jet is fundamentally different from the free jet because it issues along a wall parallel to the mean flow direction. A wall jet can be broken up into two different layers. The inner layer, which is in contact with the wall, behaves like a turbulent boundary layer, while the outer layer more closely resembles a free jet. There are different approaches to determining the transition point between the inner and outer layer. The most common approach is to define the inner layer to begin at the wall and terminate at the point of maximum velocity. Another approach defines the inner layer to extend from the wall to point where the Reynolds shear stresses are zero (Kruka & Eskinazi, 1964). In a free jet, the point at which Reynolds shear stresses are zero coincides with the point of maximum velocity. In a wall jet this is not the case. The point where the shear stress disappears is closer to the wall.

8

$\overline{u'v'} = 0$

Outer Layer

$U = U_{max}$

Inner Layer
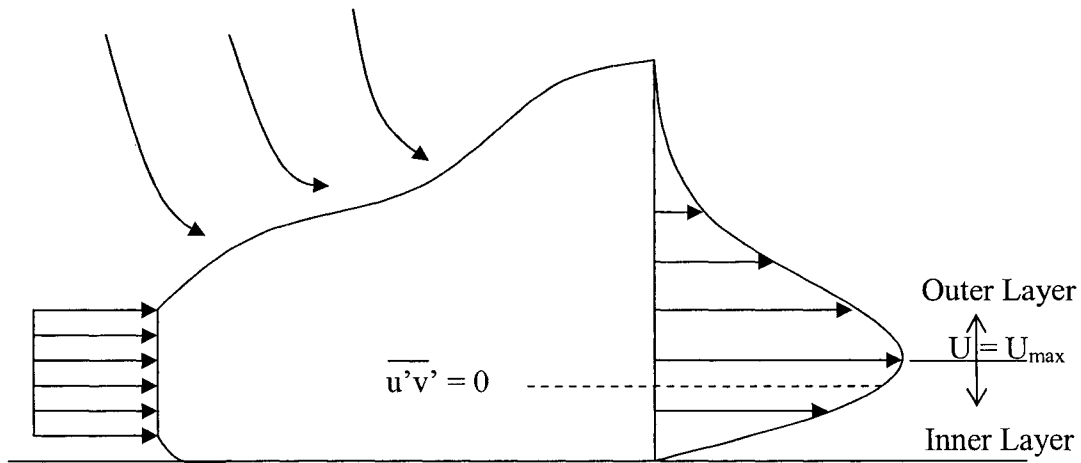
Figure 1.2: A schematic of a wall jet

A jet inside an enclosure is what is studied in this thesis. A schematic diagram of an enclosed jet is shown in Figure 1.3. A jet inside an enclosure has characteristics of both a free jet and a wall jet. One characteristic of the enclosed jet is that there is a reverse flow which does not occur when a jet is in an 'infinite' environment. This flow reversal "steals momentum from the jet, and thereby progressively modifies it from the jet which would be observed in an infinite environment."(Hussein, Capp and George 1994). Another way in which the enclosure affects the jet is known as the Coanda effect. The Coanda effect is a phenomenon where a jet is drawn toward the wall of an enclosure. This is caused by the wall retarding entrainment of free stream fluid on the side of the jet closest to the wall. This results in a momentum imbalance caused by more fluid being entrained on the 'free' side of the jet. The jet is then pushed towards the wall by this momentum imbalance.

9
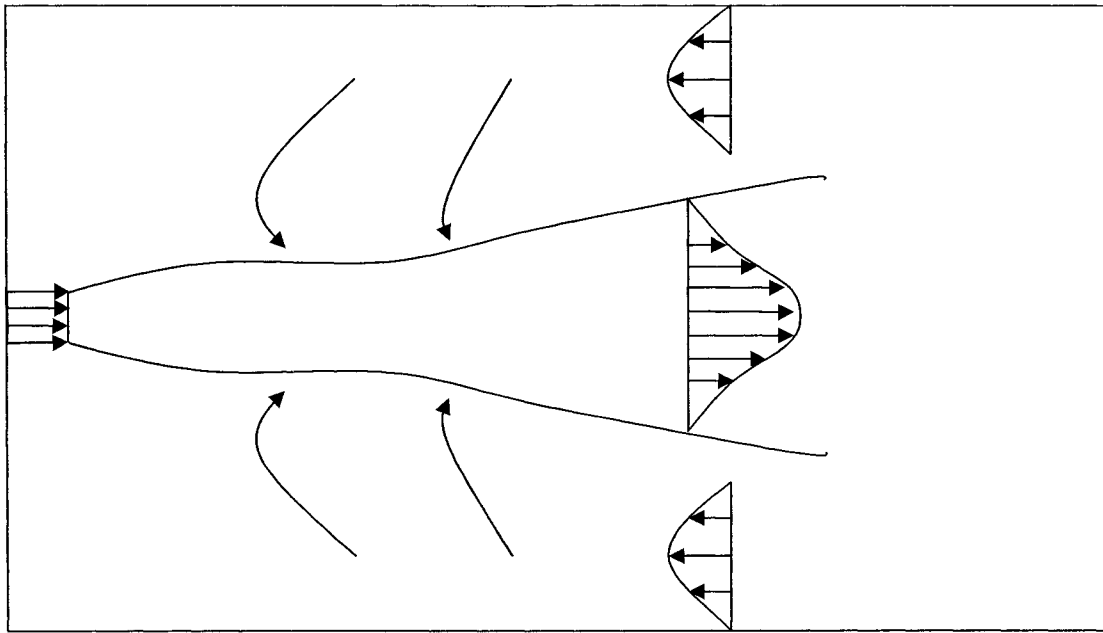
Figure 1.3: A schematic of an enclosed jet.

1.5 Objectives

The objectives of this research project are as follows:

i. The first objective of this research project was to construct and test a confined jet apparatus which could be used in this project as well as by future researchers. The apparatus had to be suitable for use with optical measurement techniques such as an LDV

ii. Another objective of this project was to take accurate velocity measurements of a jet inside an enclosure. Of particular interest was the effect that a moveable wall inside the enclosure had on turbulence statistics such as the Reynolds shear stress and turbulent kinetic energy. Most data that have been taken in the past used invasive methods like hot wire anemometry which

10

suffers the problems of poor spatial resolution, ambiguity in determining flow direction, as well as slow time response.

iii. Benchmark data were desired for future work involving jets in enclosures. (Because of the physical limitations of the apparatus, measurements close to the wall had to be taken in the X-Y (wall-parallel) plane while the traverse was moved in the (wall-normal) Z-direction.)

iv. Determine a range of dimensions and parameter space within which this system behaves as a free jet.

11

Chapter 2: Literature review

The work presented in this thesis represents the initial study of turbulent jets inside enclosures being undertaken in this Mechanical Engineering Department. Previous work done here has focused on scalar concentration measurements inside of turbulent jets.

Previous work at the University of Alberta in the Civil Engineering Department carried out by Rajaratnam and Pani (1970) dealt with studying wall jets. The studies by Rajaratnam are fundamentally different than the one presented here because in those studies the potential core of the jet immediately interacted with the enclosure wall. This is because the jet issued along the bottom of the tank and the bottom wall of the tank was also the bottom wall of the nozzle. In Rajaratnam's work it was found that the circular jet tested exhibited self similarity after 16 diameters downstream. Rajaratnam also made observations of the wall shear stress in the central plane of the jet.

The research of Yue (2002) involved studying wall jets where the nozzle was a fixed distance from an adjacent wall. In this work a constant temperature hot wire probe was used to take velocity measurements in the self similar region of the wall jet. Yue was primarily concerned with centerline velocity values and did not provide turbulence statistics in the self similar region that was studied. Yue also did not discuss the spreading mechanisms of the jets that were studied.

12

In the work of Ewing & Hongguang (2002), detailed flow field measurements inside wall jets were carried out. The primary motivation behind the work of Ewing was to determine what role initial, as well as boundary, conditions play in the development of turbulent three dimensional wall jets. They found that the jet exit Reynolds number had no significant effect on the growth of a fully developed turbulent jet for $Re_D > 65000$, the lowest value tested. They did find however that the shape of the exit velocity profile plays an important role in the downstream spreading of the jet. Ewing tested jets created using a contoured nozzle as well as a straight pipe. The contoured nozzle created a top hat exit velocity profile. This initial top hat profile was found to promote jet spreading in the near field of the wall jet. It was also found that the presence of a back wall flush mounted to the jet had little or no influence on jet characteristics for $x/d > 10$. In the near field it was found that a jet without a back wall was able to spread more quickly. This result can be attributed to the enhanced entrainment available to the jet when the back wall is removed. The jet used by Ewing was a true wall jet with the bottom wall of the enclosure immediately against the bottom of the nozzle.

In the work of Hussein, Capp and George (1994) detailed LDA and hot wire measurements were taken of an axisymmetric turbulent jet inside of a large room. Their results were found to satisfy both the second order integral and differential forms of the momentum equation for a free axisymmetric turbulent jet. This is in contrast to the earlier works of Wygnanski & Fiedler (1969) which were shown by Baker (1980) to not satisfy the integrated axial momentum equation in the far field of

13

the jet. The work of Capp (1983) found that this discrepancy in the Wygnanski & Fiedler data was a facility related problem. The facility used by Wygnanski & Fiedler was only semi-infinite since the axial momentum equation failed to be satisfied due to the entrainment of recirculating flow. This recirculating flow would not have been present in an infinite environment. Hussein et al. used two different types of hot wires when taking measurements, a stationary and a flying hot wire. They found the accuracy of the stationary hotwire was poor compared to the flying hotwire or LDA. Hussein also cautioned against trusting earlier works because of either enclosure effects, which were not taken into account, or the prevalence of stationary hot wire anemometers. The work of Hussein et al. was used a benchmark for the work presented in this thesis from both a procedural standpoint and as a standard for comparison of raw data.

In Ewing (2002) large scale structures inside turbulent wall jets were studied in the areas between $x/d = 15$ to $x/d = 40$. In this work Ewing shows that large scale double horseshoe structures evolved in this region and played an important role in the development of the flow downstream. Ewing goes on to explain how these horseshoe structures interact with each other as well as the adjacent wall to help promote spreading in the lateral direction.

In the work of Erikson, Karlsson et. al. (1998) a complete and comprehensive dataset of mean velocities and turbulent structure is presented for the wall jet studied in an earlier work by Karlsson (1993). In this paper a wall jet with an exit Reynolds

14

number of 9600 was studied using a similar TSI two component LDA as was used in the work presented in this thesis. Wall shear stress was calculated by calculating the mean velocity gradient in the area below $y^+=4$. Shear stress was also determined using measurements taken with a hot wire anemometer. The hot wire measurements yielded a wall shear stress which was considerably lower than the stress calculated using the LDA. This was attributed to the fact that the hot wire could not get as close to the wall as the LDA. Thus the hot wire measurements were taken outside the viscous sublayer where the velocity profile is no longer linear. This illustrates another example of why optical measurement techniques like LDA are superior to invasive methods like hot wire anemometry. Their results are consistent with momentum conservation up to $x/d = 150$

Tachie, Balachandar and Bergstrom (1999) have written a review of recent literature regarding co-flow and counter flow wall jets. In this review some applications of wall jets are given. One of the main conclusions they reach is that using the velocity gradient at the wall is a much more suitable method for calculating wall shear stress than the Clauser method which relies on curve fitting the log region. This is because of the variability in the log-law constants found in past work. This variability shows that the wall jet does not have a well defined log-law region like the turbulent boundary layer. They go on to detail how LDA measurements can be used to develop wall skin friction correlations because of their ability to resolve directional uncertainty and excellent spatial resolution. Another conclusion of Tachie et al. is that scaling of turbulence statistics has been a consistent problem in recent near-wall

15

measurements taken by other researchers. The most common method of scaling second and third moments is to use the jet centerline velocity. The problem with this method is that the moments and the centerline velocity have different rates of decay with downstream distance. Another method that is used is to scale the second order moments with the $\overline{u'v'}_{max}$, while another method uses the jet exit velocity to normalize the downstream turbulent moments.

Hammad and Sherkarriz (1998) studied turbulence in confined axisymmetric jets. This study considered both Newtonian and non-Newtonian fluids. More specifically they investigated the effect of Reynolds number and confinement geometry on turbulence within axisymmetric jets. Measurements were taken at downstream distances from the nozzle ranging from $x/d = 10$ to 100. Reynolds numbers, based on exit diameter, were varied between $Re_D = 2000$ up to a maximum Reynolds number of 10^5. The measurements that were taken show that the centerline turbulence levels in the axial direction approach an asymptotic value and eventually become independent of Reynolds number. This independence occurs at a critical Reynolds number of 10^4. It should also be noted that Hammad and Sherkarriz found that the turbulence kinetic energy measurements they made in Newtonian fluids were higher than earlier measurements of free jets. This same result was not found to be the case for non-Newtonian fluids. When non-Newtonian jets were examined, the results were found to be consistent with Newtonian free jets. This result means that confinement geometry does not have the same effect on jets of non-Newtonian fluids that it does with jets of Newtonian fluids.

16

In the work of Fukushima, Aanen and Westerweel (2000) an axisymmetric turbulent jet with a Reynolds number of 2000 was studied. This study was undertaken using particle image velocimitry (PIV) as well as laser induced fluorescence (LIF). This study was carried out by taking velocity measurements with the PIV and concentration measurements with the LIF system. The data sets were then compared to one another as well as to previous datasets by other researchers. The primary motivation for their work was to obtain greater insight into the coupling between turbulence and scalar mixing by taking simultaneously measurements of both turbulence and concentration. The results obtained by Fukushima et al. agreed well with data by previous researchers as well as DNS simulations.

The anisotropic spread rate that is found in wall jets was examined by Ewing, Benaissa and Pollard (1997). This spread rate manifests itself after $x/d = 10\sim15$ when the jet begins to spread 4-5 times faster in the wall-parallel direction than it does in the wall-normal direction. Some preliminary flow visualization images are shown in their work. It can be seen that the increase in lateral growth rate is caused by flow being expelled in the lateral direction very close to the wall. These ejections of fluid increase in width with increasing downstream distance and only occur on an intermittent basis. The anisotropic spread rate of wall jets was first noted by Rajaratnam & Pani at the University of Alberta.

Launder and Rodi (1981) completed a very thorough literature review on wall jets. Although this review is long out of date, it still provides a useful starting point for anyone interested in the field of turbulent wall jets. The purpose of their review was to determine what adaptations were required to the κ-ϵ turbulence model to make it work for turbulent wall jets. This lead to the development of algebraic stress models for turbulent flows.

Chapter 3: Equipment and Procedure

3.1 LDA system

The LDA measurements that were taken during the course of this experiment were taken using a two component TSI LDA system. This system consisted of a Coherent Innova 70 4W Argon ion laser. The laser beam was split into three components using a 9201 Colorburst beam separator. These three components (colors) are green at 514.5 nm, blue at 488 nm, and violet at 476.5 nm. Once the laser beam is split into three components, each color is split again creating two like beams. One beam from each color then has a frequency shift added to it by the Bragg cell inside the Colorburst. Although the output from the Colorburst consists of six beams only four are used. The green and blue beams are used since they contain more power than the violet beams and therefore yield a higher data rate. The Colorburst is connected to a TSI 9800 series fiber optic probe. This probe projects the laser beams into the glass tank which contains the jet being studied. The water inside the tank is seeded with titanium dioxide particles that scatter the light inside the measurement volume. The 9800 series probe operates in backscatter mode. This means the sensor which collects the data is located inside of the probe. Thus only light which is reflected backward towards to the probe is collected. The light is then transmitted to a TSI Colorlink 9230 receiver. This light signal is then converted to an electrical signal by photomultiplier tubes. This signal is then sent to the IFA 650 digital burst correlator for processing. The software package that was used to control and display the data taken by the LDA was FIND for Windows version 1.4 made by TSI. In order for the FIND software to accept a signal as a valid data point, the signal has to have at least

19

eight zero crossings. This corresponds to a seeding particle crossing at least eight fringes inside the measurements volume. The fringe spacing inside the measurement volume is governed by the following formula

$$d_f = \frac{\lambda}{2\sin(\kappa)} \qquad (3.1)$$

where λ is the wavelength of the laser light and κ is the half angle between the two beams. The measurement volume itself has an ellipsoidal shape. The diameter of the ellipsoidal volume is given by

$$d_m = \frac{4f\lambda}{\pi D_{e^{-2}}} \qquad (3.2)$$

where f is the focal length of the transmitting lens, D_e^{-2} is the diameter of the beam based on the e^{-2} intensity point entering the transmitting lens and λ is the same as above. The length of the ellipsoidal volume can then be calculated by

$$l_m = \frac{d_m}{\tan(\kappa)} \qquad (3.3)$$

The velocity of the seeding particle is then calculated by FIND using

$$u_{particle} = \frac{d_f}{t_l}\left(d_f F\right) \qquad (3.4)$$

20

where F is the Doppler shift frequency of the backscattered light. The mean flow velocity is calculated using $u_{particle}$ and the residence time, $\Delta t_{particle}$, in the following formula

$$U = \frac{\sum (u_{particle} \Delta t_{particle})}{\sum \Delta t_{particle}}$$ (3.5)

The residence time is the amount of time a seeding particle is inside of the measurement volume. The Reynolds stresses $\overline{u'^2}$, $\overline{v'^2}$ and $\overline{u'v'}$ and are calculated as follows

$$\overline{u'^2} = \frac{\sum_{j=1}^{n} (u_{j,particle} - U)^2 \Delta t_{j,particle}}{\sum \Delta t_{j,particle}}$$ (3.6a)

$$\overline{v'^2} = \frac{\sum_{j=1}^{n} (v_{j,particle} - V)^2 \Delta t_{j,particle}}{\sum \Delta t_{j,particle}}$$ (3.6b)

$$\overline{u'v'} = \frac{\sum_{j=1}^{n} (u_{j,particle} - U)(v_{j,particle} - V) \Delta t_{j,particle}}{\sum \Delta t_{j,particle}}$$ (3.6c)

where $u_{j,particle}$ and $v_{j,particle}$ are the velocities of the jth particle and n is the number of validated particles that passed through the measurement volume. Each zero crossing inside the measurement volume must attain a magnitude of at least 100mV before the

21

software validates the signal as a data point. A summary of the optical parameters for the LDV system used in this thesis is presented below in Table 3.1

Table 3.1: Summary of LDV optical parameters

Optical Parameter	Green Laser beam	Blue Laser Beam
wavelength λ	514 nm	488 nm
fringe spacing d_f	4.21×10^{-3} mm	4.04×10^{-3} mm
measurement volume diameter d_m	0.060 mm	0.064 mm
Length of measurement volume l_m	1.01 mm	1.10 mm

3.2 Jet and Enclosure

The jet that was examined in this thesis was created by a bi-cubic nozzle. The procedures involved in designing this nozzle were adapted from a paper by Morel (1975). The inlet to the nozzle is 50mm in diameter while the outlet is 5mm in diameter. This yields an area contraction ratio of 100:1 and a corresponding velocity increase inside the nozzle of 100:1. The bi-cubic nozzle type was chosen because it offers a proven record in producing flat velocity profiles with a minimum amount of non-uniformity at the jet exit. The nozzle was made of aluminum and was then anodized. The nozzle was machined on a CNC lathe to an accuracy of +/- 0.005mm.

The system is of a closed loop design and is powered by a magnetic drive centrifugal pump. The pump is integrated into the system in such a manner as to be self priming. The glass tank which contains the nozzle assembly measures 0.35m x 0.45m x 1.19m

22

and has a capacity of 187 litres. A schematic of the inside of the tank is shown in Figure 3.1. This diagram shows a moveable wall which was placed inside the tank. This wall was oriented so that it is parallel to the longitudinal axis of the jet as well as being parallel to the sidewalls of the tank (the wall normal direction was the z axis). This wall was moved in the z direction and measurements were taken with the wall at the following distances from the jet axis: $h = 2.5d$, $5d$, $10d$ as well as with the wall removed from inside the tank.
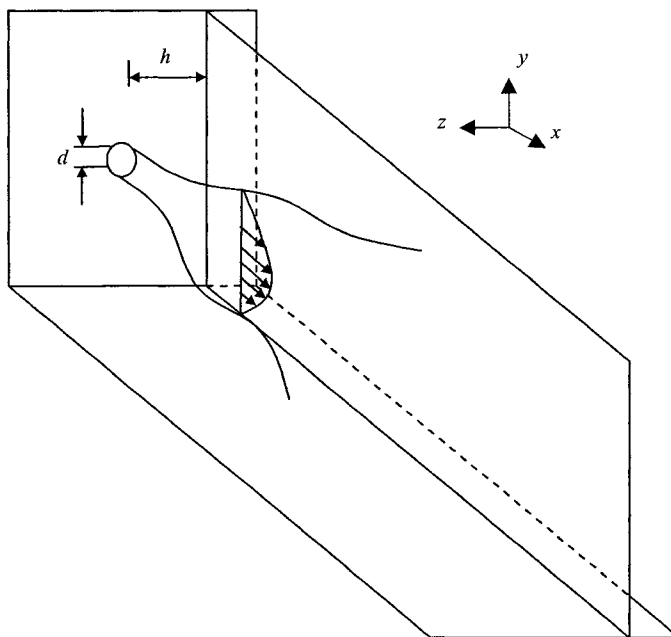
Figure 3.1 Schematic of apparatus.

The wall that was used was made of 4mm thick window glass. Originally a piece of plexiglas was used for this application but it was found to adversely effect data rate when taking measurements close to the wall. The cause of this adverse effect was found to be that the Plexiglas reflected the laser beams. This reflection was a problem because the probe operates in backscatter mode. The reflected light was causing a

23

decrease in contrast between the actual signal and the background. The decrease in contrast caused the decrease in data rate. When the Plexiglas was used, measurements could only be taken to within 1.25cm of the wall. Window glass was then chosen as an alternative to the Plexiglas. It exhibited much less reflection and as a result didn't cause as much of a decrease in contrast. This resulted in a data rate that was on the order of ten times higher than when Plexiglas was used when measurements were taken close to the wall. The use of window glass allowed for measurements to be taken to within 1.5mm of the wall. This is 11mm closer than when the Plexiglas was used. Other media were tested for use as a wall including a first surface mirror and a black painted surface. However the window glass gave the best results.
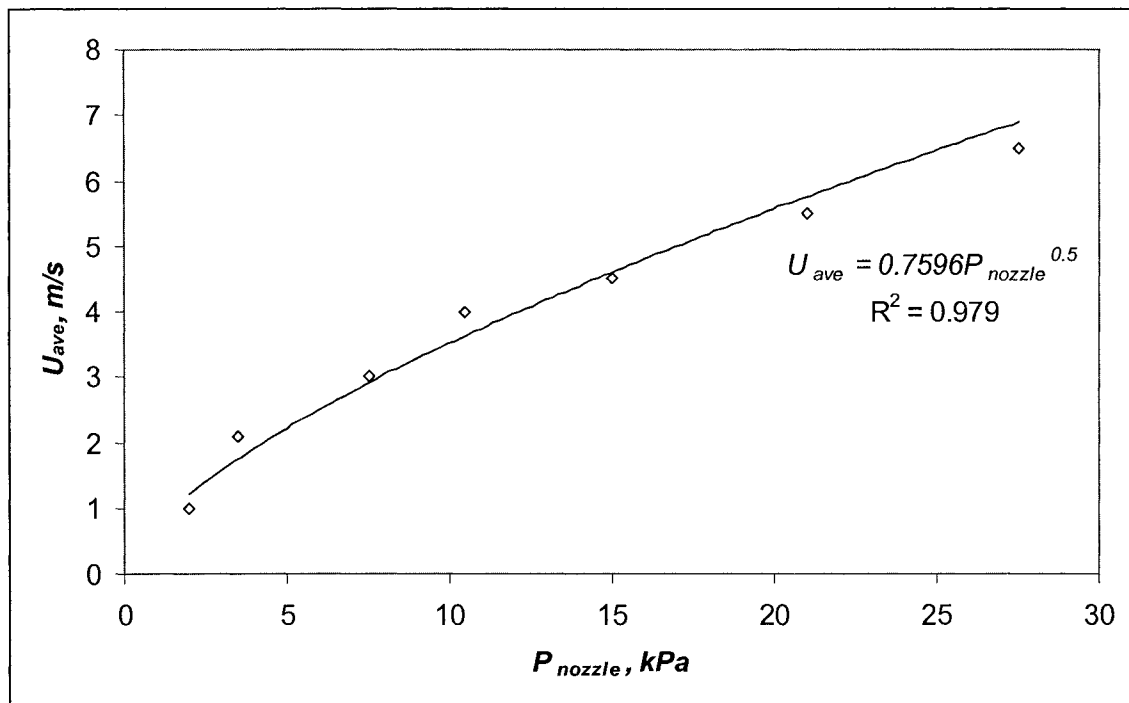

The equation on the plot reads:

$$U_{ave} = 0.7596 P_{nozzle}^{0.5}$$
$$R^2 = 0.979$$

with axes $U_{ave}, m/s$ (vertical) and P_{nozzle}, kPa (horizontal)

Figure 3.2: A plot of nozzle pressure vs. exit velocity for the jet nozzle

24

3.3 Experimental Procedure

The nozzle flow rate was not measured directly, rather the nozzle was instrumented with a pressure tap. This pressure tap was connected to a Validyne differential pressure transducer with a range of 0-34.5 kPa and a sensitivity of 3.45kPa/volt. The nozzle was calibrated and a curve of pressure vs. exit velocity was created and is shown in Figure 3.2. The nozzle was calibrated by pumping water through the nozzle at a constant flow rate. This water was collected in a large basin (~20L) and then weighed. The flow rate was calculated by dividing the volume of water collected by the time required to fill the basin. This flow rate was used to determine the approximate Reynolds number at the jet exit.

The LDA took measurements of velocity in the x-y plane. The measurements were taken at the following distances downstream: x/d = 2.5, 5, 7.5, 10, 15 and 20. These measurements were taken along traverses in the z direction while maintaining constant x and y coordinates during each traverse. The y coordinate was chosen to correspond with the center of the jet at the jet exit. The experiment was run with the jet having an exit Reynolds number of 20000 (±2%). Each data point was acquired over a set period of time ranging from one to five minutes. The shorter time period of one minute was used when readings were being taken toward the center of the jet where the data rate was higher. The reason why the data rate was higher towards the center of the jet is because the velocity is higher there. Since the concentration of the seeding particles is uniform everywhere inside the tank, higher velocities yield higher data rates simply because more particles move through the measurement volume if

25

the velocity increases. This can cause a problem known as velocity bias if measurements are taken in a flow with high velocity gradients or large fluctuations in velocity. This is because more of the faster moving particles move through the measurement volume than the slower particles, thus the fast particles are given an unequal weighting. The FIND software package used for data analysis made corrections for velocity bias by using burst transit time weighting. This means the amount of time a particle was present inside the measurement volume, $\Delta t_{particle}$, was used as a weighting factor when calculating the flow velocity.

The traverse was started on the 'free' side of the jet and was continued through the jet in the negative z direction in varying increments through to the wall. The smallest increment that was made was 0.25mm and the largest increment was 1.0mm. As a general rule smaller increments were made in areas where there was a large gradient in the data that was observed. The traverse was continued until the measurement volume came within 1.5mm of the wall or until the shear layer was exited.

The traverse that was used consisted of two Superior Electric SLO-SYN stepper motors, model no M091-FC06. This motor has a resolution of 200 steps/rev. Each motor was connected to a lead screw, one lead screw controlled motion in the z direction and the other controlled motion in the y direction. These lead screws had a pitch of 1 thread/5mm. Coupled with the stepper motors the spatial resolution of the traverse in the y and z direction is 0.0254mm or 0.0127mm if a half stepping technique is employed. Motion in the x direction was constrained by rails which are

26

attached to the concrete floor in the lab. The traverse assembly sat on these rails and motion in the x direction was controlled manually. The accuracy and repeatability of the traverse was tested using a dial gage. It was found that the traverse was repeatable to within 0.025mm and was accurate to 0.020mm.

The computer program used to control the stepper motors makes corrections for motion in the z direction. This is necessary because on the different media the laser beams travel through before the control volume. The beams must pass through the glass sidewall of the tank as well as the water inside of the tank. The air-glass interface causes the beams to bend, as does the glass-water interface. The computer program makes simple corrections using Snell's law to ensure that the control volume is moved the desired amount, not the traversing mechanism.

3.4 Measurement Accuracy & Noise

In most cases, the frequency of a measured LDA signal burst is not equal to the Doppler frequency because the measured frequency also contains noise. The electrical signal received by the signal processor must be filtered before it can be processed. A band pass filter is applied to the signal. The choice of filter is left to the user and the selection is made via the user interface of the FIND software program. The lower end of the band pass filter is used to remove the DC pedestal from the LDA signal. Once this pedestal is removed the signal essentially has a mean value of 0V. The high end of the filter is then applied. Care must be taken to ensure that the signal itself is not cut off by the application of the filters. In order to choose a

27

reasonable value for the band pass filter something must be known about the flow being studied. The two most important parameters that must be estimated are the mean flow velocity and the turbulence intensity. The estimate of the mean flow velocity and the dimension of the ellipsoidal measurement volume are used to set the value of the low pass filter, while the mean velocity and the turbulence intensity estimates are used to select a value of the high pass filter.

The signal to noise ratio (SNR) of a LDA signal is given by the following formula

$$SNR = \frac{\eta P_o}{\Delta f} \left(\frac{D_a}{f_r} \frac{d_e}{f_t} \right)^2 d_p^2 G K^2 \tag{3.7}$$

where η is the quantum efficiency of the LDA photo detector and is generally a constant, P_o is the incident laser power and Δf is the bandwidth of the filters used in the system. The terms in brackets represent the optical parameters, or f-number, of the LDA system. The term D_a is the diameter of the receiving lens and f_r is the focal length of the receiving lens. This ratio is a relative measure of how much of the scattered light is received. Likewise d_e is the diameter of the laser beam and f_t is the focal length of the transmitting lens. This ratio is a measure of the relative light intensity inside the measurement volume. The term d_p is the diameter of a seeding particle, G is a scattering coefficient and K is a visibility factor. These last three terms must be evaluated using Mie scattering theory.

28

It can be seen from Equation 3.7 that laser power has an effect on the SNR of the LDA signal. Thus every effort should be made to use the laser at its highest power settings. Another way of increasing laser light intensity is to minimize losses in the fiber optic transmission system. This can be accomplished by optimizing the coupling alignments at the Colorburst interface. This optimization was carried out on a daily basis using a laser power meter whenever measurements were being taken. If this check is not completed whenever measurements are being taken, damage can occur to the fiber ends due to misalignment and the high laser power being used.

The optical parameter terms in Equation 3.7 have the potential to have a significant effect on SNR. This is due their exponent power of 2. From these terms it can be seen it is advantageous to have a small measurement volume thus keeping the laser intensity inside the volume high. However this does have some practical limitations because the measurement volume for the green beams should coincide with the measurement volume for the blue beams. As the volumes get smaller it becomes more difficult to achieve coincident measurement volumes. The degree of overlap, or coincidence, of the two measurement volumes was checked by placing a microscope objective lens at the location of the volume and projecting the image onto a wall. If necessary, adjustments could be made to the probe to change the location of the measurement volumes. This was a parameter that was checked before measurements were taken. The probe alignment was pre set at the factory; however vibrations in the building and general use can cause the measurement volumes to move away from each other over time.

Chapter 4: Results

Velocity measurements were taken at various locations inside the tank with different wall configurations. The results are presented in this chapter.

4.1 Free jet

As mentioned before this free jet is not a true free jet because of the surrounding enclosure which caused flow reversal and recirculation inside the tank. Figure 4.1 shows the mean velocity across the jet at varying distances downstream. The centerline velocity at x/d = 2.5 is 4.14m/s. Measurements could not be taken directly at the exit because of the physical limitations of the experimental apparatus. However x/d = 2.5 is within the potential core of the jet so it can be assumed that the exit velocity is also 4.14m/s. This result agrees with the 4.15m/s velocity calculated by measuring the pressure differential across the nozzle as discussed in Section 2.1. Figure 4.2 is a normalized version of Figure 4.1. The mean velocity was normalized using the centerline velocity, and the radial coordinate was normalized using the downstream distance from the virtual origin.

It can be seen from Figure 4.2 that this method of normalizing works well between $7.5 < x/d < 20$ as all data points lie within +/- 4% of the normalized mean in this range. This particular method of normalizing was chosen to be consistent throughout the thesis. The more popular method involves normalizing the radial coordinate using the jet half-width. This would not have been practical when the enclosure geometry was changed to bring a wall closer to the jet because of the possible changes in the

30

shape of the velocity profile and subsequent ambiguity in determining half-width. The measurements shown in Figure 4.1 and 4.2 were taken traversing the y direction. Figure 4.3 was made by taking a traverse in the z direction. The results are similar in shape and magnitude to the results shown in Figure 4.2 as is expected from an axisymmetric jet. The difference between taking measurements during a z direction traverse versus a y direction traverse becomes apparent when the components of Reynolds stresses are examined.

4.2 Free Jet Turbulence Statistics, y-traverse

The turbulence statistics presented in this section were taken along a traverse in the y-direction. Figure 4.4 is a normalized plot of Reynolds shear stresses. As was standard throughout the experiment, measurements were taken from $x/d=2.5$ to $x/d = 20$. For $x/d = 2.5$ the maximum normalized Reynolds stress of 0.008 occurred at a value of $y/(x-x_o) = 0.19$. The maximum normalized Reynolds stress increased to 0.0085 at a downstream distance of $x/d = 5$ and the location of the maximum changed to $y/(x-x_o) = 0.10$. It can be seen that the value of Reynolds shear stress increases as the distance from the exit increases. At the farthest downstream location tested, $x/d = 20$, the maximum Reynolds stress is 0.015 and occurs at $y/(x-x_o) = 0.07$. This result is similar to the results obtained in HCG94, with their maximum Reynolds shear stress being 0.0205 at $y/(x-x_o) = 0.08$. It should be noted that the detailed results presented in HCG94 were taken at 70 diameters from the jet exit.

31

Two components of the Reynolds normal stress, $\overline{v'^2}$ and $\overline{u'^2}$, were also measured. A normalized $\overline{u'^2}$ plot is shown in Figure 4.5. The normalized turbulence velocity $\overline{u'^2}$ increases with downstream distance as is expected. At $x/d = 2.5$, $\overline{u'^2}/U^2_c = 0.0016$ at the centerline. This corresponds to a turbulence intensity of 4% in the x-direction. This low level of turbulence can be attributed to the bicubic nozzle which was the source of the jet. The $\overline{u'^2}$ velocity decreases towards the centerline for both $x/d = 2.5$ and 5. From $x/d = 7.5$ to 15 there is no appreciable reduction in $\overline{u'^2}$ turbulence velocity as the centerline is approached. At $x/d = 20$ this changed as the turbulence velocity again decreased towards the centerline. In these normalized plots the jet appears wider at the exit because the radial coordinate is normalized with downstream distance. This causes the plots to appear to shrink in width with increasing downstream distance.

The plot shown in Figure 4.6 is a normalized plot of $\overline{v'^2}$. Figure 4.6 shows that at the same downstream distance $\overline{v'^2}$ is consistently less than $\overline{u'^2}$. This result is expected because there should be very little $\overline{v'^2}$ present at the exit of the jet. The turbulence in the y-direction, $\overline{v'^2}$, is generated by turbulence in the x-direction, $\overline{u'^2}$. In other words, since $\overline{v'^2}$ feeds off of $\overline{u'^2}$ it is unlikely that $\overline{v'^2}$ would become larger than $\overline{u'^2}$. The maximum value shown in Figure 4.6 occurs at the farthest downstream position that measurements were taken at, $x/d = 20$. The maximum value of $\overline{v'^2}/U^2_c = 0.0326$

32

occurs at the centerline. This is different than Figure 4.5 where the turbulence decreased towards the centerline at $x/d = 20$.

4.3 Free jet turbulence, z-traverse

Turbulence statistics presented in this section were taken along a traverse in the z-direction. The same statistics that were measured during the y-traverse were measured and they are presented below. A normalized plot of Reynolds stress for $x/d = 2.5$, 5, and 7.5 is shown in Figure 4.7. This plot is different than the one shown in Figure 4.4 in that it exhibits two maxima and two minima with one of each on either side of the centerline. The results in Figure 4.7 also differ from Figure 4.4 because the Reynolds stress decreases with downstream distance. The maximum normalized Reynolds stress of 0.0047 occurs at a downstream distance of $x/d = 2.5$. The maximum of 0.08 found in the y-traverse is 16 times larger than the maximum in the z-traverse. The shape of the shear stress plot keeps its two-maxima, two-minima shape until $x/d=10$. At this point the trend is hard to visualize because of scatter in the data. This can be attributed to the small readings that were being taken and uncertainty in the measurements. Most of the uncertainty in this experiment was experienced when measurements were taken close to a wall or along the edge of a jet. That uncertainty was caused by a low data rate and small sample size which was a direct consequence of the low velocity found in these two regions. The scatter in the data found in Figure 4.8, a normalized plot of Reynolds stress of $x/d = 10$, 15, and 20, was not caused by low data rate. This is known because the scatter exists in regions in the center of the jet where the data rate is at its highest. It is likely that this scatter is

33

being caused because the magnitude of the measurements is so small that they are approaching the resolution of the LDA system.

Figure 4.9 is a normalized plot of $\overline{u'^2}$ made during a traverse in the z-direction. For $x/d = 2.5$ to 15 the plot is similar to Figure 4.5, the normalized plot of $\overline{u'^2}$ made in the z-direction. A notable difference occurs at $x/d = 20$. The maximum normalized value of 0.055 occurs at the centerline along the y–traverse at $x/d = 20$. The maximum normalized $\overline{u'^2}$ along the z-traverse is close to 0.08 and at the centerline it is 0.07. This downstream variation is interesting because the exit velocities are within 0.96% of one another. This suggests that the variation in $\overline{u'^2}$ is not caused by a variation in the exit velocity of the jet but is caused by the enclosure affecting the jet development.

A normalized plot of $\overline{v'^2}$ is shown on Figure 4.10. This plot is similar to Figure 4.6, a plot of $\overline{v'^2}$ made for a y-traverse. In Figure 4.10 the maximum normalized $\overline{v'^2}$ value of 0.034 occurs at the centerline of the $x/d = 20$ traverse. Along the y-traverse the maximum $\overline{v'^2}$ value is 0.033. This is a difference of 3% and is considerably smaller than the 50% difference encountered when comparing the $\overline{u'^2}$ plots.

4.4 Wall located at h/d=10, z-traverse

The measurements taken in this section were done with the wall 10 diameters (50mm) from the axis of the jet. Figure 4.11 is a normalized plot of the velocity profile

34

downstream from the jet exit. Self similarity in mean velocity is observed from $x/d = 7.5$ to 20. This is consistent with the results obtained from the free jet.

The graph shown in Figure 4.12 is a normalized plot of Reynolds shear stress. The maximum normalized Reynolds stress of -0.015 in this Figure occurs at the jet centerline at $x/d = 20$. There is considerable scatter in the data at $x/d = 20$ but as discussed earlier it is unlikely that this scatter was caused by a low data rate. The trend toward large negative downstream Reynolds stresses is more prevalent in Figure 4.12 than it is in Figure 4.8 when the free jet was examined. This trend could be caused by the increased velocity gradient between the jet and the free fluid. The presence of the wall made the effective size of the enclosure much smaller resulting in an increase in the velocity of the flow reversal in the free fluid and a greater velocity gradient between the jet and the free fluid.

Normalized plots of $\overline{u'^2}$ and $\overline{v'^2}$ are shown in Figures 4.13 and 4.14 respectively. Figure 4.13 shows that self similarity in $\overline{u'^2}$ is never achieved for the downstream distances tested in this experiment. It should also be noted that the normalized values of $\overline{u'^2}$ shown in Figure 4.13 are consistently similar than to shown in Figure 4.9, a normalized plot of $\overline{u'^2}$ for the free jet. This trend disappears at $x/d = 20$ where a maximum of 0.08 is attained. This is larger than the maximum of 0.055 obtained in Figure 4.9 This indicates that the presence of the wall could enhance the development of $\overline{u'^2}$ far downstream from the jet exit. The data in Figure 4.13 are smooth and do not show scatter until $x/d = 20$. The scatter that is present at $x/d = 20$ is less than 5%

35

of the maximum centerline value. Another interesting phenomenon is that $\overline{u'^2}$ has a relatively flat profile at $x/d = 15$ and 20.

Figure 4.14 also exhibits no self similarity. The values obtained closely agree with the data shown in Figure 4.10. There is a discrepancy at $x/d = 15$ and 20 where the values are larger than they are for the free jet. At $x/d = 15$ the maximum normalized $\overline{v'^2}$ value is 0.0347 and at $x/d = 20$ the maximum is 0.043. These values are 15% and 22% larger than their respective free jet values. The same flatness that is seen in Figure 4.13 is also demonstrated in Figure 4.14.

4.5 Wall located at h/d=5, z-traverse

The measurements taken in this section were taken with the wall 5 diameters (25mm) from the axis of the jet. A normalized mean velocity profile is shown in Figure 4.15. With the exception of $x/d = 2.5$, the profiles collapse on each other resulting in self similar profiles. This result is consistent with those of the free jet as well as with the wall $10d$ from the jet axis.

Figure 4.16 is a normalized plot of Reynolds shear stress for $x/d = 2.5$, 5 and 7.5 and Figure 4.17 is a similar plot for $x/d = 10$, 15 and 20. The shape of the plots in Figure 4.16 is similar to that found in Figures 4.7 and 4.12 (a maxima and a minima on each side of the jet centerline). These maxima and minima dissapear with increasing downstream distance. In Figure 4.17 at $x/d = 20$ there is considerable scatter in the data but there is a definite trend toward the Reynolds stresses being

36

positive. This result is a contrast to what occurred with the wall positioned $10d$ from the jet axis in Section 4.4. In Section 4.4 it can clearly be seen that the Reynolds stress attains a large negative value at $x/d = 20$.

The normalized plots of $\overline{u'^2}$ and $\overline{v'^2}$ are shown in Figures 4.18 and 4.19. No self similarity is demonstrated in either of these Figures. The $\overline{u'^2}$ data shown in Figure 4.18 are similar to the data presented in Figure 4.13 for $x/d = 2.5$, 5 and 7.5. This is not the case for $x/d = 10$ through 20. At $x/d = 10$ the maximum normalized $\overline{u'^2}$ value is 0.05. In Figure 4.13, for the case in Section 4.4 where the wall is $10d$ from the jet axis, the maximum normalized $\overline{u'^2}$ value is 0.045. This is a difference of 11%. This discrepancy gets larger downstream. At $x/d = 15$ the maximum in Figure 4.18 is 18% smaller than the comparable data in Figure 4.1. At $x/d = 20$ the difference between the two maximum values is even higher, with the data presented in Figure 4.18 being 33% smaller than the comparable maximum shown in Figure 4.13.

The data presented in Figure 4.19, a normalized plot of $\overline{v'^2}$, agree well with the data presented in Figure 4.14 with the exception of the $x/d = 20$ traverse. The data shown in Figure 4.19 do not show the large jump at the centerline like the data in Figure 4.14.

4.6 Wall located at h/d=2.5, z-traverse

The measurements in this section were taken with the wall 2.5 diameters (12.5mm) from the axis of the jet. A normalized mean velocity plot is shown in Figure 4.20. Although self similarity in the mean velocity is approached close to the exit, it is not

37

actually achieved until $x/d = 10$. This is different than in section 4.5 where all of the mean velocity profiles were self similar except at $x/d = 2.5$. This is however consistent with the data in section 4.1 where more than $5d$ downstream distance was required for the mean velocities to become self similar.

Figure 4.21 is a normalized plot of Reynolds shear stress for $x/d = 2.5$, 5 and 7.5. This Figure is unremarkable in that it exhibits the same general shape as Figure 4.7 in Section 4.3, Figure 4.12 in Section 4.4, and Figure 4.16 in Section 4.5. There is a small spike in the data for $x/d = 7.5$ on the negative side of the origin. It should be noted that the negative side of the origin is the side of the jet the wall is on. This spike in shear stress is caused by the presence of the wall. In the previous sections in this chapter no such spike was observed.

Figure 4.22 is a plot of normalized Reynolds shear stresses for $x/d = 10$, 15 and 20. In this plot all of the Reynolds stresses exhibit a definite trend towards becoming negative towards the centerline. This is keeping with the trend in Sections 4.3 and 4.4 where the shear stress also became all negative at distances downstream from the exit. The trend observed in Figure 4.22 is inconsistent with the data presented in Figure 4.17 where no obvious trend is present in the downstream Reynolds stresses until $x/d = 20$, when most of the data are all positive with significant amounts of scatter. It should also be noted that in Figure 4.22 there is a small spike in the data taken at $x/d = 10$. Larger spikes are found in the data for $x/d = 15$ and 20. The

38

increases in shear stress are caused by the presence of the wall. The shear stress created by the wall increased with increasing downstream distance.

A normalized plot of $\overline{u'^2}$ is shown in Figure 4.23. The plots in this figure are similar to the $\overline{u'^2}$ plot shown for the case where the wall was $10d$ from the jet axis, Figure 4.13. This plot also exhibits a large spike in $\overline{u'^2}$ where the jet gets close to the wall. At $x/d = 20$ the creation of this wall generated turbulence increases the local $\overline{u'^2}/U_c^2$ from 0.031 just outside the wall boundary layer to a maximum of 0.13 on the inside. This is an increase of 319%.

Figure 4.24 is a normalized plot of $\overline{v'^2}$. The data in this figure also closely agree with the $\overline{v'^2}$ data presented in Section 4.4 where the wall was $10d$ from the jet axis. The increase in the normalized $\overline{v'^2}$ value at $x/d = 20$, from outside the wall boundary layer to the inside, is 404% or an increase from 0.024 to 0.121. These results show what a significant role the wall has on turbulence generation.

4.7 Results for fixed x/d. Wall position varied.

Results previously shown were plotted at various downstream positions with the wall position held constant. Plots of mean velocity and turbulence statistics were also plotted at fixed downstream stations with the wall position varied. These plots can be seen in Figures 4.25 through 4.44.

39
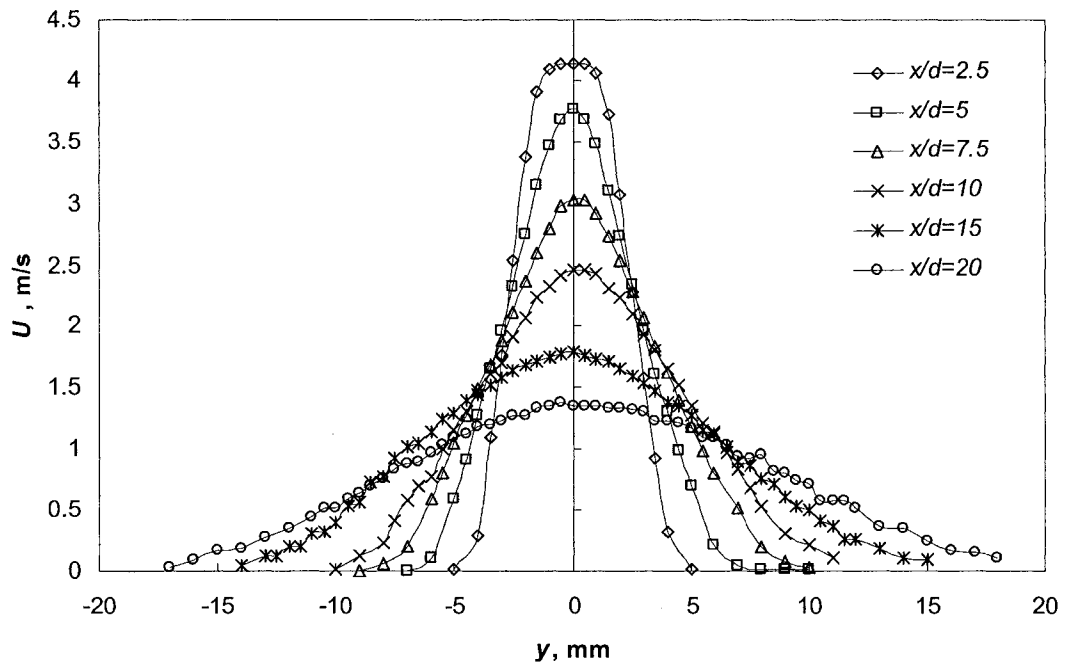
Figure 4.1: A plot of velocity across the jet for various downstream locations. Points connected for visual continuity.

40
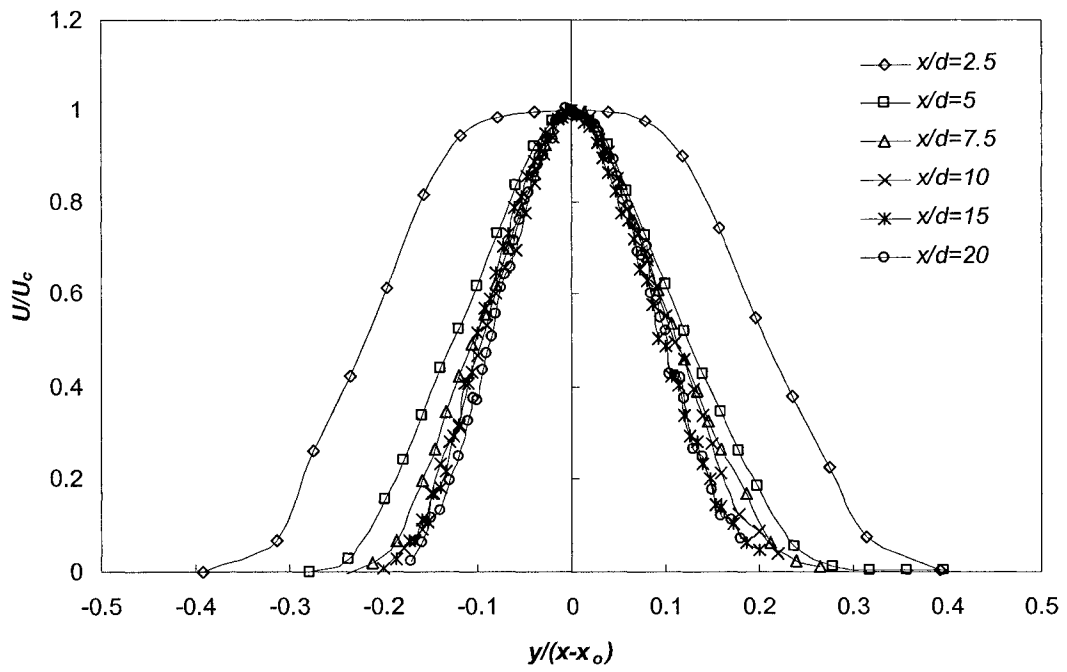
Figure 4.2: A normalized velocity plot showing profiles at various downstream locations. The dataset used to create this plot was taken along a traverse in the *y*-direction with no interior wall present. Points connected for visual continuity.
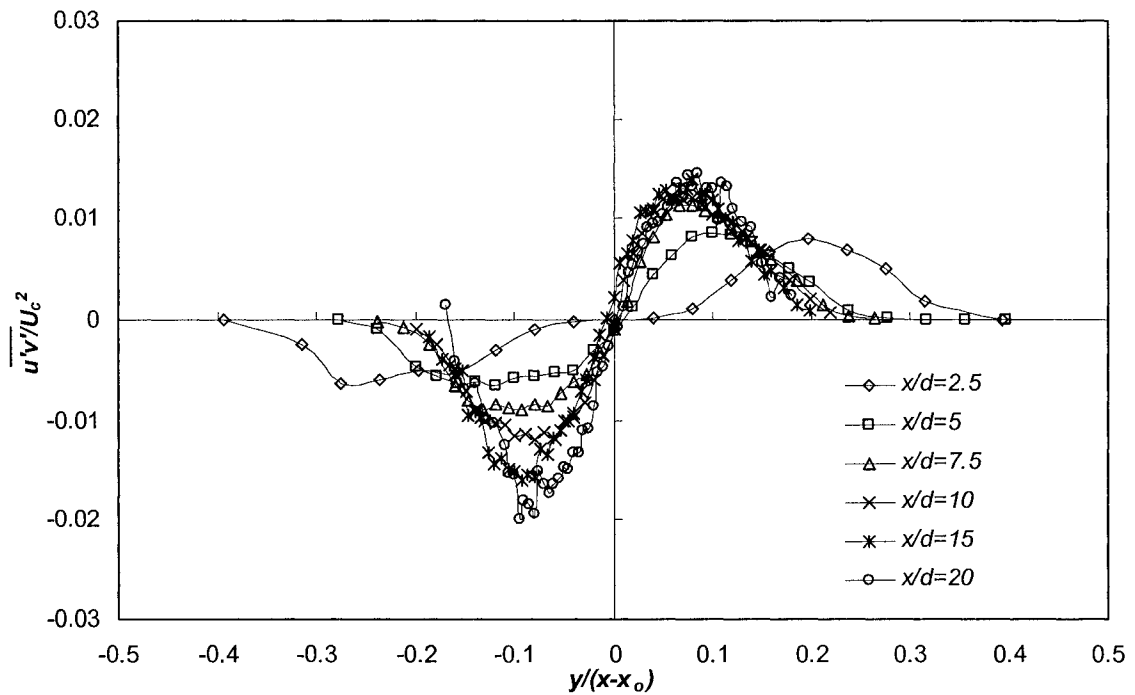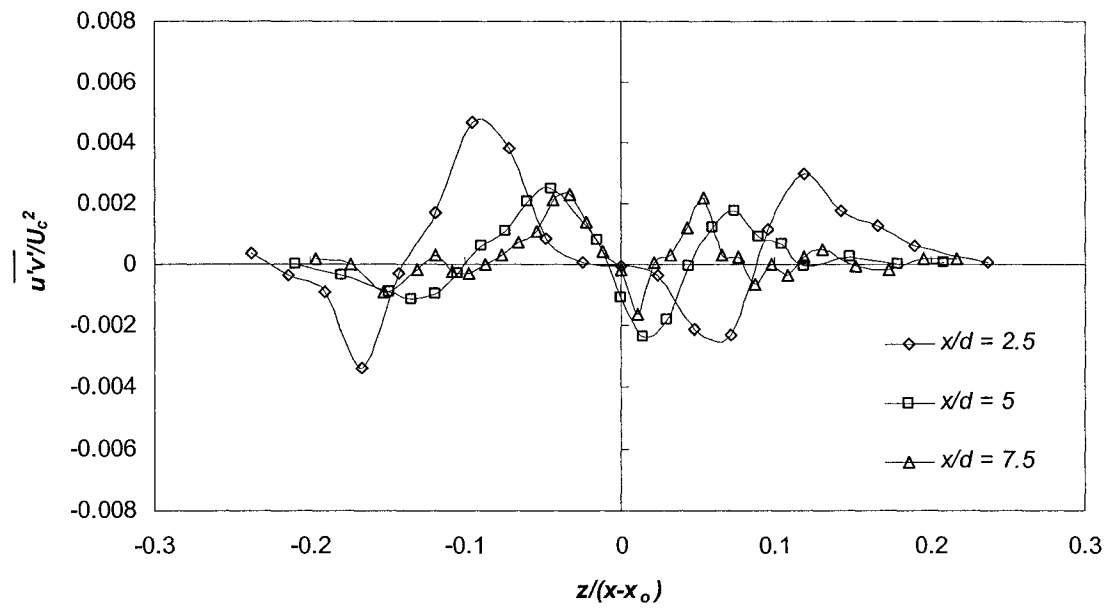
41
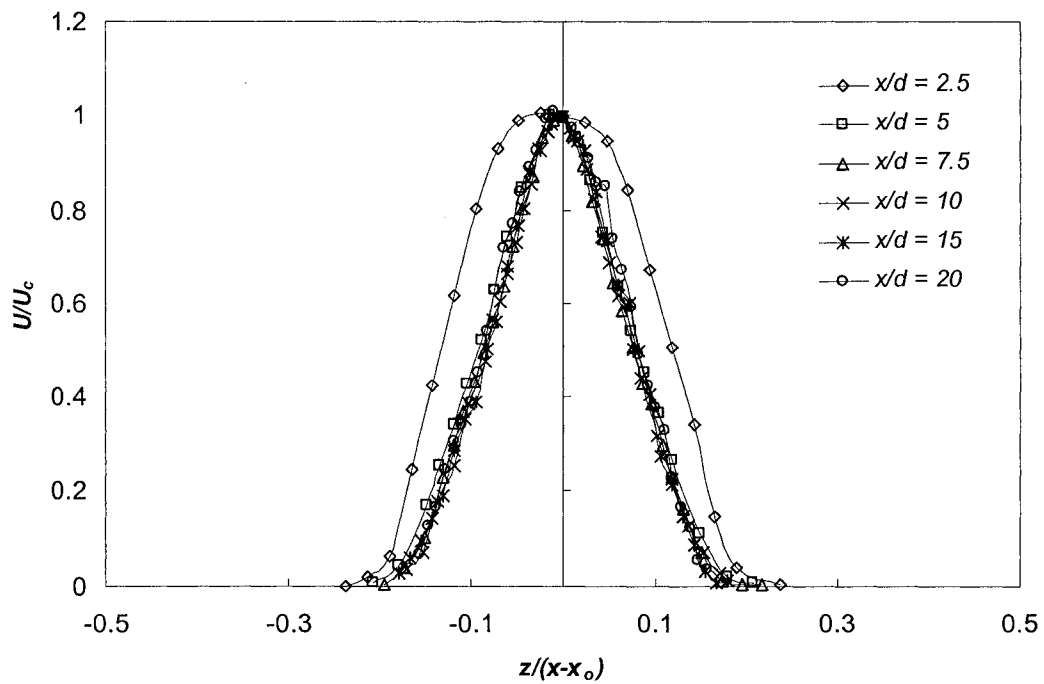
Figure 4.3: A normalized plot of downstream velocity profile taken at various downstream positions. The dataset used in this plot was taken along a traverse in the z-direction with no interior wall present. Points connected for visual continuity.
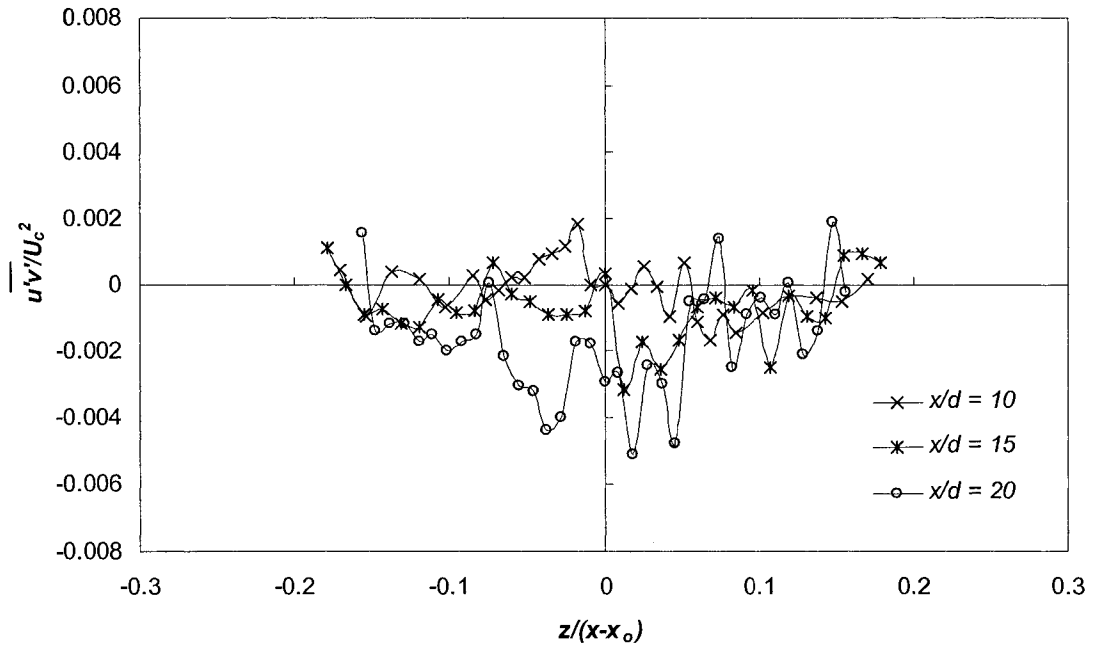
Figure 4.4: A normalized plot of Reynolds shear stress at various downstream locations. This dataset was taken along a traverse in the y-direction with no interior wall present. Points connected for visual continuity.
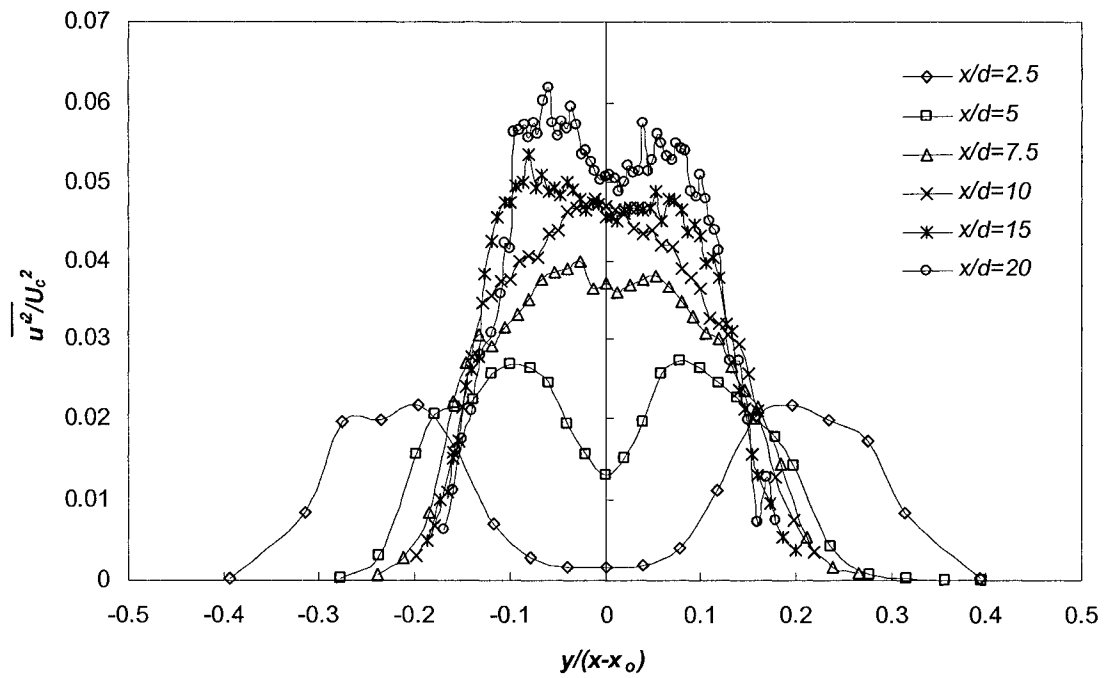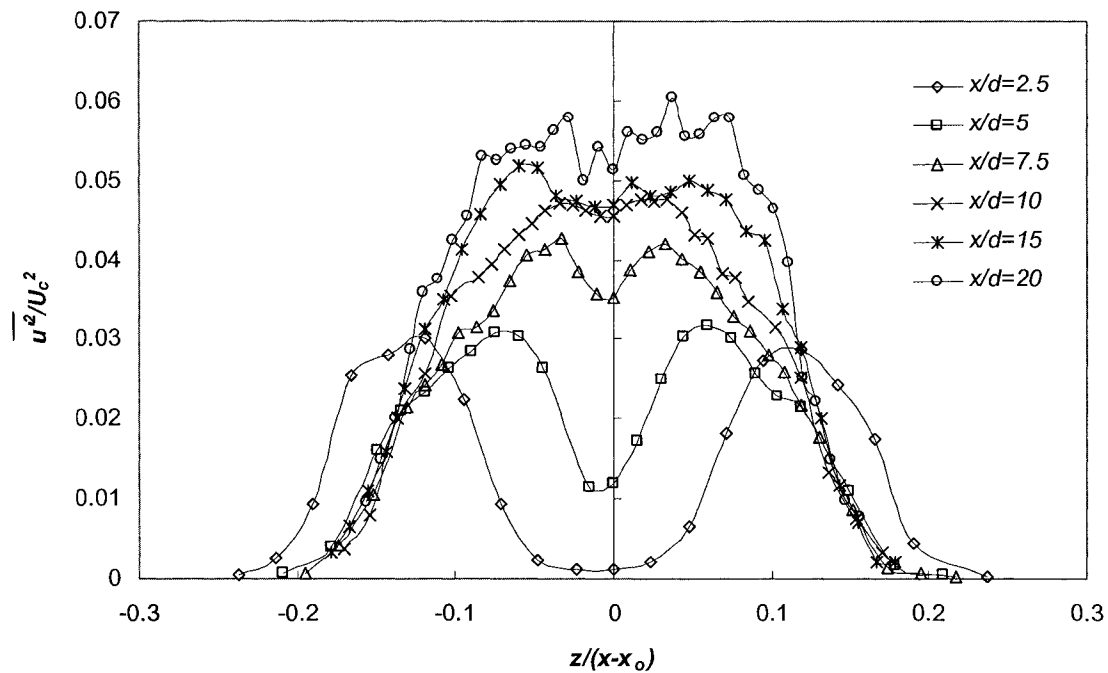
Figure 4.5: Normalized plot of $\overline{u'^2}$. The dataset used in this Figure was taken along a traverse in the y-direction with no interior wall present. Points connected for visual continuity.
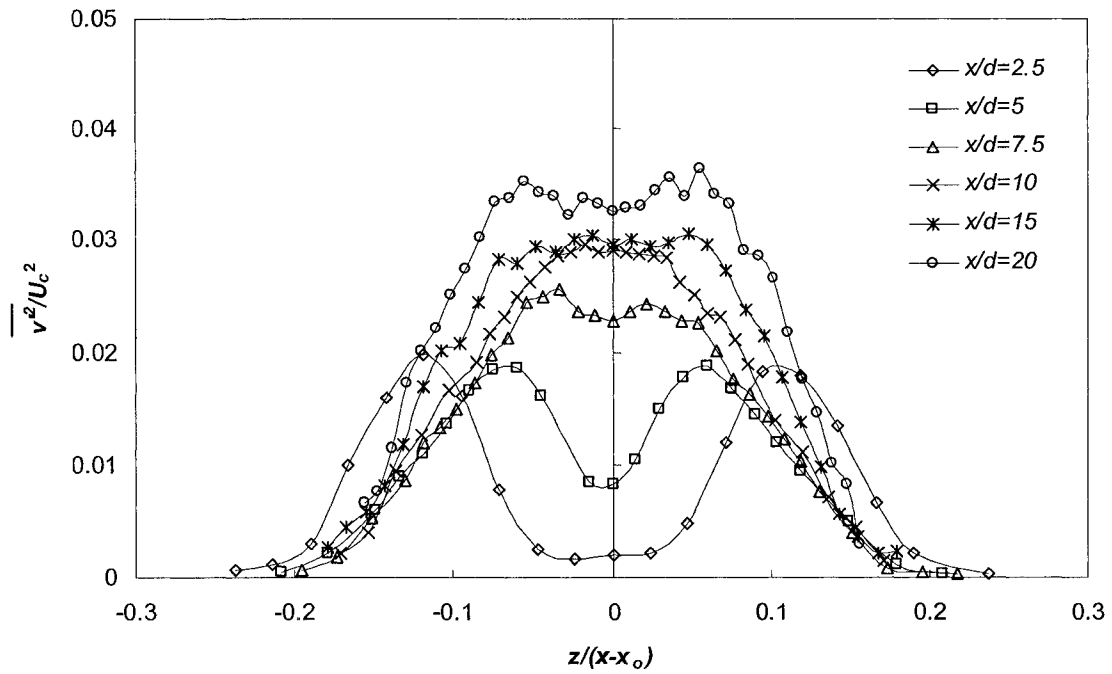
44
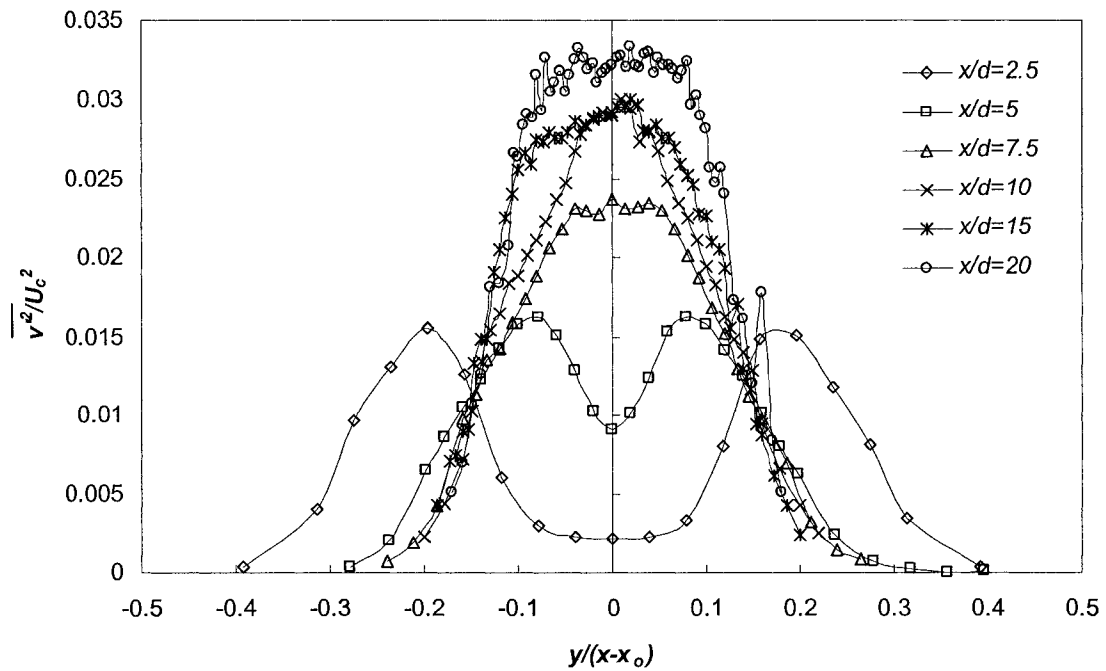
Figure 4.6: A normalized plot of $\overline{v'^2}$. The dataset used in this Figure was taken along a traverse in the y-direction with no interior wall present. Points connected for visual continuity.

45

0.008
0.006
0.004
0.002
0
-0.002
-0.004
-0.006
-0.008

$\overline{u'v'}/U_c^2$

-0.3   -0.2   -0.1   0   0.1   0.2   0.3

$z/(x-x_o)$

x/d = 2.5
x/d = 5
x/d = 7.5

Figure 4.7: A normalized plot of Reynolds shear stress for x/d **= 2.5, 5 and 7.5. The dataset used in this Figure was taken along a traverse in the** z**-direction with no interior wall present. Points connected for visual continuity.**

46

Figure 4.8: A normalized plot of Reynolds shear stress for x/d = 10, 15 and 20. The dataset used in this Figure was taken along a traverse in the z-direction with no interior wall present. Points connected for visual continuity.
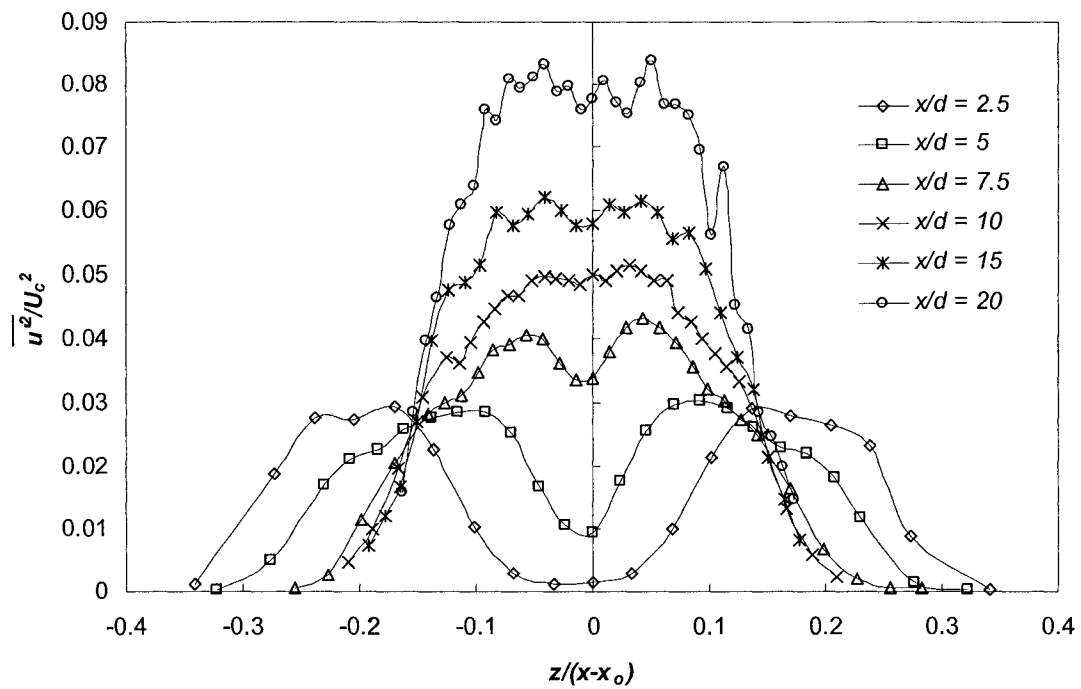
47

Figure 4.9: Normalized plot of $\overline{u'^2}$. The dataset used in this Figure was taken along a traverse in the z-direction with no interior wall present. Points connected for visual continuity.
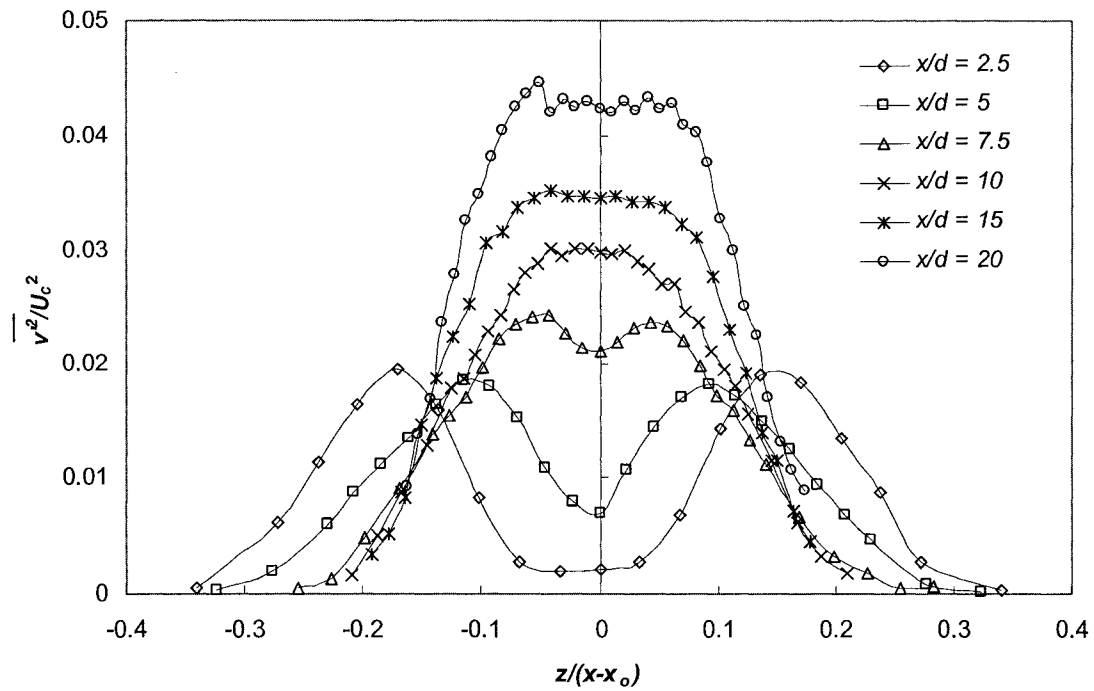
48

Figure 4.10: Normalized plot of $\overline{v'^2}$. The dataset used in this Figure was taken along a traverse in the z-direction with no interior wall present. Points connected for visual continuity.

49
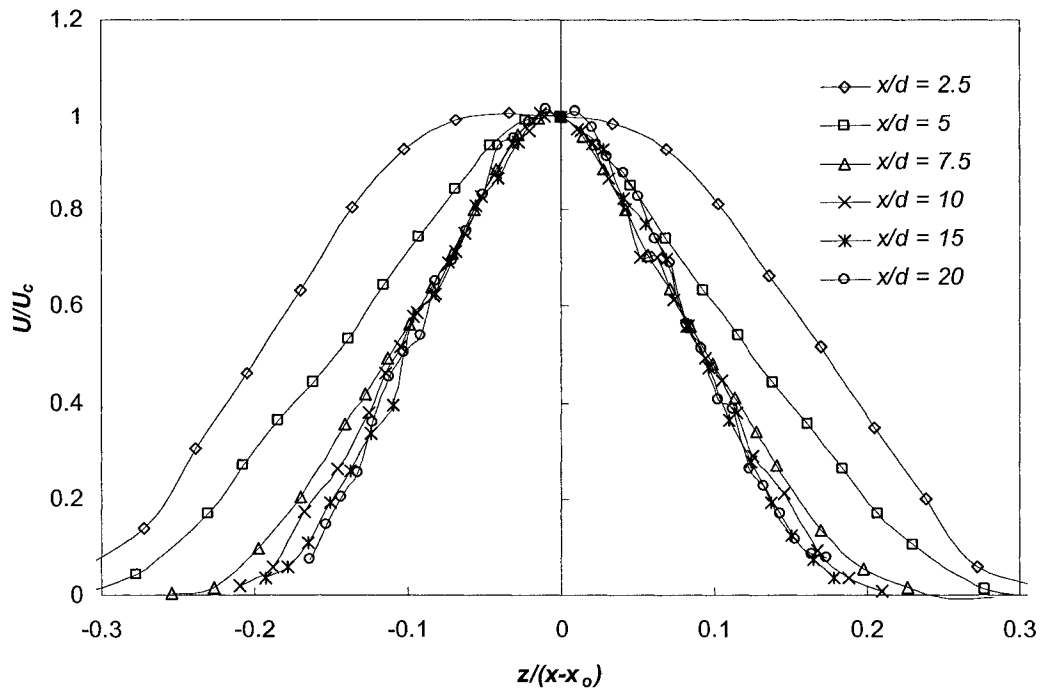
Figure 4.11: A normalized velocity plot showing profiles at various downstream locations. The dataset used to create this plot was taken along a traverse in the z-direction with the wall located at $h/d = 10$. Points connected for visual continuity.

50
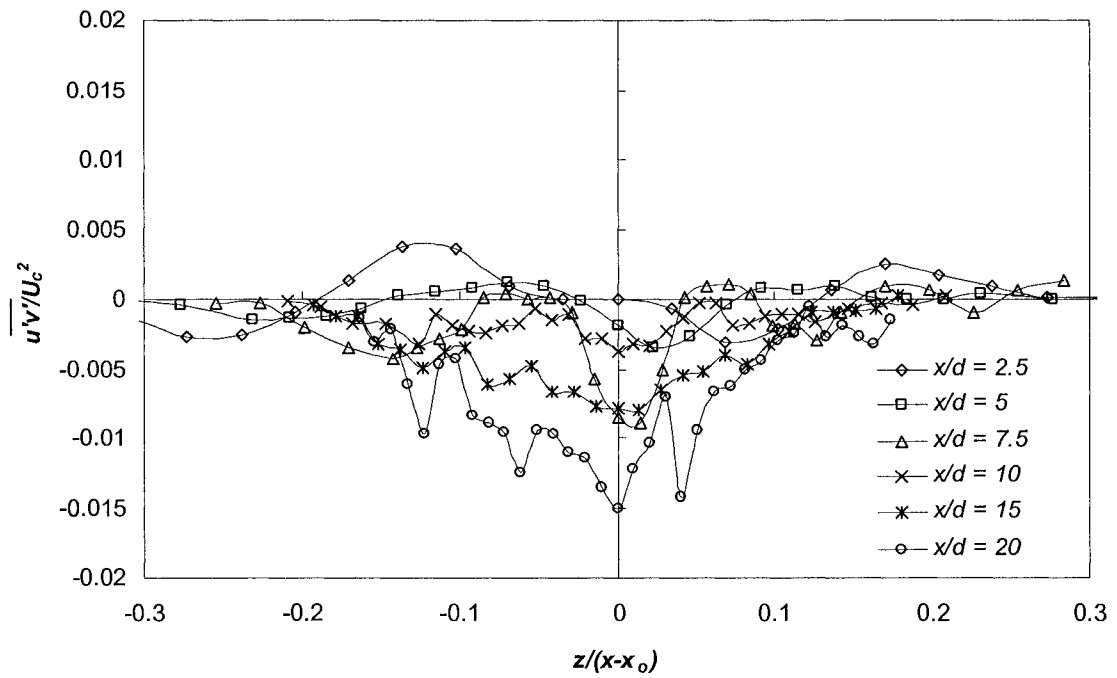
Figure 4.12: A normalized plot of Reynolds shear stress at various downstream locations. This dataset was taken along a traverse in the z-direction with the wall located at $h/d = 10$. Points connected for visual continuity.

51

Figure 4.13: Normalized plot of $\overline{u^2}$. The dataset used in this Figure was taken along a traverse in the z-direction with the wall located at $h/d = 10$. Points connected for visual continuity.
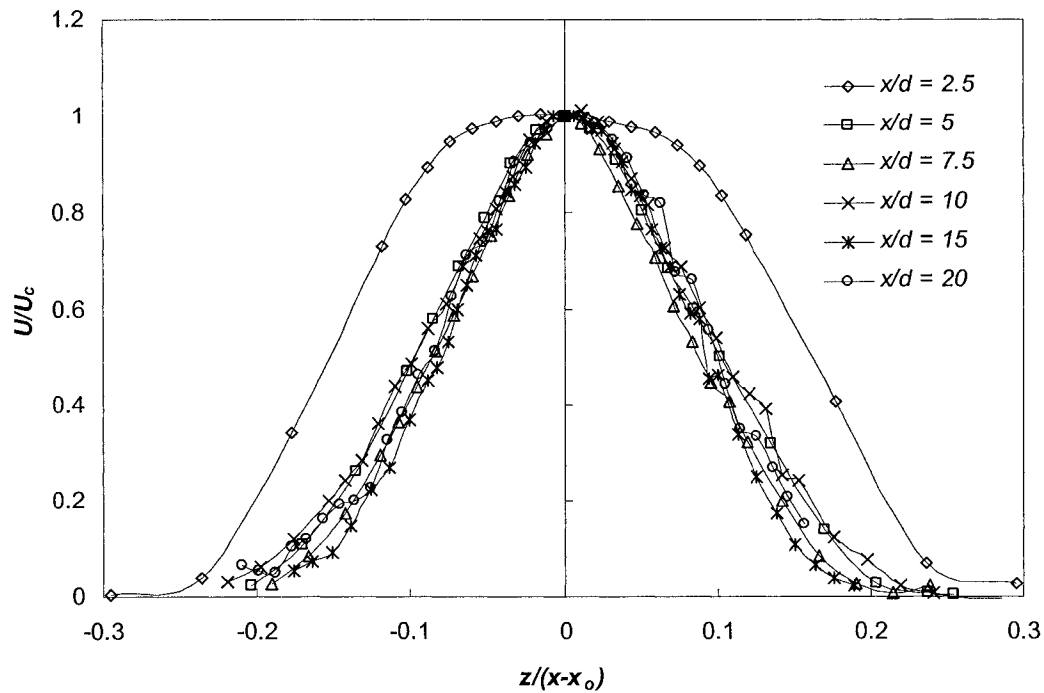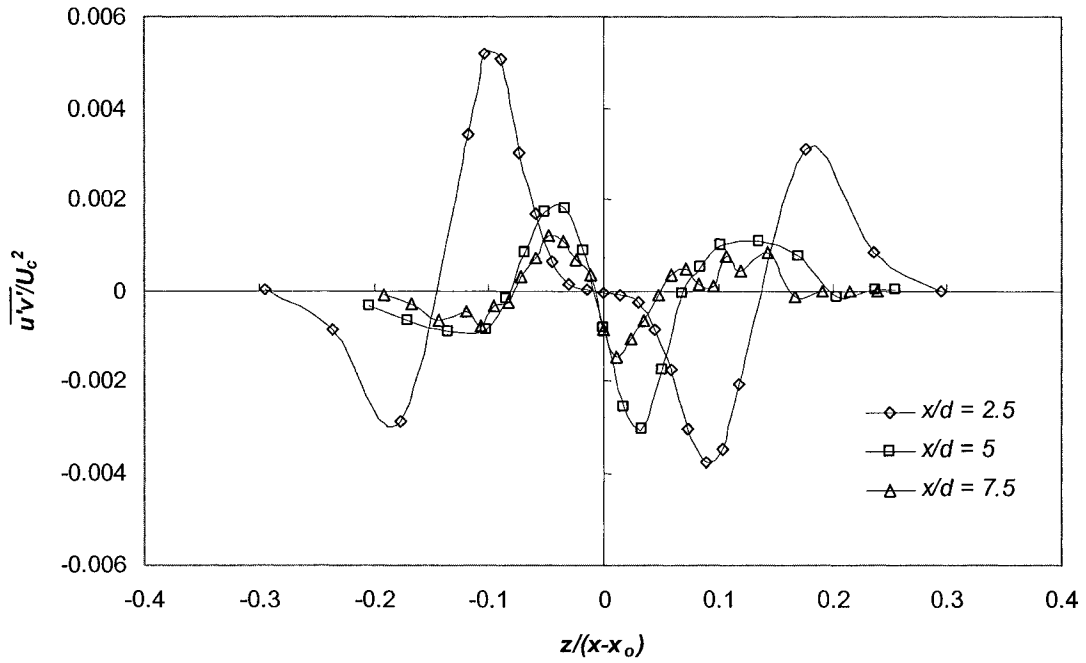
52

Figure 4.14: Normalized plot of $\overline{v^2}$. The dataset used in this Figure was taken along a traverse in the z-direction with the wall located at $h/d = 10$. Points connected for visual continuity.

Figure 4.15: A normalized velocity plot showing profiles at various downstream locations. The dataset used to create this plot was taken along a traverse in the z-direction with the wall located at $h/d = 5$. Points connected for visual continuity.

54

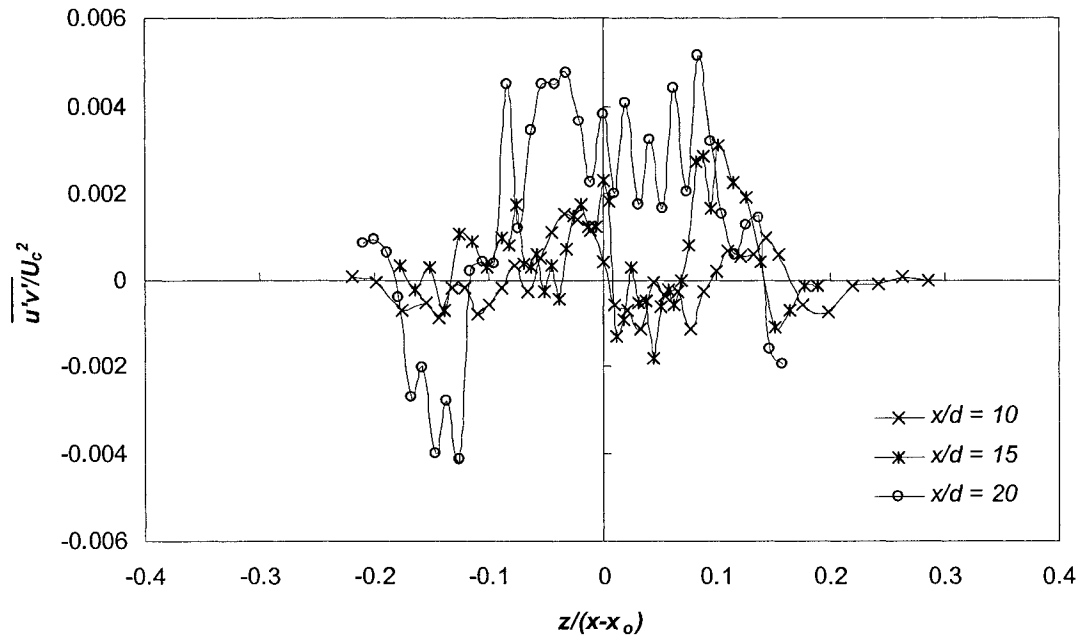**Figure 4.16: A normalized plot of Reynolds shear stress at** x/d = **2.5, 5 and 7.5.**
This dataset was taken along a traverse in the z**-direction with the wall located at**
h/d = **5. Points connected for visual continuity.**

55

Figure 4.17: A normalized plot of Reynolds shear stress at x/d = 10, 15 and 20. **This dataset was taken along a traverse in the** z-direction with the wall located at h/d = 5. **Points connected for visual continuity.**
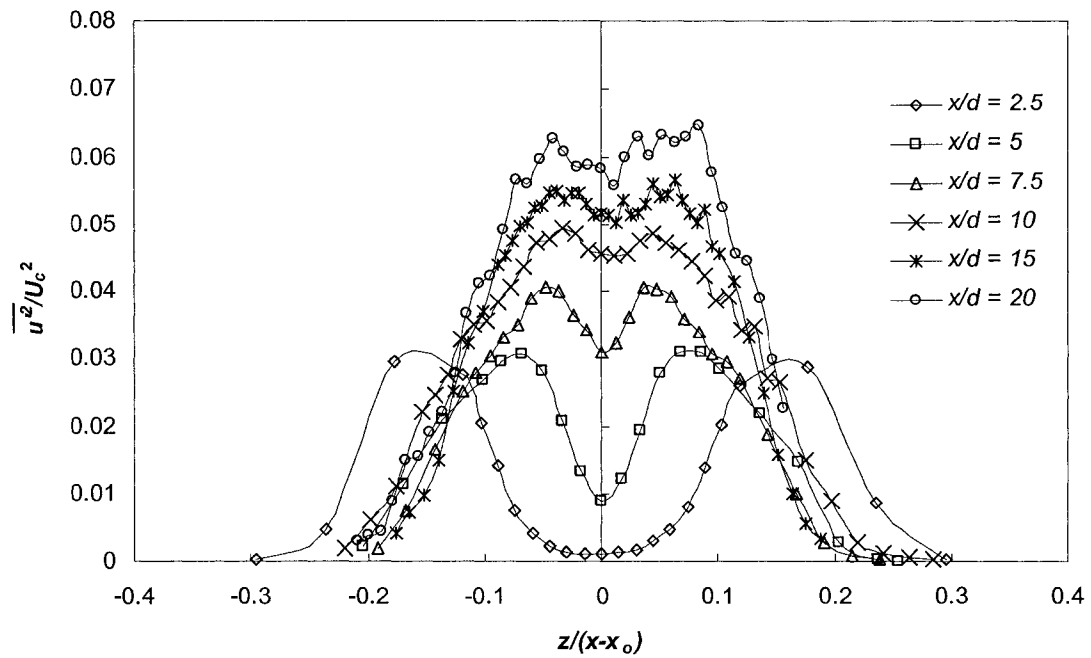
56

Figure 4.18: Normalized plot of $\overline{u'^2}$. The dataset used in this Figure was taken along a traverse in the z-direction with the wall located at h/d = 5. Points connected for visual continuity.
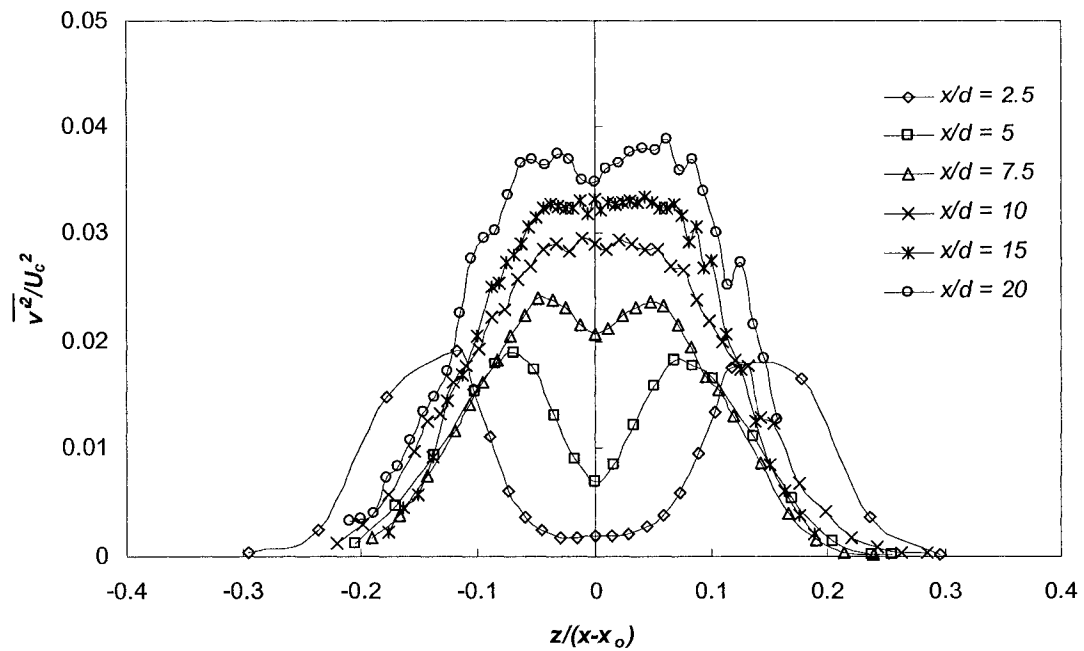
57

Figure 4.19: Normalized plot of $\overline{v'^2}$. The dataset used in this Figure was taken along a traverse in the z-direction with the wall located at $h/d = 5$. Points connected for visual continuity.
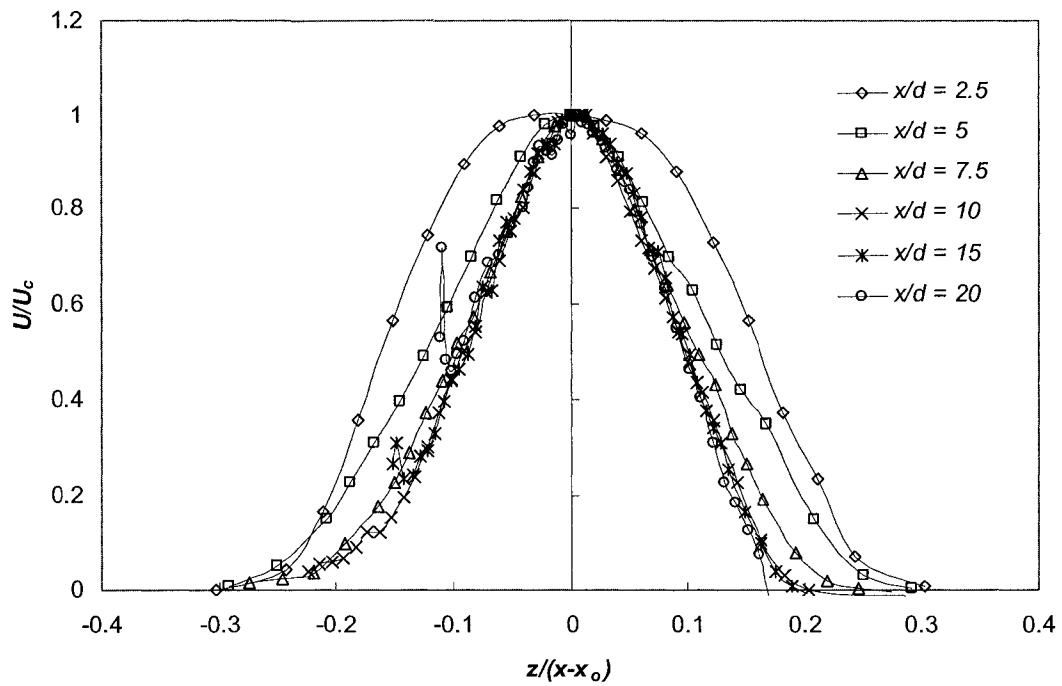
58

Figure 4.20: A normalized velocity plot showing profiles at various downstream locations. The dataset used to create this plot was taken along a traverse in the z-direction with the wall located at $h/d = 2.5$. Points connected for visual continuity.
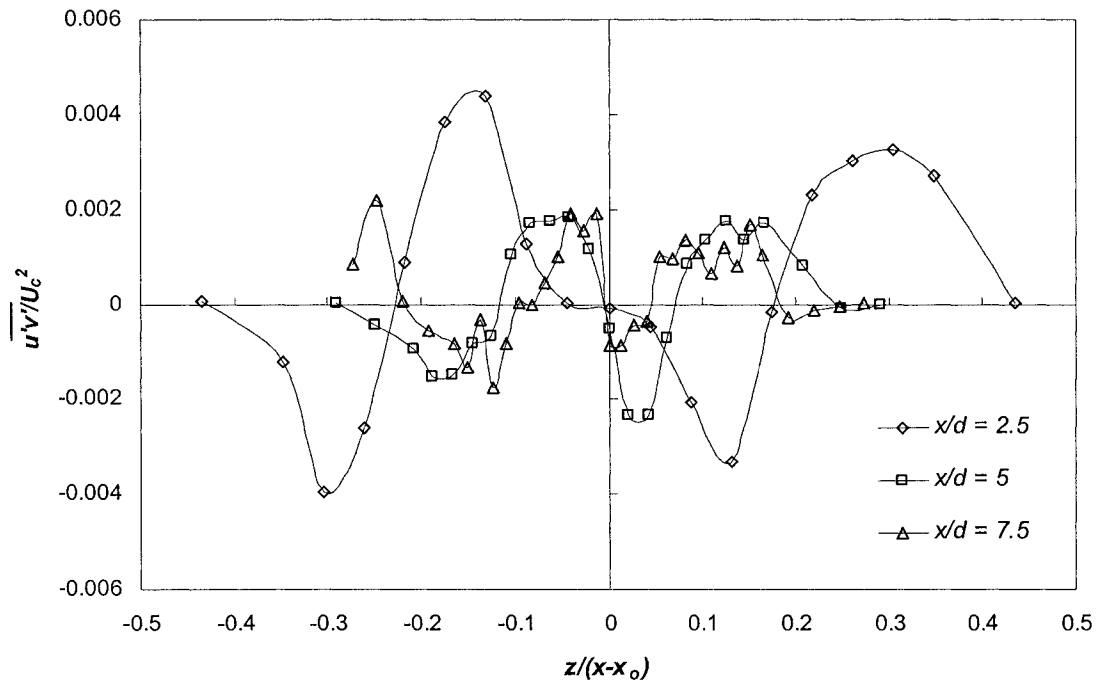
59

Figure 4.21: A normalized plot of Reynolds shear stress at x/d = 2.5, 5 and 7.5. This dataset was taken along a traverse in the z-direction with the wall located at h/d = 2.5. Points connected for visual continuity.
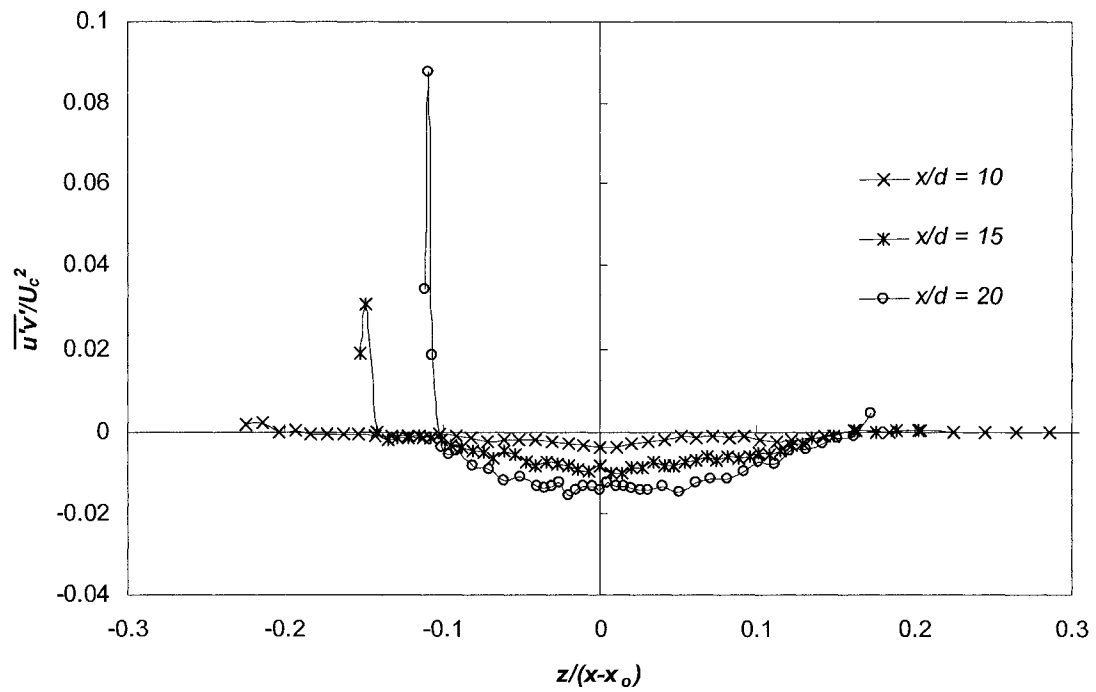
60

Figure 4.22: A normalized plot of Reynolds shear stress at x/d = 10, 15 and 20. This dataset was taken along a traverse in the z-direction with the wall located at h/d = 2.5. Points connected for visual continuity.
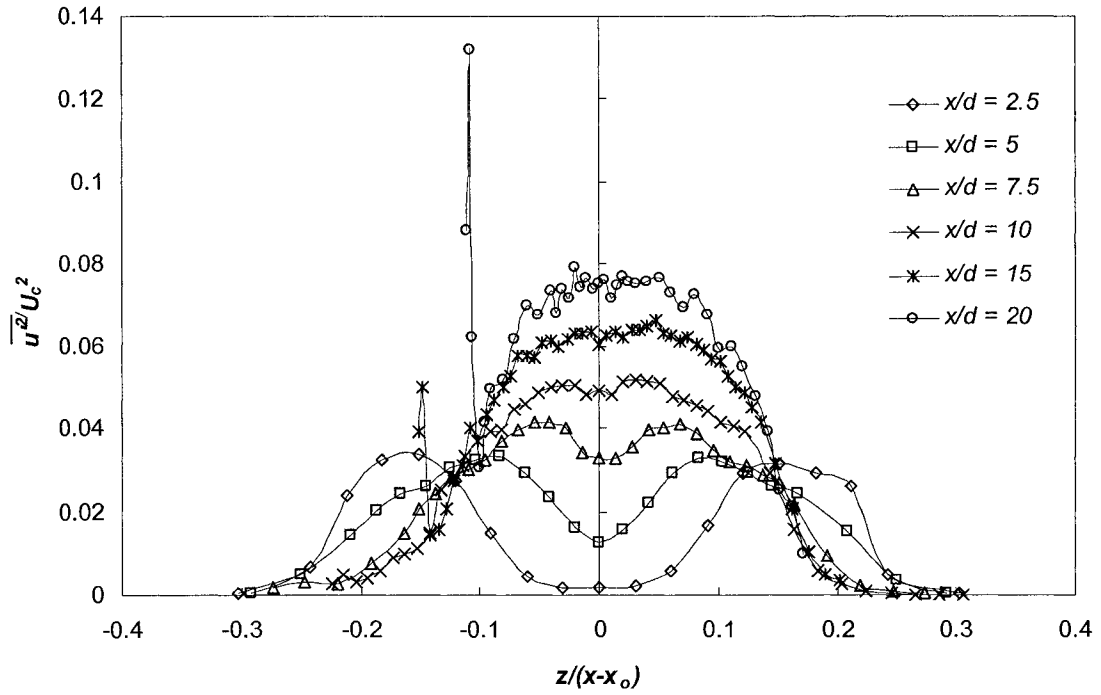
61

Figure 4.23: Normalized plot of $\overline{u'^2}$. The dataset used in this Figure was taken along a traverse in the z-direction with the wall located at h/d = 2.5. Points connected for visual continuity.

62

Figure 4.24: Normalized plot of $\overline{v'^2}$. The dataset used in this Figure was taken along a traverse in the z-direction with the wall located at $h/d = 2.5$. Points connected for visual continuity.
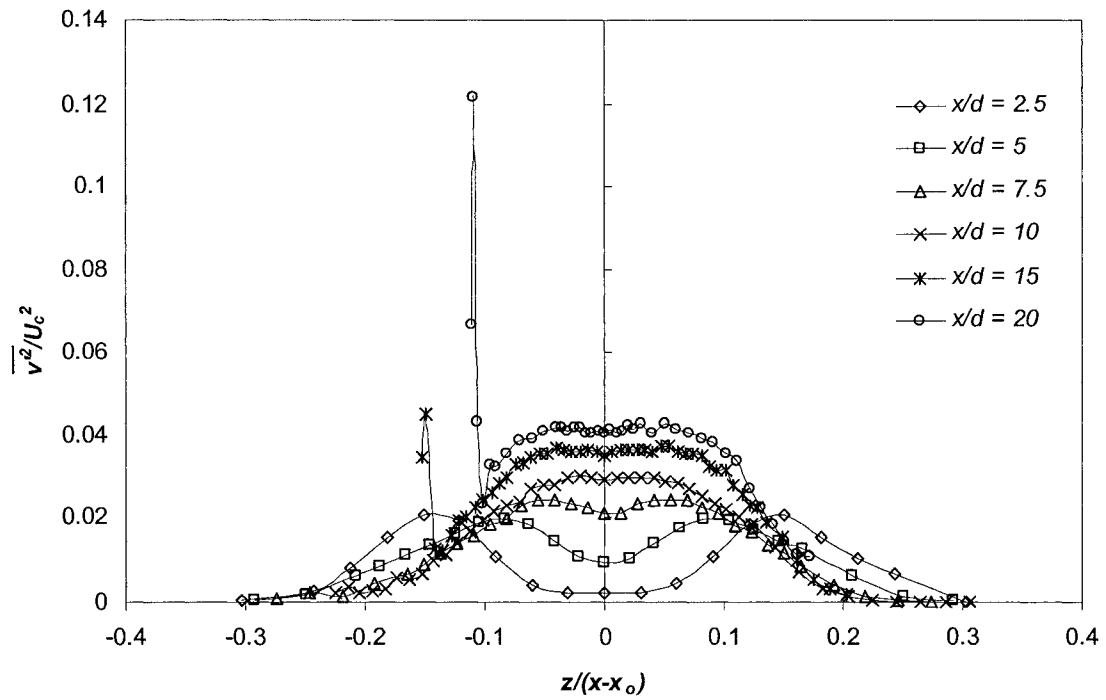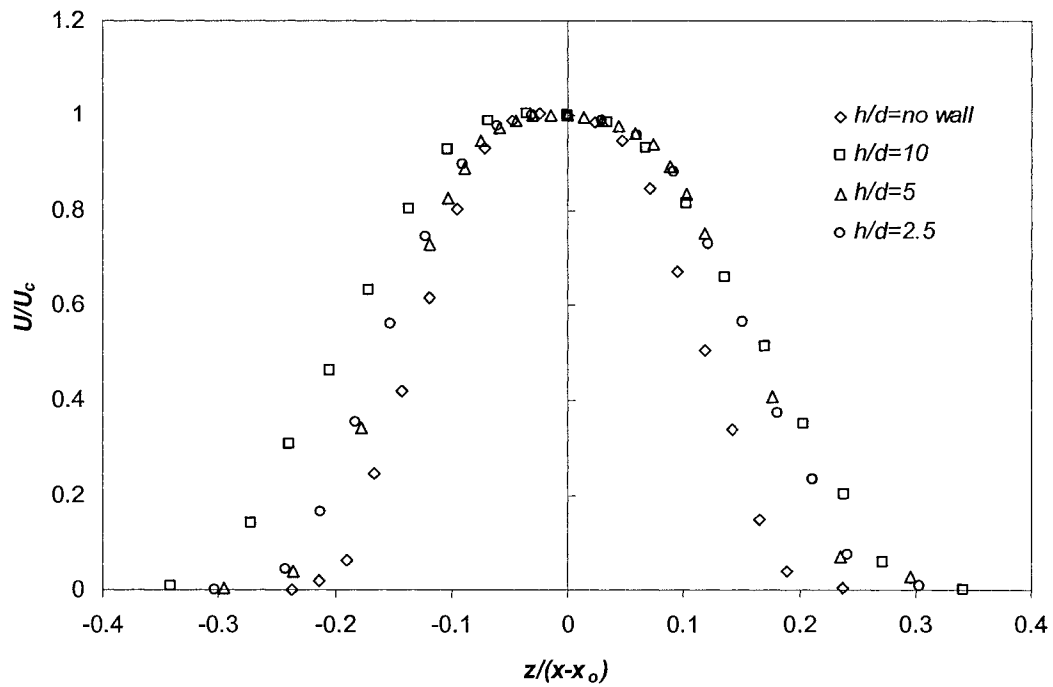
63

Figure 4.25: A normalized plot of downstream velocity profile taken at $x/d = 2.5$ with h/d = no wall, 10, 5 and 2.5. The dataset used in this plot was taken along a traverse in the z-direction.

64

Figure 4.26: Normalized plot of $\overline{u'^2}$ taken at a downstream position of $x/d = 2.5$ with h/d = no wall, 10, 5 and 2.5. The dataset used in this Figure was taken along a traverse in the z-direction.

Figure 4.27: Normalized plot of $\overline{v'^2}$ taken at a downstream position of $x/d = 2.5$ with h/d = no wall, 10, 5 and 2.5. The dataset used in this Figure was taken along a traverse in the z-direction.

66

Figure 4.28: Normalized plot of Reynolds shear stress taken at a downstream position of x/d **= 2.5 with** h/d **= no wall, 10, 5 and 2.5. The dataset used in this Figure was taken along a traverse in the** z**-direction.**

67

Figure 4.29: A normalized plot of downstream velocity profile taken at x/d = 5 with h/d = no wall, 10, 5 and 2.5. The dataset used in this plot was taken along a traverse in the z-direction.

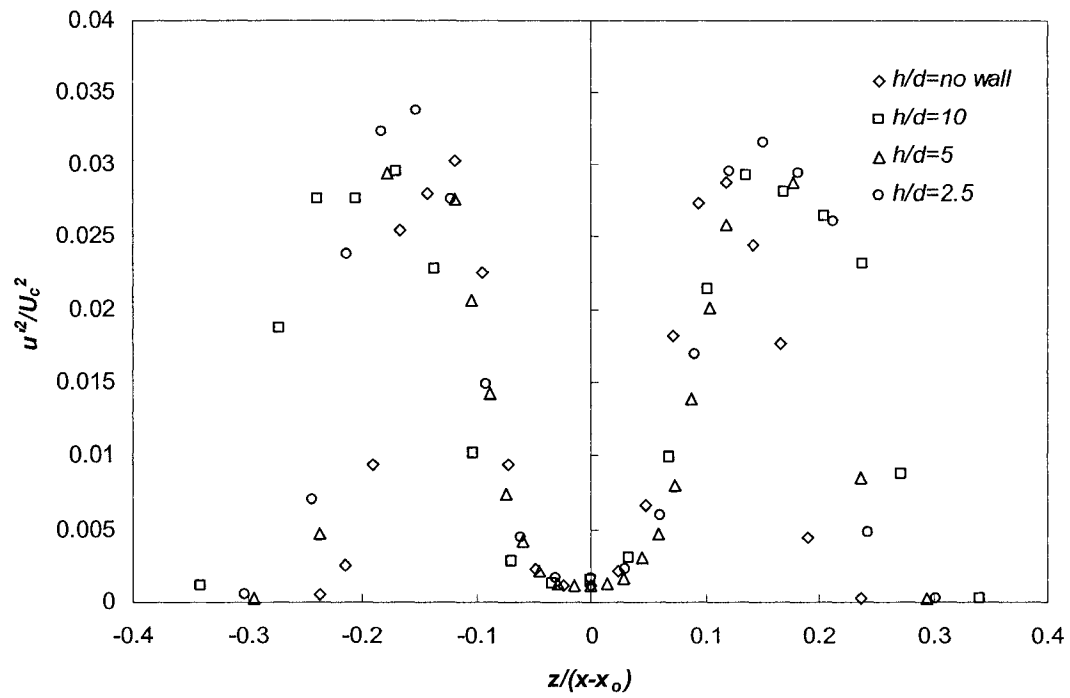Figure 4.30: Normalized plot of $\overline{u'^2}$ taken at a downstream position of $x/d = 5$ with h/d = no wall, 10, 5 and 2.5. The dataset used in this Figure was taken along a traverse in the z-direction.
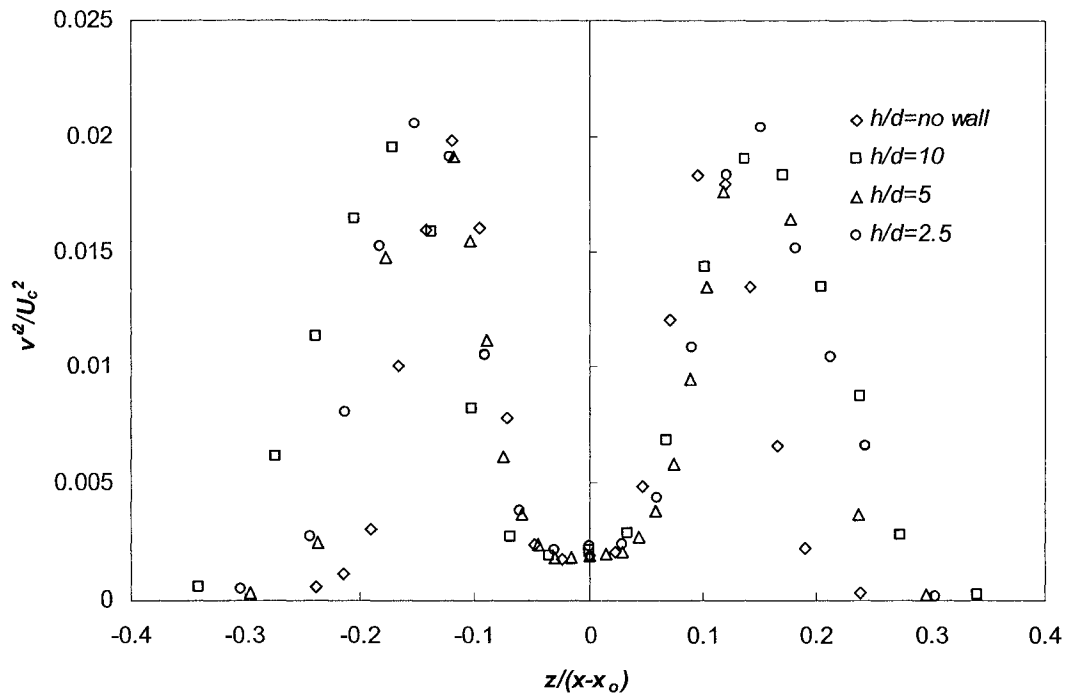
69

Figure 4.31: Normalized plot of $\overline{v'^2}$ taken at a downstream position of $x/d = 5$ with h/d = no wall, 10, 5 and 2.5. The dataset used in this Figure was taken along a traverse in the z-direction.

70

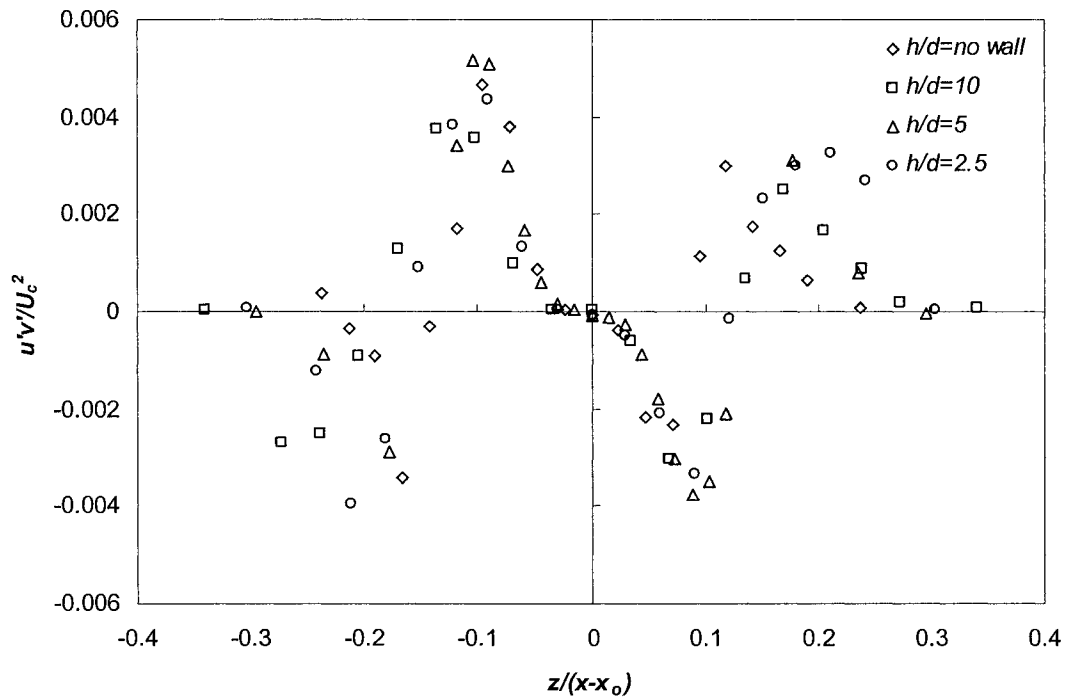**Figure 4.32: Normalized plot of Reynolds shear stress taken at a downstream position of $x/d = 5$ with h/d = no wall, 10, 5 and 2.5. The dataset used in this Figure was taken along a traverse in the z-direction.**

71

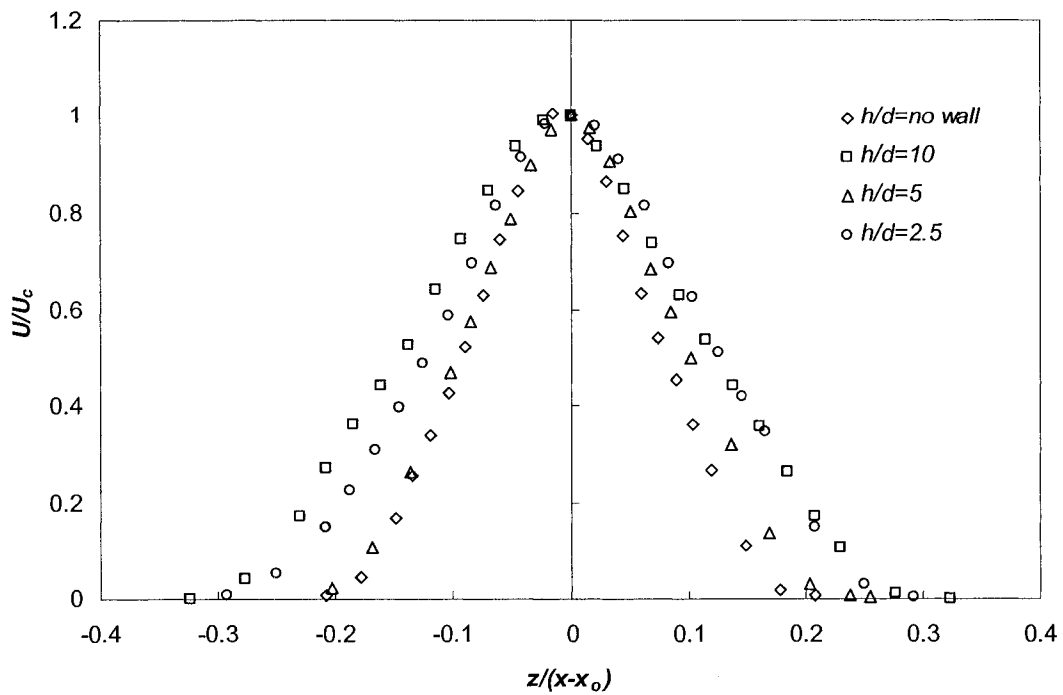**Figure 4.33: A normalized plot of downstream velocity profile taken at $x/d = 7.5$ with h/d = no wall, 10, 5 and 2.5. The dataset used in this plot was taken along a traverse in the z-direction.**
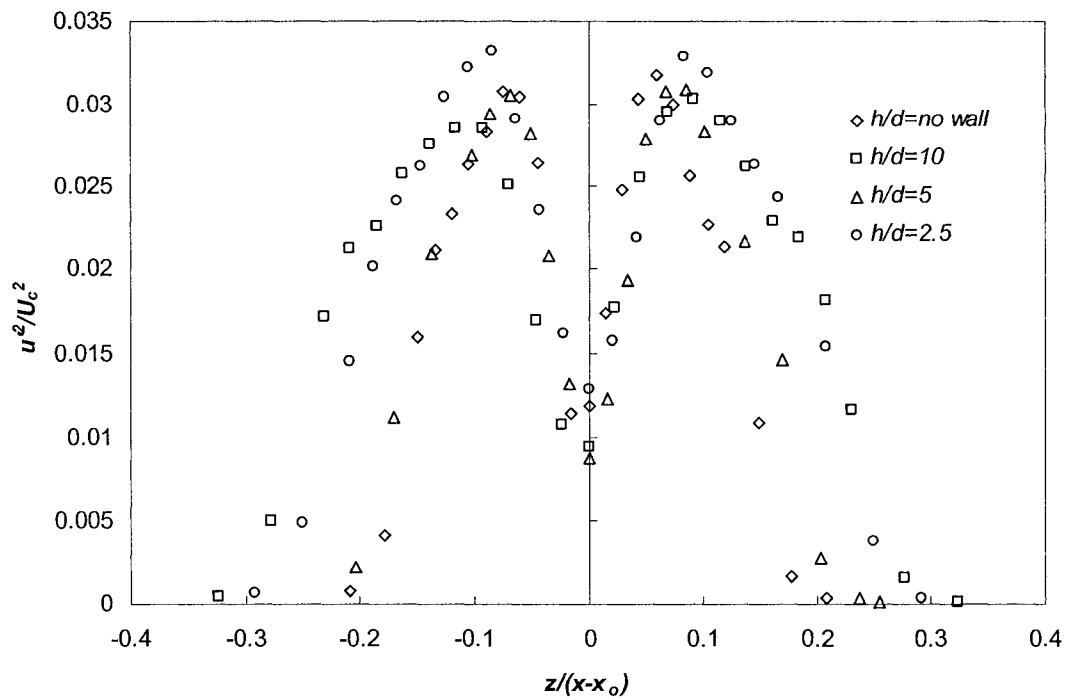
72

Figure 4.34: Normalized plot of $\overline{u'^2}$ taken at a downstream position of $x/d = 7.5$ with h/d = no wall, 10, 5 and 2.5. The dataset used in this Figure was taken along a traverse in the z-direction.

73
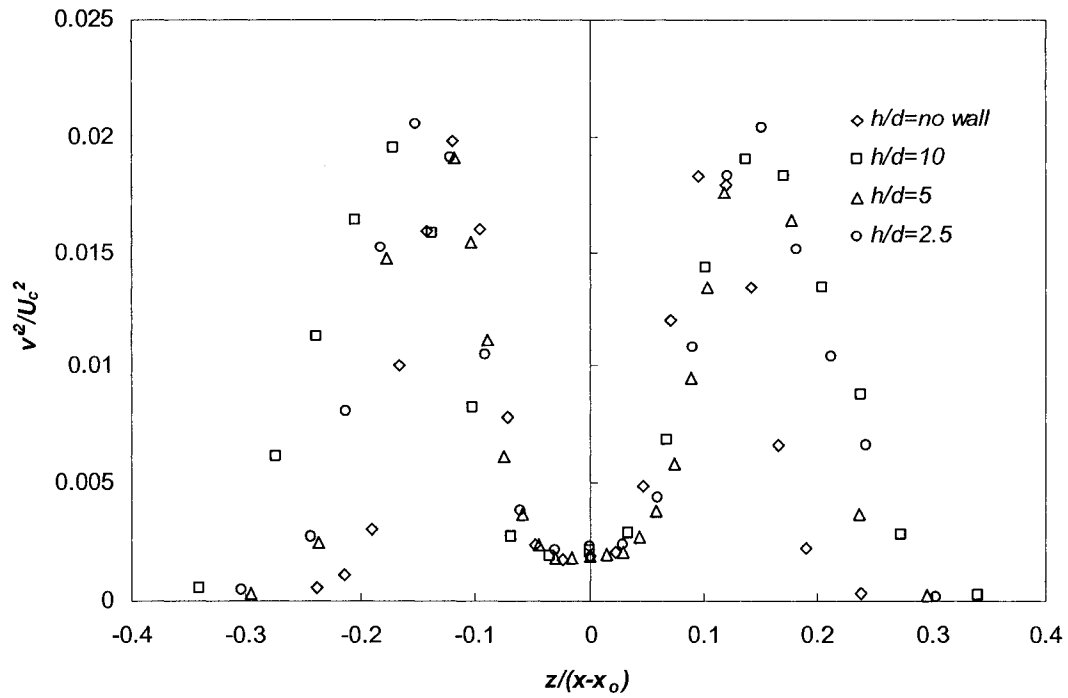
Figure 4.35: Normalized plot of $\overline{v'^2}$ taken at a downstream position of $x/d = 7.5$ with h/d = no wall, 10, 5 and 2.5. The dataset used in this Figure was taken along a traverse in the z-direction.

74

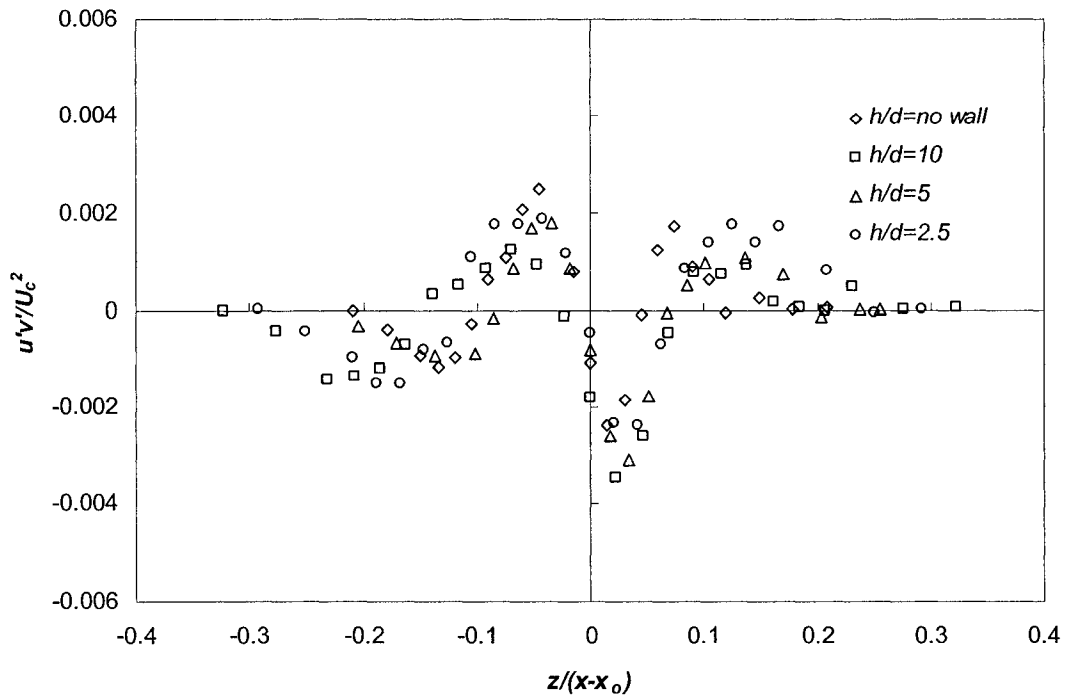Figure 4.36: Normalized plot of Reynolds shear stress taken at a downstream position of x/d = 7.5 with h/d = no wall, 10, 5 and 2.5. The dataset used in this Figure was taken along a traverse in the z-direction.

Figure 4.37: A normalized plot of downstream velocity profile taken at $x/d = 10$ with h/d = no wall, 10, 5 and 2.5. The dataset used in this plot was taken along a traverse in the z-direction.

76

Figure 4.38: Normalized plot of $\overline{u'^2}$ taken at a downstream position of $x/d = 10$ with h/d = no wall, 10, 5 and 2.5. The dataset used in this Figure was taken along a traverse in the z-direction.

77

Figure 4.39: Normalized plot of $\overline{v'^2}$ taken at a downstream position of $x/d = 10$ with $h/d =$ no wall, 10, 5 and 2.5. The dataset used in this Figure was taken along a traverse in the z-direction.
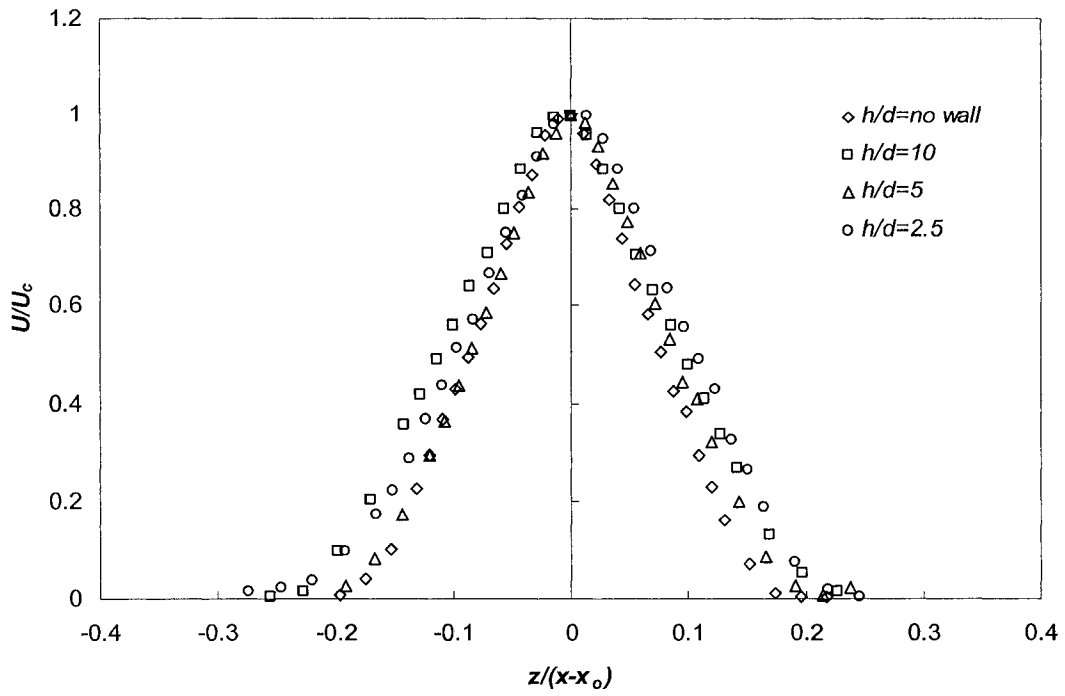
78

Figure 4.40: Normalized plot of Reynolds shear stress taken at a downstream position of $x/d = 10$ with $h/d =$ no wall, 10, 5 and 2.5. The dataset used in this Figure was taken along a traverse in the z-direction.

79

Figure 4.41: A normalized plot of downstream velocity profile taken at $x/d = 15$ with h/d = no wall, 10, 5 and 2.5. The dataset used in this plot was taken along a traverse in the z-direction.

80
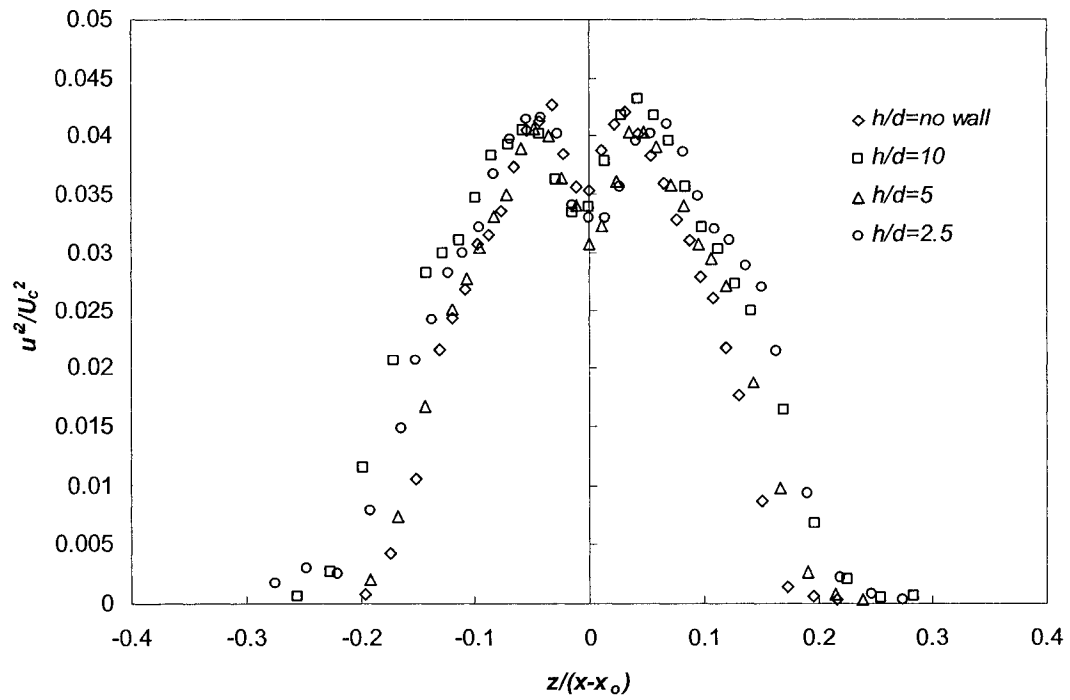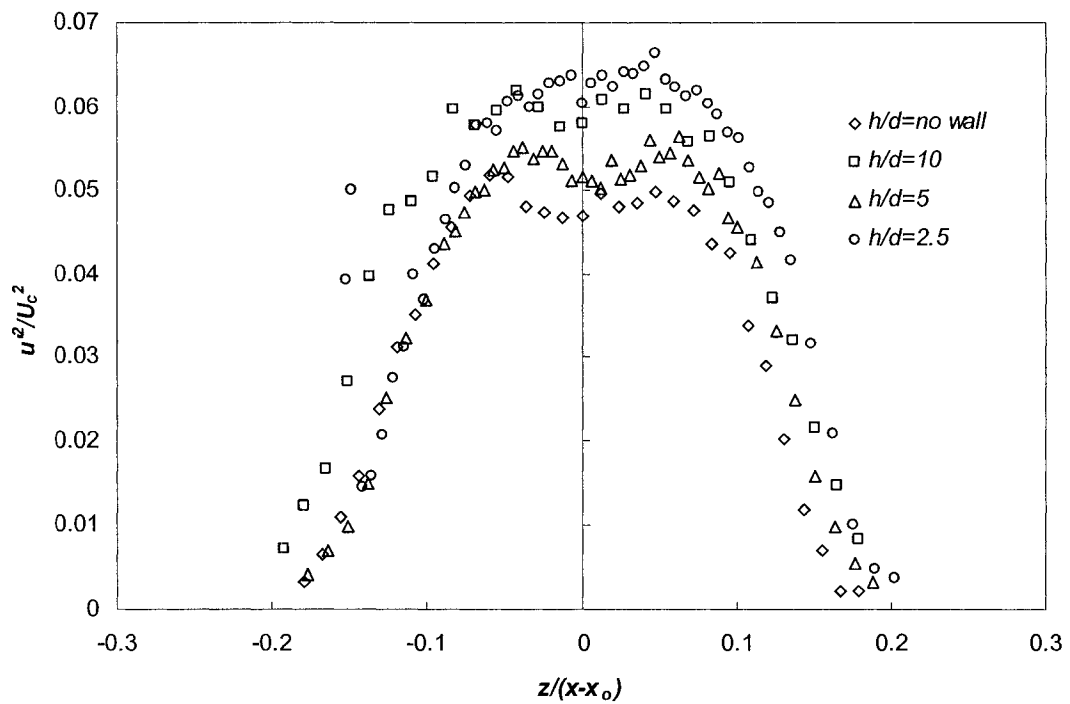
Figure 4.42: Normalized plot of $\overline{u'^2}$ taken at a downstream position of $x/d = 15$ with $h/d =$ no wall, 10, 5 and 2.5. The dataset used in this Figure was taken along a traverse in the z-direction.
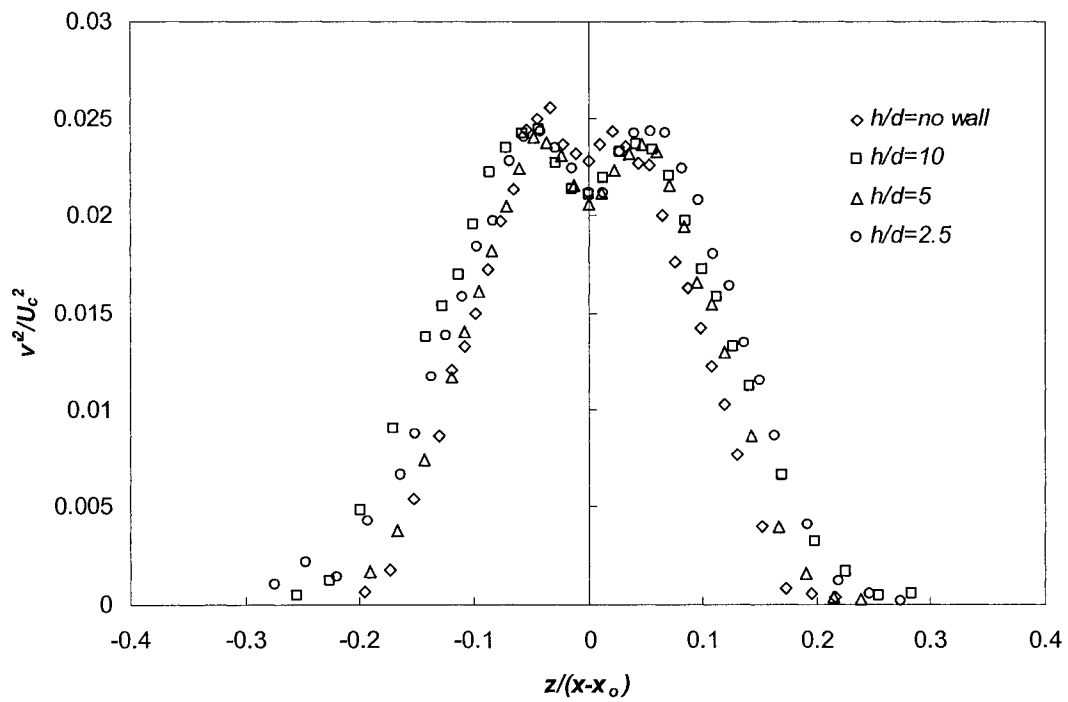
81
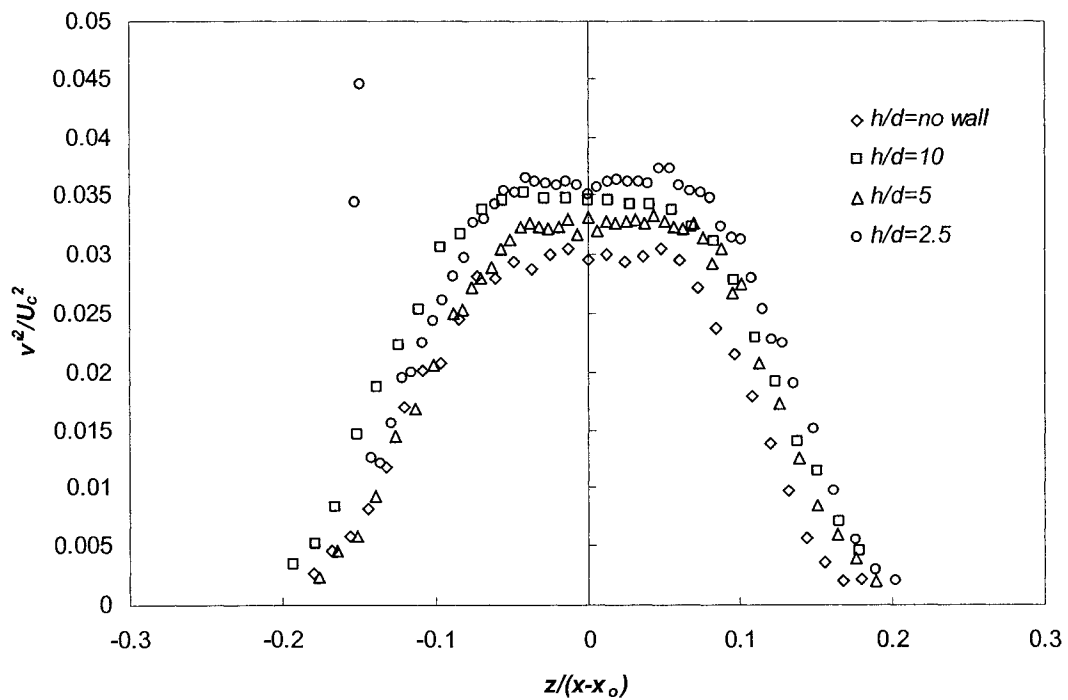
Figure 4.43: Normalized plot of $\overline{v'^2}$ taken at a downstream position of $x/d = 15$

with h/d = no wall, 10, 5 and 2.5. The dataset used in this Figure was taken along

a traverse in the z-direction.

82
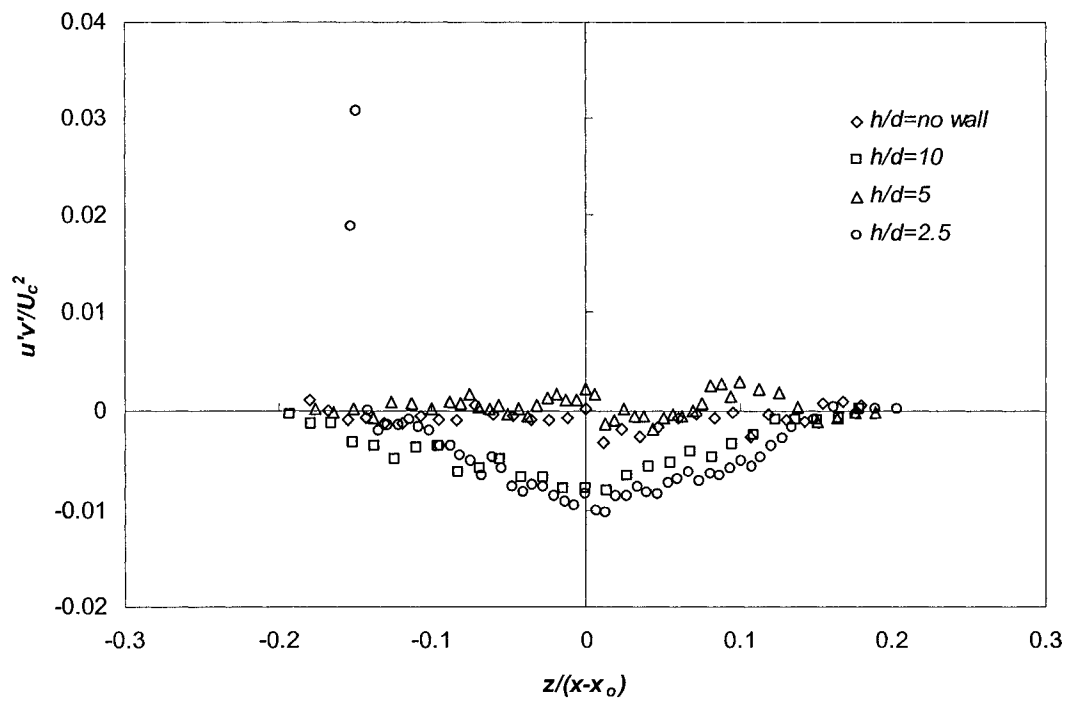
Figure 4.44: Normalized plot of Reynolds shear stress taken at a downstream position of $x/d = 15$ with $h/d =$ no wall, 10, 5 and 2.5. The dataset used in this Figure was taken along a traverse in the z-direction.
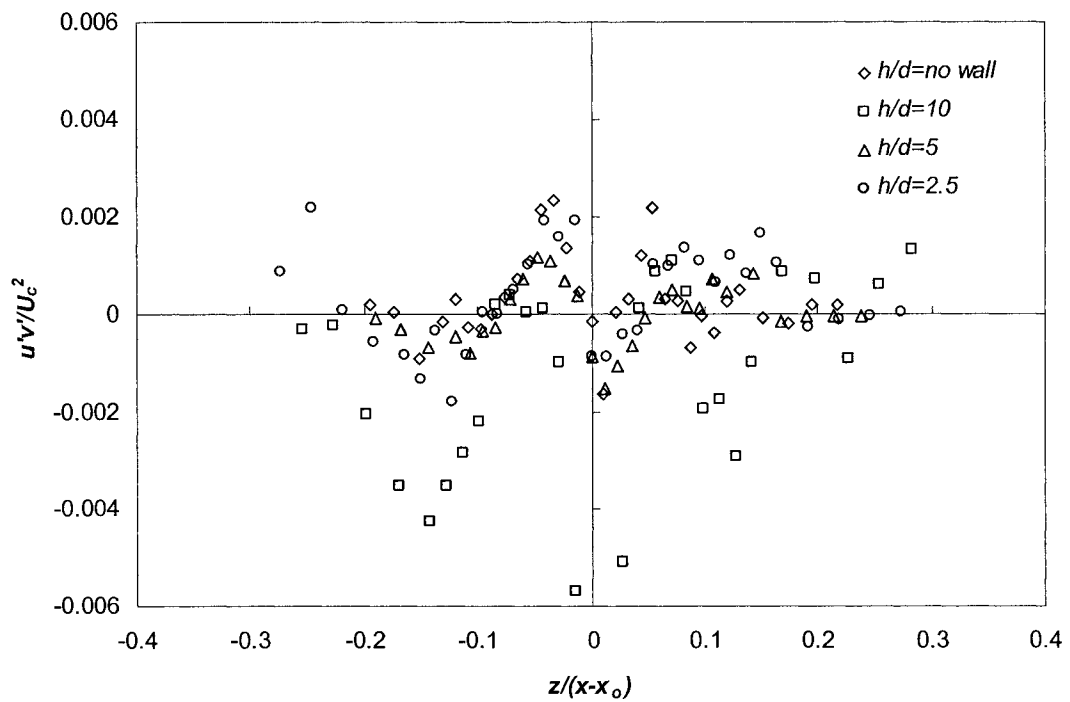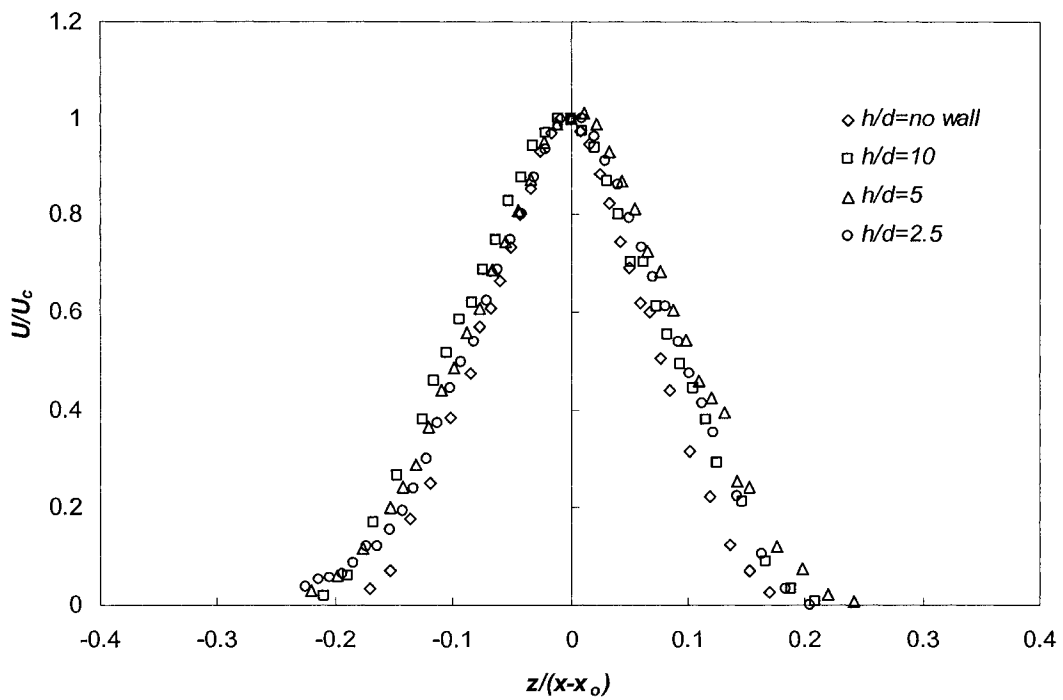
83
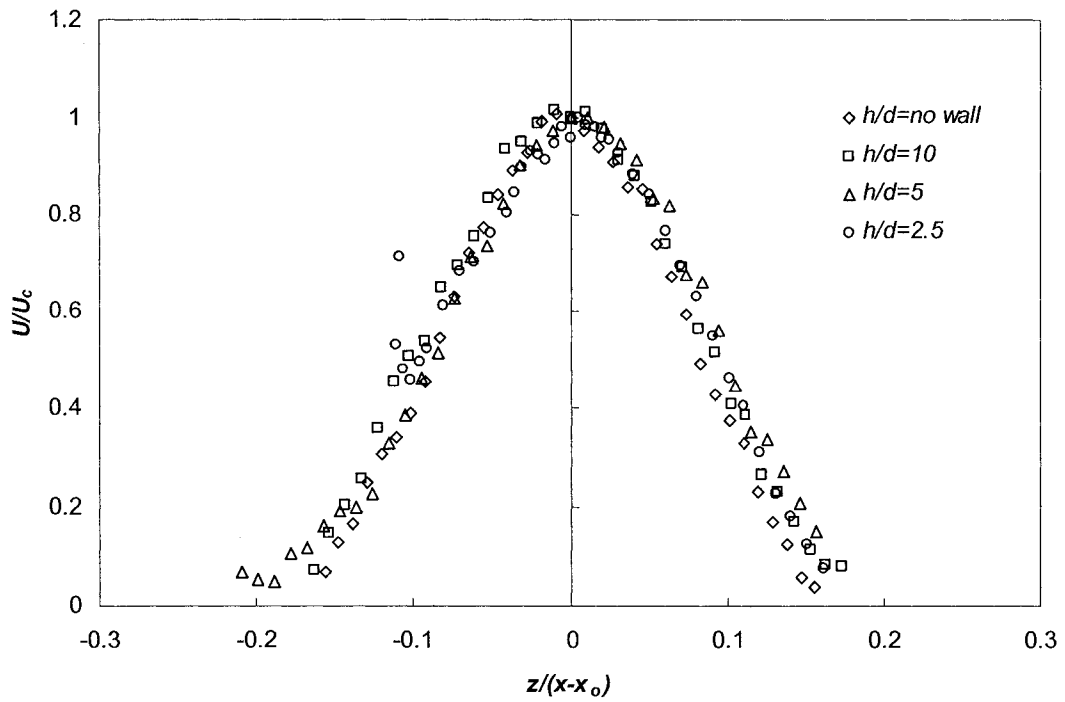
Figure 4.45: A normalized plot of downstream velocity profile taken at $x/d = 20$ with h/d = no wall, 10, 5 and 2.5. The dataset used in this plot was taken along a traverse in the z-direction.
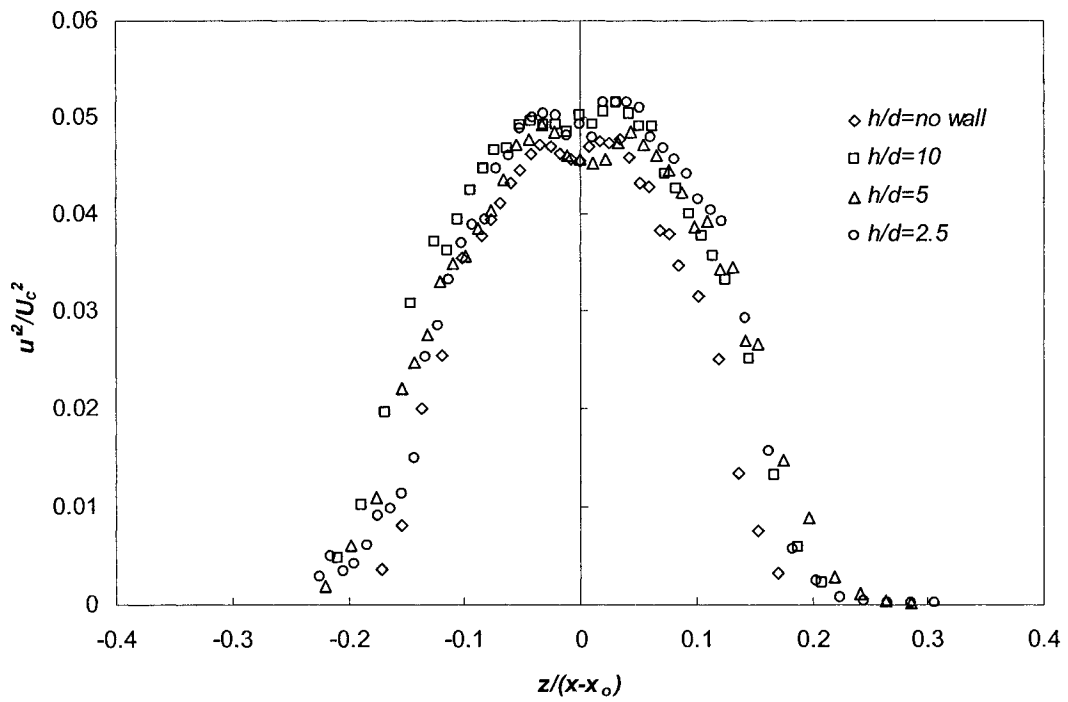
84
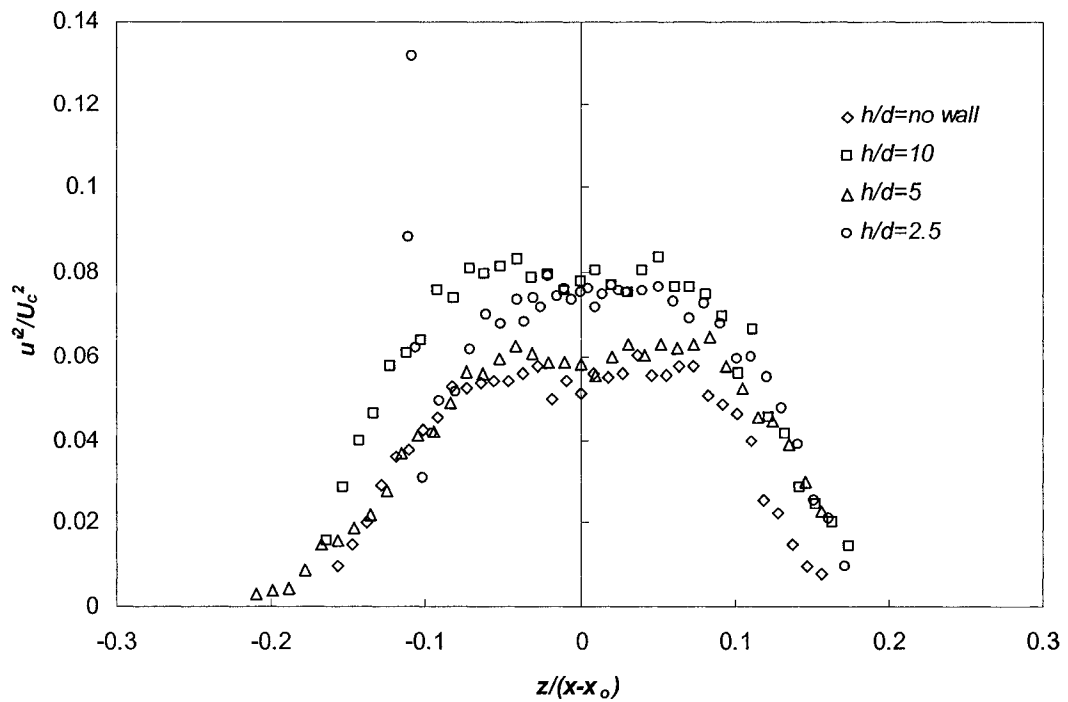
Figure 4.46: Normalized plot of $\overline{u'^2}$ taken at a downstream position of x/d = 20 with h/d = no wall, 10, 5 and 2.5. The dataset used in this Figure was taken along a traverse in the z-direction.

85
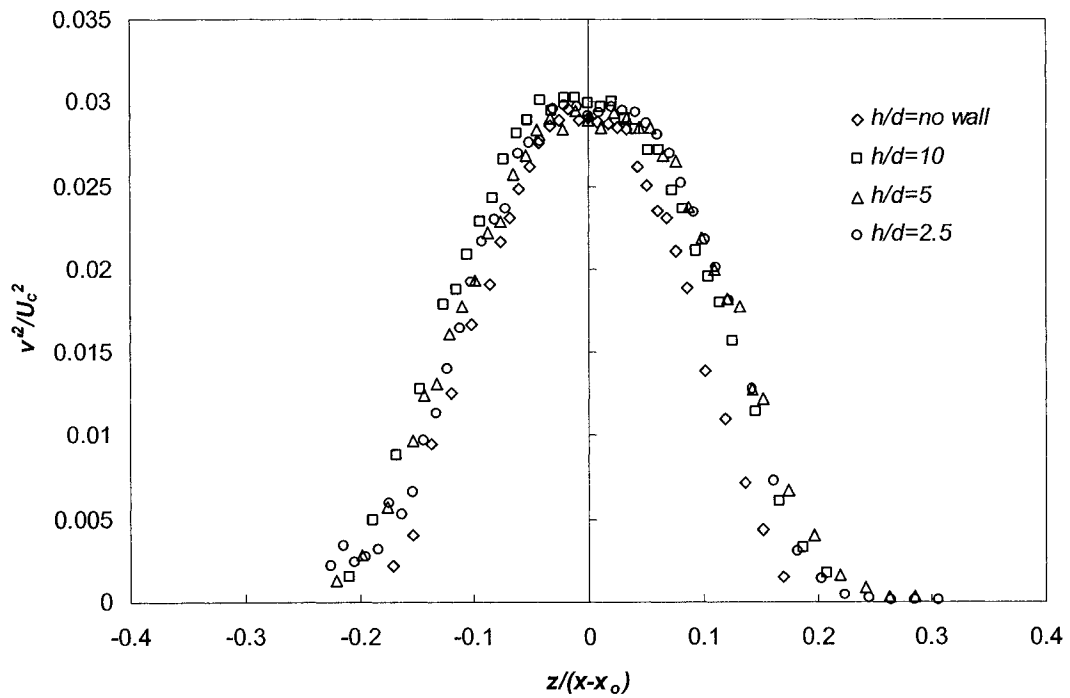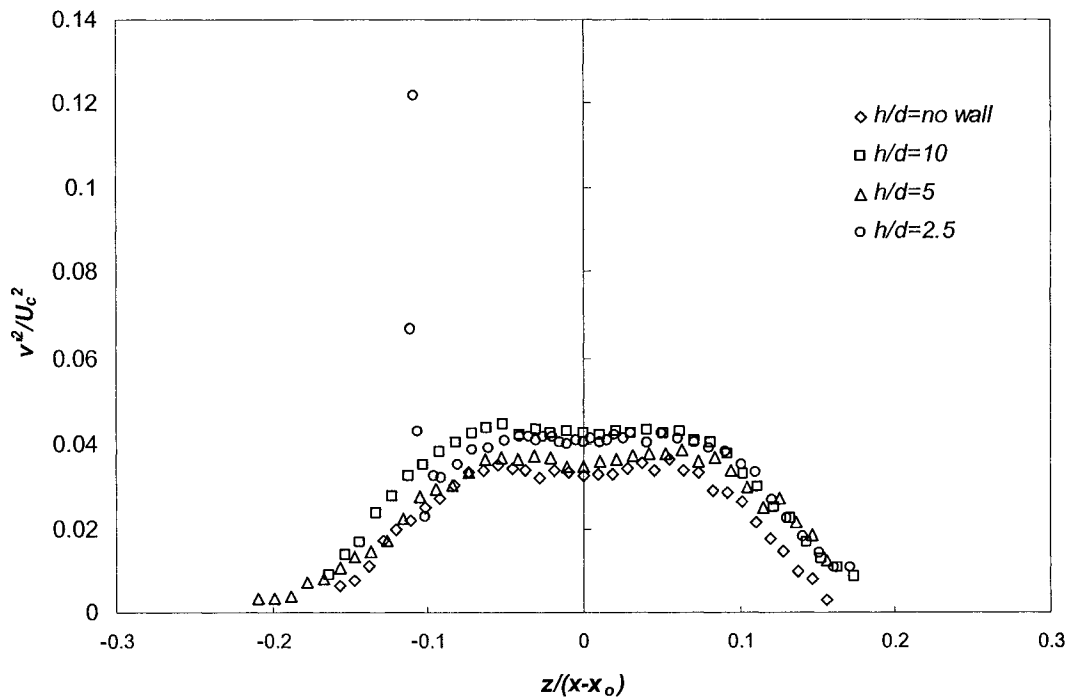
Figure 4.47: Normalized plot of $\overline{v'^2}$ taken at a downstream position of $x/d = 20$ with h/d = no wall, 10, 5 and 2.5. The dataset used in this Figure was taken along a traverse in the z-direction.
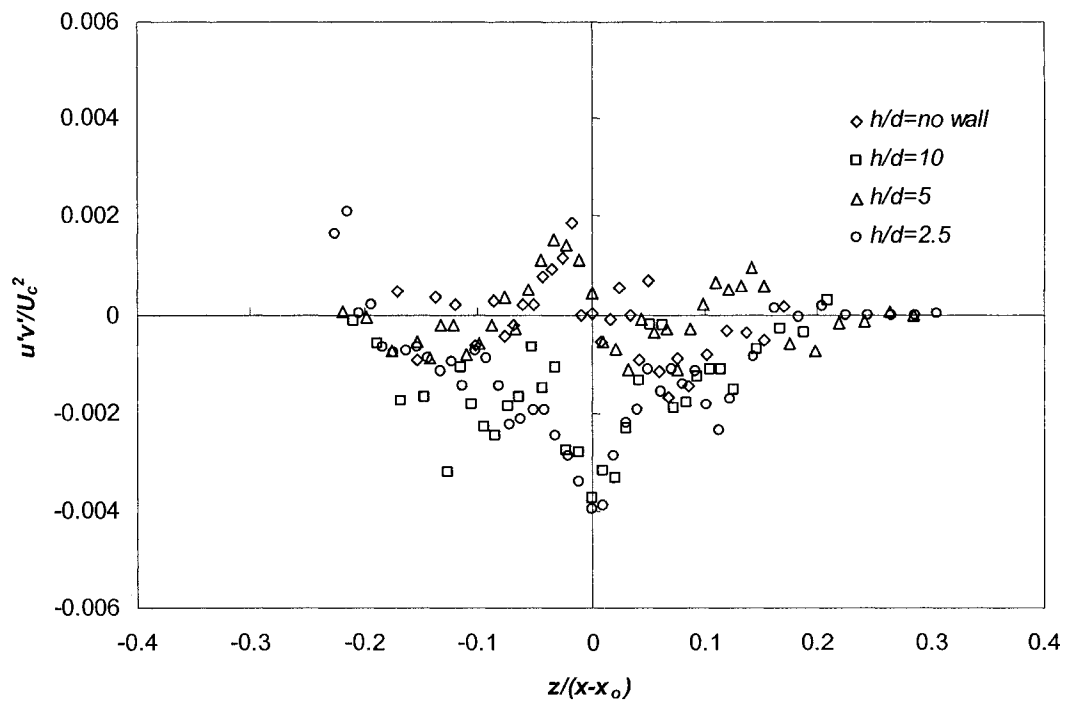
86
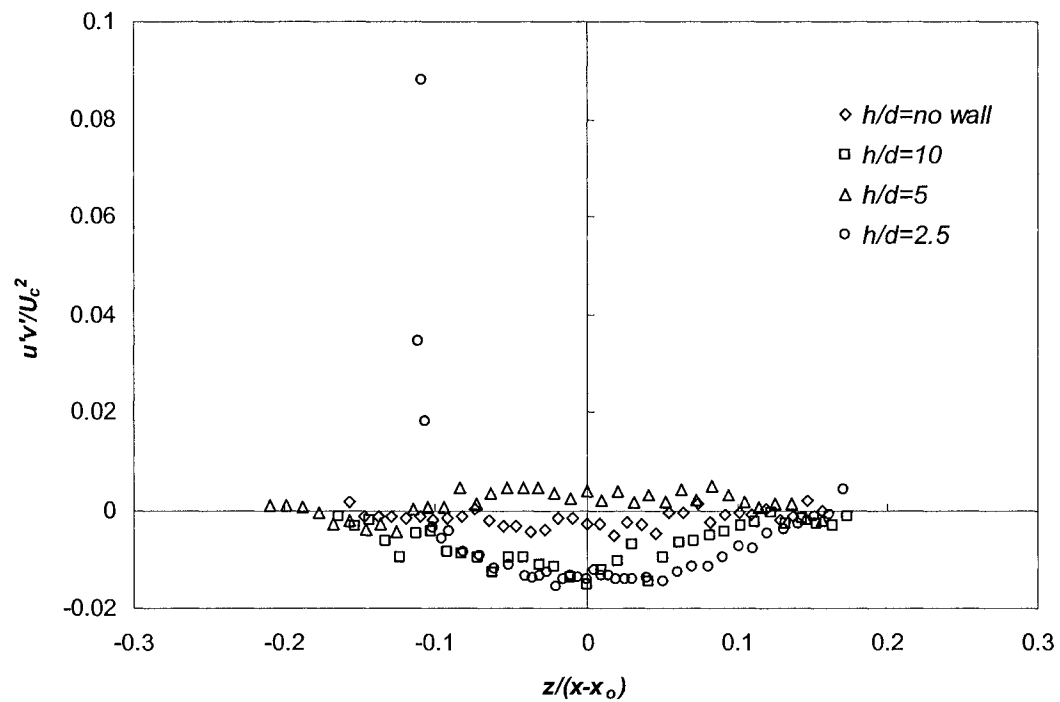
Figure 4.48: Normalized plot of Reynolds shear stress taken at a downstream

position of x/d = 20 with h/d = no wall, 10, 5 and 2.5. The dataset used in this

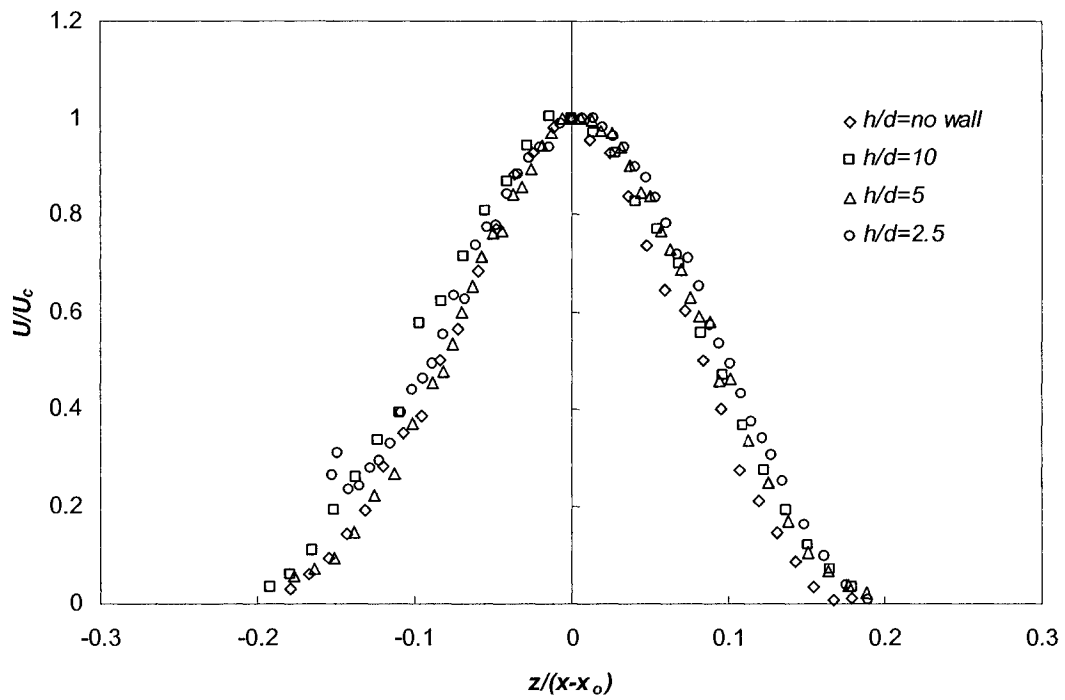Figure was taken along a traverse in the z-direction.

87

# Chapter 5: Discussion of Results

5.1 The Free Jet

Free jet data taken in this experiment needed to be verified against data taken by other researchers. Of particular interest was the second order moments presented in Chapter 4 recorded along a y traverse. It should be noted that in any shear flow the mean velocity profiles appear self similar long before higher order moments. Since measurements were only taken in the near field of the jet it is not surprising that self similarity was only truly achieved for the mean flow profiles.

The Reynolds shear stress results obtained in HCG94 are shown in Figure 5.1 plotted along with the results of Section 4.2 of this thesis. It can be seen that the shear stress obtained by Hussein et al. are larger than the results obtained during this experiment. The maximum normalized shear stress obtained in HCG94 was 0.0205 and occurred at $y/(x-x_o)$ = 0.08. The maximum normalized shear stress obtained in Section 4.2 of this thesis is 0.015 and occurred at $y/(x-x_o)$ = 0.07. This makes the maximum shear stress in presented Section 4.2 of this thesis 26% smaller than the results in HCG94. This result can be attributed to the enclosure affecting the development of the jet. It could also be hypothesized that the markedly different values of shear stress could be a function of the different downstream stations the measurements were taken at. This hypothesis can be dismissed since the shear stress in Section 4.2 appears to be quickly approaching self-similarity and it is doubtful it would increase in magnitude by 26% before self similarity was achieved.

88

Figure 5.2 is a plot similar to Figure 4.5 with the $\overline{u'^2}$ data from HCG94 included. The presence of a downstream off axis peak in Figure 5.2 is also consistent with data found in HCG94, Fukushima et al (2000), and others. This off axis peak in axial normal stress is caused by a peak in the production of turbulence kinematic energy working against the mean shear. This is different from the off axis peak found in the near field which is a footprint of the jets low turbulence potential core. In the data presented in Figure 5.2 the off axis peak occurs at $y(x-x_o) = 0.05$. This is close to the 0.04 value obtained by HCG94 and matches the 0.05 value obtained by Fukushima. As with the Reynolds shear stress, the values obtained for the peak axial normal stress are considerably smaller than the maximum found in HCG94. The peak value obtained by HCG94 was 0.085 while the maximum obtained in this experiment was 37% smaller. This again can be attributed to the enclosure influencing jet development.

The normalized $\overline{v'^2}$ Reynolds stress of HCG94 was also compared to the data presented in Section 4.2 and is shown in Figure 5.3. The comparison made in Figure 5.3 shows how the data from Section 4.2 obtains a considerably smaller maximum value than the data obtained in HCG94. The data from Section 4.2 is also smaller than data found in Fukushima et al (2000) and Wygnanski et al (1969). As stated before, the data from Section 4.2 was taken closer to the exit of the nozzle than the data taken by the authors previous mentioned. The maximum value in the $\overline{v'^2}$ plot would undoubtedly get larger in magnitude as the downstream distance was

89

increased; however it is unlikely that it would be able to increase enough to make up the 41% difference. It is also notable that no off axis peak in $\overline{v'^2}$ is found at downstream locations. This is consistent with what is found in available literature.

The decreased magnitude of Reynolds shear stress, $\overline{u'^2}$ as well as $\overline{v'^2}$, when compared to the works of others, is likely caused by the enclosure geometry used in this experiment.

5.2 Jet with interior wall included

The effect of the location of the interior wall on the Reynolds stresses will be discussed in this section. Figure 5.4 is a plot of all of the Reynolds normal stresses made from a z traverse in Chapter 4. It can be seen that the wall position does influence the development of the off axis peak in $\overline{u'^2}$ at downstream locations. Small off axis peaks are found for the no wall case, as well as $h = 10d$ and $5d$. The off axis peak in $\overline{u'^2}$ is not seen for $h = 2.5d$. There are two possibilities why this is. The presence of the wall 2.5 diameters from the jet centerline could delay the onset of the off axis peak in $\overline{u'^2}$ so it would not occur until $x/d > 20$. The other possibility is that the presence of the wall completely removes this peak from the flow. This would mean that the wall has a dramatic effect on the ability of the Reynolds stresses to work against the mean shear. There is no clear pattern on how the wall or enclosure affects the magnitude of the maximas found in the $\overline{u'^2}$ plots of Figure 5.4.

90

The plots of $\overline{v'^2}$ also show no dramatic changes as the interior wall is moved closer to the jet centerline. The maximum value in $\overline{v'^2}$ is smallest when no interior wall is present but no clear pattern can be observed to determine a relationship between the wall to jet distance h, and the overall shape or size of the $\overline{v'^2}$ plots. In the future more measurements could be taken with the wall in a greater number of positions in order to determine if any pattern exists for either $\overline{u'^2}$ or $\overline{v'^2}$.

Figure 5.5 is a collection of Reynolds shear stress plots made along a y traverse from Chapter 4. The most notable feature of the plots is the nonzero values for Reynolds shear at the jet centerline. There are a few possible explanations for this. One explanation is that the measurements were not actually taken at the jet centerline. It is possible that the Coanda effect caused the jet to deflect so measurements were not actually being taken at the jet centerline since the centerline shifted as the jet developed downstream. This is unlikely since the Coanda effect would have pushed the jet in the negative z direction and a zero shear stress still would have been observed, although it would be shifted towards the wall. It is also possible that the jet wasn't aligned properly so the jet centerline was not parallel to the x axis and had a small z component as well. This misalignment would become increasingly noticeable as measurements were taken further downstream. Again this is not a likely possibility since any misalignment would have remained constant each time the wall to jet distance h was changed given that the nozzle was never moved during the experiment.

91

Another possible cause for the non-zero measurement is the asymmetry in the enclosure boundary conditions. The top of the enclosure used in this experiment was a free surface, while the ends, bottom and sides were made of glass. This resulted in a zero velocity boundary condition along the bottom, ends and sides, and a zero shear condition along the top of the enclosure. The implications of this free surface are that no wall shear stress exists at the top boundary of the enclosure. This asymmetry in velocity boundary conditions, which was considered insignificant when the experiments were being carried out, could have had a greater effect on the experimental results than originally thought.

Figure 5.6 is a schematic showing the asymmetrical boundary conditions inside the experimental apparatus. When more of the re-circulating flow is on the top of the jet, this could cause the jet to be deflected downward. This downward (or negative y) deflection would not be noticed in the mean velocity profiles or the $\overline{u'^2}$ or $\overline{v'^2}$ plots since these plots were made with datasets taken along traverses in the z direction. In addition, the aforementioned plots are also relatively insensitive to small spatial errors when making a traverse through the centerline since they all have zero rate of change at $z/(x-x_o) = 0$ (They all have a derivative of zero at the jet centerline). This is not true for the Reynolds shear stress. The Reynolds shear stress $\overline{u'v'}$ has a point of inflection at the centerline when the traverse is made in both the y and z directions. This means the centerline is the location where the rate of change of the shear stress is the maximum. As a result the shear stress plots are very sensitive to any spatial error when the centerline is being approached. This fact, combined with the wall and

92

enclosure effects, is a likely explanation for the nonzero shear stresses observed in Figure 5.5. It should also be noted that in Section 4.3 there was an asymmetry observed in the $\overline{u'^2}$ plots for the free jet case. At x/d=20 there was a 19% difference in peak $\overline{u'^2}$ values between the y and z traverses. Since the jet is axisymmetric, the $\overline{u'^2}$ plots for the y and z traverses should have been identical. The asymmetry in the enclosure boundary conditions could be the cause of this discrepancy as well.

5.3 Momentum Considerations

At an arbitrary distance x downstream from the jet exit, the momentum of a submerged circular jet can be expressed as

$$M_x = \int_0^\infty (2\pi\rho U^2)r\,dr \tag{5.1}$$

Using the above equation, the initial momentum of a turbulent jet is found to be

$$M_0 = \pi\ r^2\rho U_0^2 = \rho A_0 U_0^2 \tag{5.2}$$

The jet considered in this experiment has an exit Reynolds number of 2×10^4 with an exit velocity of 4.14 m/s. This yields an initial jet momentum of $M_0 = 0.337$ kg•m/s^2. At $x/d = 20$, for the case with no interior wall present, the momentum integral in Equation 5.1 can be evaluated to give $M_x = 0.178$ kg•m/s^2. This result suggests that at $x/d = 20$, the jet only has 53% of the momentum it had at the jet source. This drastic

93

decrease in jet momentum can be explained by the presence of the enclosure and the recirculation associated with an enclosed jet. The above calculation of momentum did not account for the momentum associated with the return flow re-circulating inside of the tank. If the jet was issuing into an infinite environment this correction would be unnecessary. This is because the flow surrounding the jet would be quiescent and would have no momentum associated with it. Since the sole source of momentum inside the tank is from the jet exit, and at $x/d = 20$ the jet only has 53% of its initial momentum, then the re-circulating flow must contain the other 47%. This treatment ignores second order contributions due to turbulence, pressure variations as well as viscous effects at the enclosure walls (all of which are considered negligible).

The momentum of the re-circulating flow can be shown to be $M_{recirc} = 0.159$ kg•m/s^2. Now that the momentum associated with the re-circulating flow is known, the velocity of the recirculation can be calculated as follows:

The cross sectional area of the tank is $A_T = 0.1575$m^2 when there is no interior wall present. For the case being considered here, $x/d = 20$, the jet has a diameter of $d = 34$mm and a cross sectional area of $A_x = 0.000908$ m^2. The area of the re-circulating flow can be determined by subtracting A_0 from A_T which yields

$$A_{recirc} = A_T - A_O = 0.1566m^2.$$

If the velocity of the re-circulating flow is assumed to be a constant, then Equation 5.1 can now be solved using A_{recirc} and M_{recirc} calculated above. Substituting into

94

Equation 5.1 yields $U_{recirc} = 0.032$m/s. The centerline velocity of the jet at $x/d = 20$ is

$U_c = 1.36$m/s. This means that the value of the re-circulating flow is only 2.3% of the

centerline jet velocity U_c. However, because the area of the re-circulating flow is so

large relative to the area of the jet, almost 50% of the jet's initially supplied

momentum is contained in the re-circulating flow by $x/d = 20$. This is a very

important result because it shows what a significant effect the enclosure has on a

confined jet in the near & intermediate field.

Another method that can be used to determine the average recirculation velocity

inside the tank would be to use the continuity equation in the x-direction. For the case

examined above, $x/d = 20$ with no interior wall present, the volume flow rate of the jet

can be calculated by integrating a polynomial curve fit of the velocity profile at

$x/d = 20$. The result obtained using this analysis is a recirculation velocity of

$U_{recirc} = 0.045$ m/s. The difference in recirculation velocity between the two different

methods can be attributed to the pressure terms which were neglected when the

momentum integral was evaluated. These pressure terms do not necessarily remain

constant throughout the tank due to the change in hydrostatic head inside the tanks

due small waves on the top surface of the enclosure.

In HCG94 a similar analysis was used to determine how confined a jet was by its

surrounding enclosure. In their analysis, at an arbitrary downstream distance, the area

of the jet was neglected. In the preceding paragraph the area of the jet is

$A_x = 0.000908$ m^2 and the area of the tank is $A_T = 0.1575$m^2 which gave a

95

recirculation area of $A_{\text{recirc}} = 0.1566\text{m}^2$. Thus the approximation of $A_{\text{recirc}} = A_{\text{T}}$ is valid.

For a self-similar jet their method of analysis yielded the following formula

$$\frac{M_x}{M_0} = \left[1 + \frac{16}{\pi B^2}\left(\frac{x}{D}\right)^2 \frac{A_0}{A_{recirc}}\right] \tag{5.3}$$

5.4 Eddy Viscosity

The laminar shear stress in Newtonian fluids can be expressed as

$$\tau = \rho\upsilon\frac{dU}{dy} \tag{5.4}$$

Turbulent shear stress can be expressed in a form similar to Equation 5.4. Boussinesq was the first to propose the idea of using a turbulent counterpart for the kinematic viscosity in Newton's equation. Boussinesq applied the idea of a virtual eddy viscosity to the Reynolds shear stress equation and obtained the following

$$\tau = -\rho\overline{u'v'} = \rho K_m \frac{dU}{dy} \tag{5.5}$$

where K_m is the eddy viscosity. The equation in its above form isn't readily usable because the eddy viscosity is not a physical property of the fluid but a value that needs to be determined experimentally. In 1942 Prandtl introduced the idea that the turbulent eddy viscosity should remain constant across a *free* turbulent flow. Prandtl expressed eddy viscosity as

$$K_m = cb(U_{\max} - U_{\min}) \tag{5.6}$$

96

where c is a constant that is experimentally determined and b is the width of the jet at the cross section being studied. This equation is convenient because the eddy viscosity is independent of y. Thus the eddy viscosity should remain constant over every cross section inside a free turbulent jet. For a jet in quiescent surroundings, $U_{min} = 0$. The width of a jet typically grows like $b \sim x$ and $U_{max} \sim 1/x$. When substituted into Equation 5.6 the following can be seen:

$$K_m \sim cx(x^{-1} - 0) \sim c, \tag{5.7}$$

Thus the eddy viscosity should remain constant across a free turbulent jet. The eddy viscosity (K_m) in Figure 5.7 was calculated using the following formula

$$K_m = \frac{-\overline{u'v'}}{\dfrac{dU}{dy}} \tag{5.8}$$

The data in Figure 5.7 is in good agreement with the assumption that eddy viscosity is independent over the entire width of the jet. The fluctuation in K_m at $y = 0$ is caused by a discontinuity in Equation 5.8 at $y = 0$. This is because at the origin $\dfrac{dU}{dy} = 0$ which causes a discontinuity since it is the denominator of Equation 5.8

The uniform nature of the eddy viscosity in Figure 5.7 suggests the jet, even though confined by the enclosure, still shares properties with free turbulent flows. The jet

97

studied in this thesis was found to conform well to Prandtl's hypothesis and Equation 5.3 above. This is surprising because Prandtl's suggested that eddy viscosity should remain constant across a *free* jet. Given the considerable effects of the enclosure on the jet seen in the previous section, it is interesting that this idea is still valid.

5.5 Swirling Flow Field

Figure 4.4, a plot of normalized Reynolds shear stress along a traverse in the z-direction, has a very unusual shape. The two-maxima and two-minima that are clearly evident in the near field (potential core region) of the jet require further discussion. As stated in Chapter 3 of this thesis, most velocity measurements in this experiment were taken in the x-y plane across the jet traversing in the z-direction. This was necessary due to the physical limitations of the experimental apparatus.

Normalized plots of the average stream wise velocity, U, were presented in detail in Chapter 4. Now let us consider a plot of the normalized cross stream velocity, V, along traverses in both the y and z directions. Figure 5.8 shows a plot of U and V made along a traverse in the y direction. It can be seen from the figure that there is a small negative value for V in the region above the jet centerline and a small positive value for V below the jet centerline. This is to be expected and shows that the surrounding fluid is being entrained into the jet with an entrainment coefficient, α, of $\alpha = 0.03$ where α is the entrainment velocity, $V_{entrain}$, normalized by the centerline velocity, U.

98

Figure 5.9 is a plot showing U and V taken along traverses in the z direction. The cross stream velocity, V, should be close to zero at the jet exit because this traverse was taken along the z direction. This is clearly not the case. The profile of V is positive for $z > 0$ and negative for $z < 0$. This result is not caused by entrainment but by mild swirl in the jet as it exits the nozzle into the tank.

The magnitude of the swirl present in a turbulent jet is measured by a dimensionless number referred to as the jet mean swirl number, S. The swirl number can be thought of as the ratio between the axial flux of angular momentum and the axial flux of axial momentum, and can be expressed as

$$S = \frac{G_\theta}{\left(\dfrac{d}{2}\right)G_x}$$
(5.9)

where G_θ is the axial flux of angular momentum defined by

$$G_\theta = \int (\rho UV + \overline{\rho u'v'})r^2 dr ,$$
(5.10)

G_x is the axial flux of axial momentum defined by

$$G_x = \int (\rho U + \overline{\rho u'^2} + (p - p_\infty))r dr$$
(5.11)

99

and d is the exit diameter of the jet nozzle. This particular definition of swirl number is hard to measure experimentally so simplifications are often made. One simplification is to treat the flow as a solid body undergoing rotation at the nozzle. Another simplification is to ignore the Reynolds stress terms. This leads to the following simplified expression for swirl number

$$S = \frac{F/2}{1-(F/2)^2} \qquad (5.12)$$

where F is the ratio of the maximum tangential velocity to the maximum axial velocity at the jet exit. Equation 5.12 can now be written in terms of U and V to give

$$S = \frac{V/2U}{1-(V/2U)^2} \qquad (5.13)$$

which is valid for jets with mild amounts of swirl ($S < 0.2$). In Figure 5.9 the maximum value of V is 0.25m/s and the maximum value of U is 4.14 m/s. Substitution into Equation 5.13 results in a swirl number of $S = 0.03$. Since this result is less than 0.2 using the simplified version of the swirl number formula was valid.

5.6 Source of Swirl

Measurements at the jet exit were taken with the flow straightener removed from the settling chamber inside of the nozzle and the results are presented in Figure 5.10. The flow straightener that was used consisted of pieces of plastic tubing wrapped together

100

into a bundle. The inside diameter of an individual piece of tubing was 4mm and the length of the pieces was 25mm. This results in an *L/d* ratio for the individual flow straightening elements of *L/d* ~ 6.25.

It can be seen from Figure 5.10 there is no appreciable reduction in the amount of swirl present at the exit of the nozzle. This result was not anticipated. It was thought that with the flow straightener removed from the settling chamber, the swirl present in the flow would have increased dramatically. This result suggests the swirl in the flow was not caused by swirl upstream of the nozzle. If the swirl at the jet exit was caused by swirl upstream from the nozzle, the presence of the flow straightening element should have reduced the magnitude of the swirl at the jet exit. This did not happen.

The nozzle that was used to create the jet studied in this thesis had an area contraction ratio of 100:1. The inlet of the nozzle settling chamber had a diameter of 50mm while the outlet of the nozzle had a diameter of 5mm. The piping connecting the pump to the settling chamber was 25mm in diameter. A flow diffuser wasn't used to gradually increase the diameter of the piping from 25mm up to 50mm. It is felt this could have been a cause of the swirl present at the jet exit. Given the velocities involved, it is possible that when the water exited the 25mm piping into the nozzle assembly a jet was formed inside of the nozzle itself. This jet then deflected towards one side of the nozzle and, as it entered into the nozzle contraction, began to swirl as it was accelerated inside the contraction. This hypothesis is consistent with the lack of function found with the flow straightener upstream of the nozzle. A schematic

101

representation of this hypothesis is shown in Figure 5.11 and is explained mathematically below.

First we must start with a general statement of the vorticity equation in vector notation

$$\frac{D\omega}{Dt} = \omega \circ \nabla v + v \nabla^2 \omega \tag{5.14}$$

The second term on the right hand side of Equation 5.14 represents the net rate of viscous diffusion of vorticity. The first term of Equation 5.14 represents the generation (or destruction) of vorticity by the stretching or turning of vortex lines. This particular term will now be discussed in detail.

The term $\omega \circ \nabla v$ in Equation 5.14 represents the generation of vorticity by the stretching or turning of vortex lines. This 'turning' idea can also be thought of as the tipping of vorticity from one direction into another. The $\omega \circ \nabla v$ term will now be expanded to better explain this tripping phenomenon. This explanation will neglect viscous effects (the $v \nabla^2 \omega$ in Equation 5.14 will be neglected for simplicities sake). Vorticity in the x direction can now be represented by

$$\frac{D\omega_x}{Dt} = \omega_x \frac{\partial u}{\partial x} + \omega_y \frac{\partial u}{\partial y} + \omega_z \frac{\partial u}{\partial z} \tag{5.15}$$

102

The term $\omega_x \dfrac{\partial u}{\partial x}$ represents the intensification of vorticity due to stretching of a vortex line. It is evident that vorticity increases when $\dfrac{\partial u}{\partial x} > 0$; which is the case when streamlines are converging. A good example of this occurs is inside of a nozzle. This increase in vorticity is due to the conservation of angular momentum. The other terms in Equation 5.15 are $\omega_y \dfrac{\partial u}{\partial y}$ and $\omega_z \dfrac{\partial u}{\partial z}$. These two terms show how vorticity in the y and z directions can create vorticity in the x direction due to the angular strain terms $\dfrac{\partial u}{\partial y}$ and $\dfrac{\partial u}{\partial z}$ that are present. These terms can have a significant magnitude in a flow with a non-uniform velocity profile. This lends further credibility to the hypothesis that the swirl in the flow is an artifact of the jets settling chamber. If there was a strong asymmetry in the flow profile upstream of the nozzle, this asymmetry could generate x direction vorticity (swirl) due to the stretching & angular straining of vortex lines inside the nozzle contraction.

It is widely accepted that swirl present in a jet enhances entrainment, lateral growth as well as velocity decay. However, these same properties of a jet are also affected by the presence of an enclosure or an adjacent wall. The issue that must now be addressed is how much the swirl affected the jet studied in this experiment.

5.7 Effect of Swirl on Jet Development

When a jet exits the nozzle the shear layer formed between the jet and the surrounding fluid rolls up and forms ring shaped vortices. These vortices travel with

103

the flow, growing in size, until they become unstable and break apart. When a jet has an azimuthal velocity component (swirl) these roll up vortices become unstable much sooner than when a jet isn't swirling. The break-up of these vortices increases the entrainment into the jet and promotes growth in the lateral direction.

A jet with a swirl number of $S = 0.0302$ is considered to have a very weak amount of swirl (Chevier and Chervinsky 1967). Since the measurements taken in this thesis were in the near field of the jet, and the Swirl number associated with the flow is very low, it is felt the swirl did not have an appreciable effect on the development of the jet in this thesis. However, this is not to say the swirl had no effect on the jet being studied, but rather in the near field the effects of the swirl would not yet have been realized.
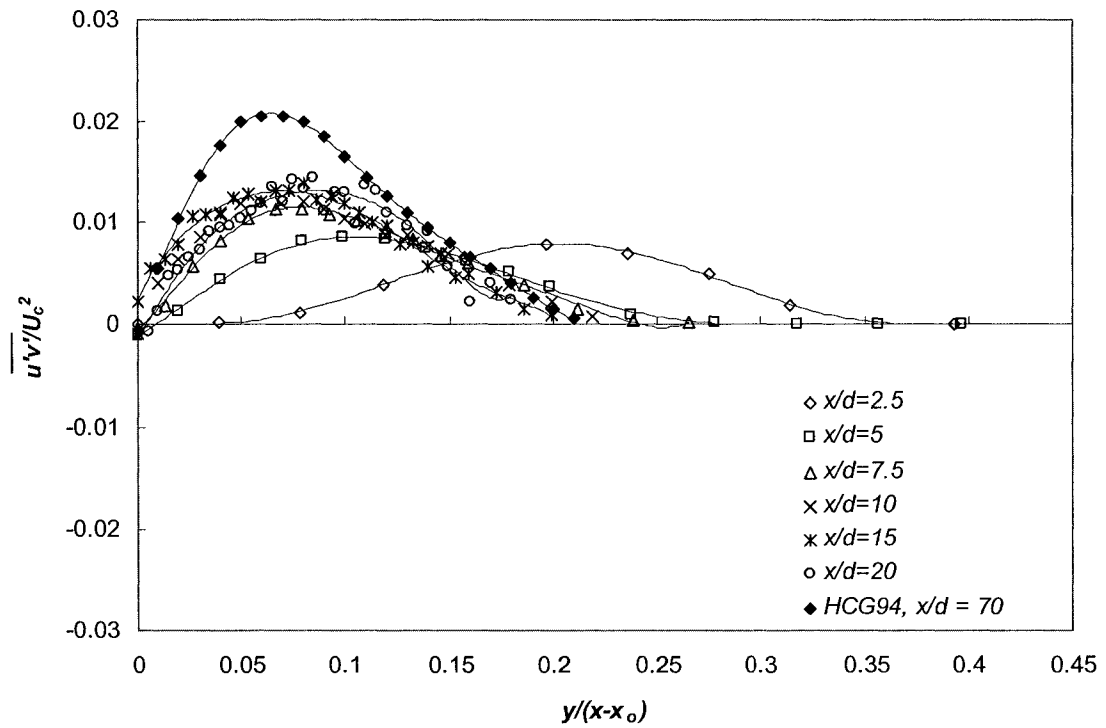
Figure 5.1: A normalized plot of Reynolds shear stresses including data taken by Hussein, Capp and George (1994). This dataset was taken with the interior wall removed from the enclosure along a y traverse. Points connected for visual continuity.
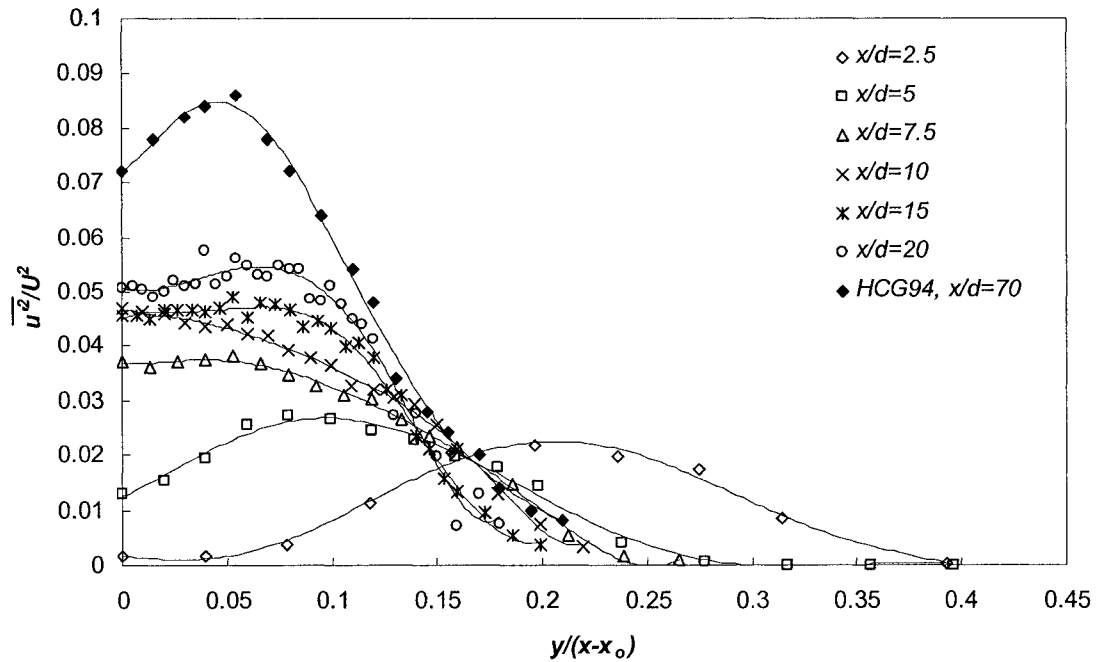
105

Figure 5.2: Normalized plot of axial normal stress $\overline{u'^2}$. This plot includes data taken by Hussein, Capp and George (1994). The datasets used in this plot were taken with the interior wall removed and along a traverse in the y direction. Points connected for visual continuity.
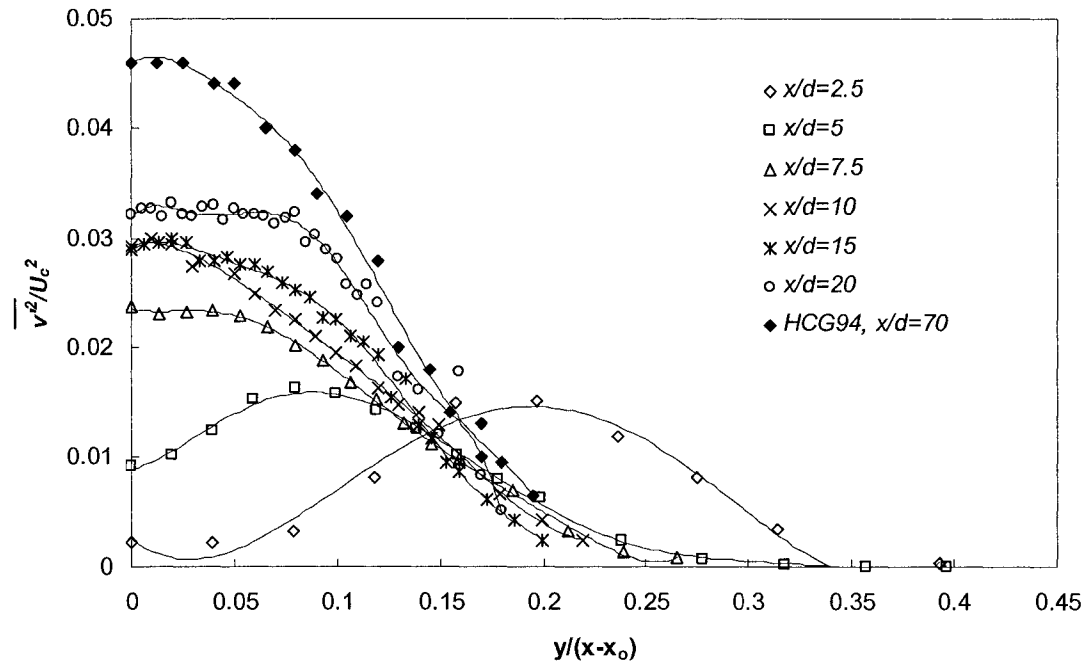
Figure 5.3: A normalized plot of $\overline{v'^2}$ with data from Hussein, Capp and George (1994) included. This data was taken with interior wall removed. Points connected for visual continuity
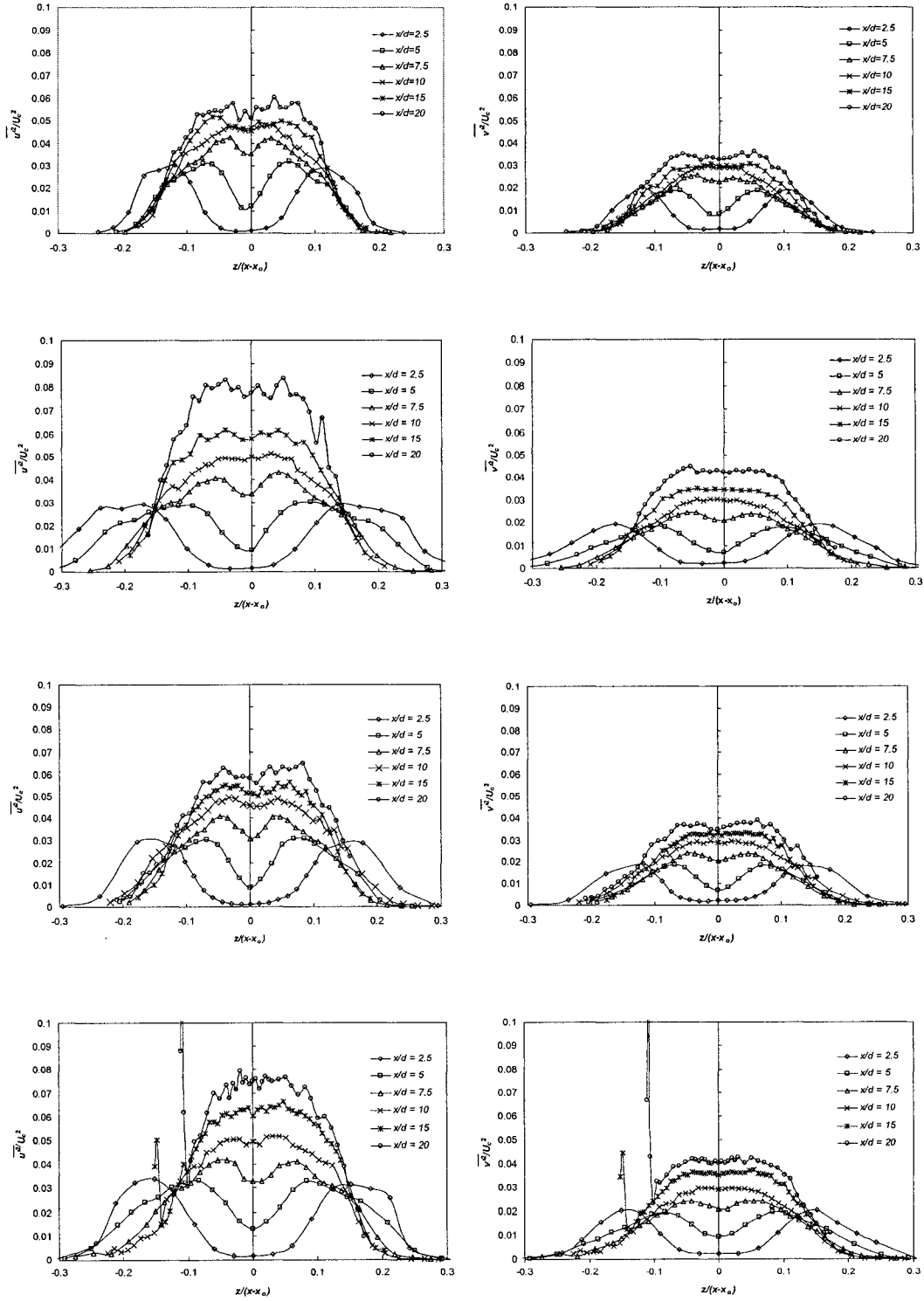
107

Figure 5.4: Plots of Reynolds normal stresses. From top to bottom, wall locations: no wall, $h = 10d$, $5d$ and $2.5d$. Points connected for visual continuity.
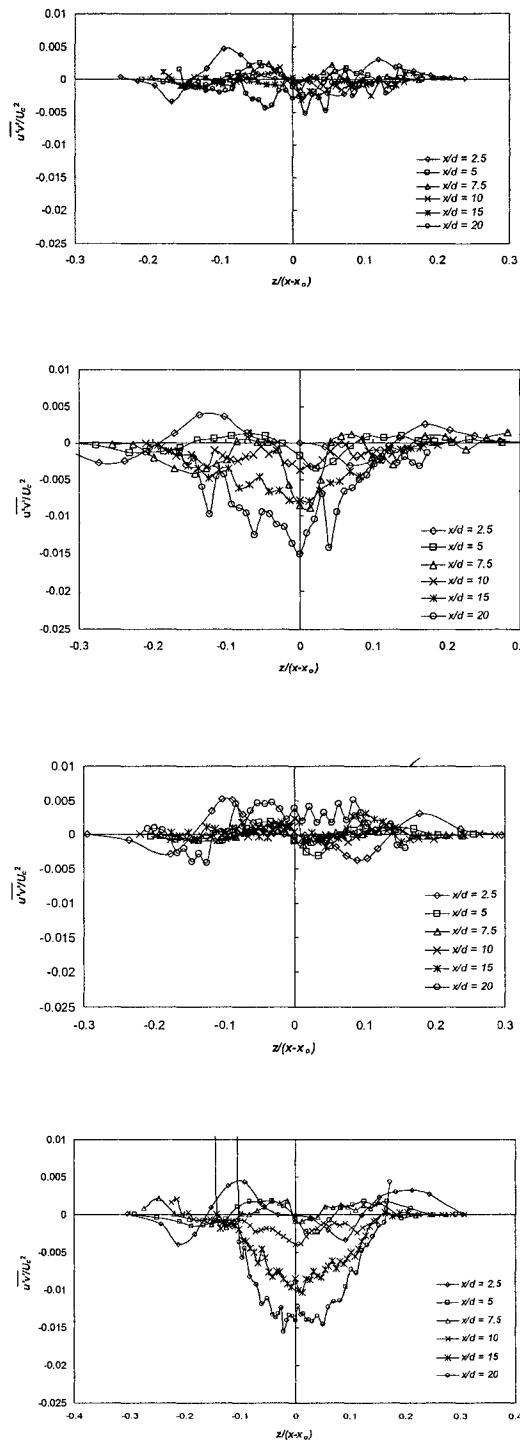
108

Figure 5.5: Normalized plots of Reynolds shear stress taken along a z traverse. From top down the interior wall is located at the following position: no wall, h=10d, 5d and 2.5d. Points connected for visual continuity.
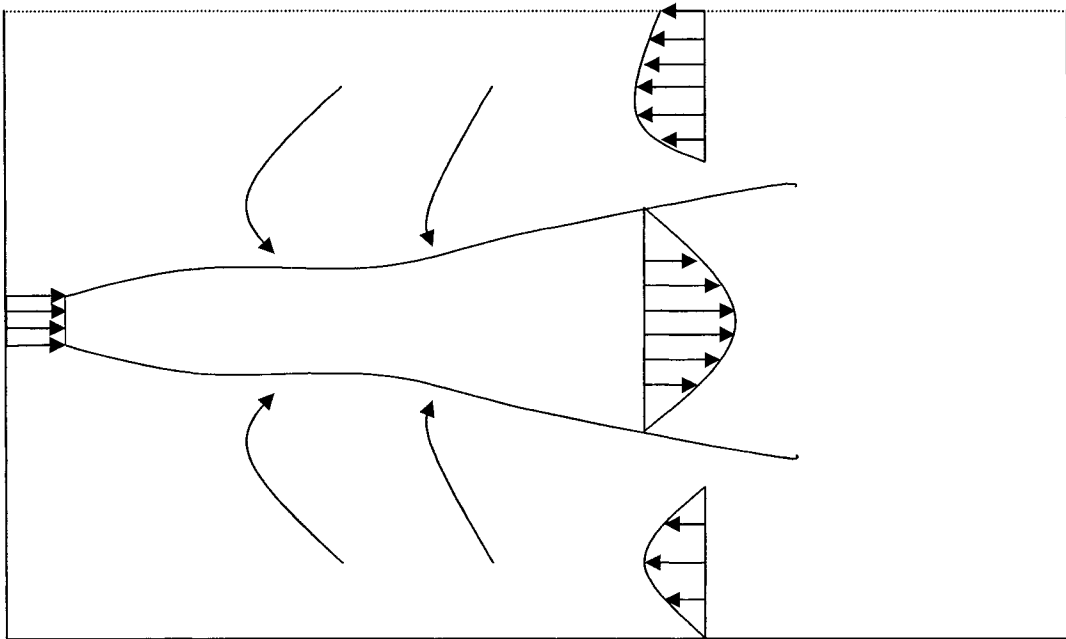
109

Figure 5.6: A modified version of Figure 1.3. This schematic shows the asymmetrical boundary conditions inside the enclosure.
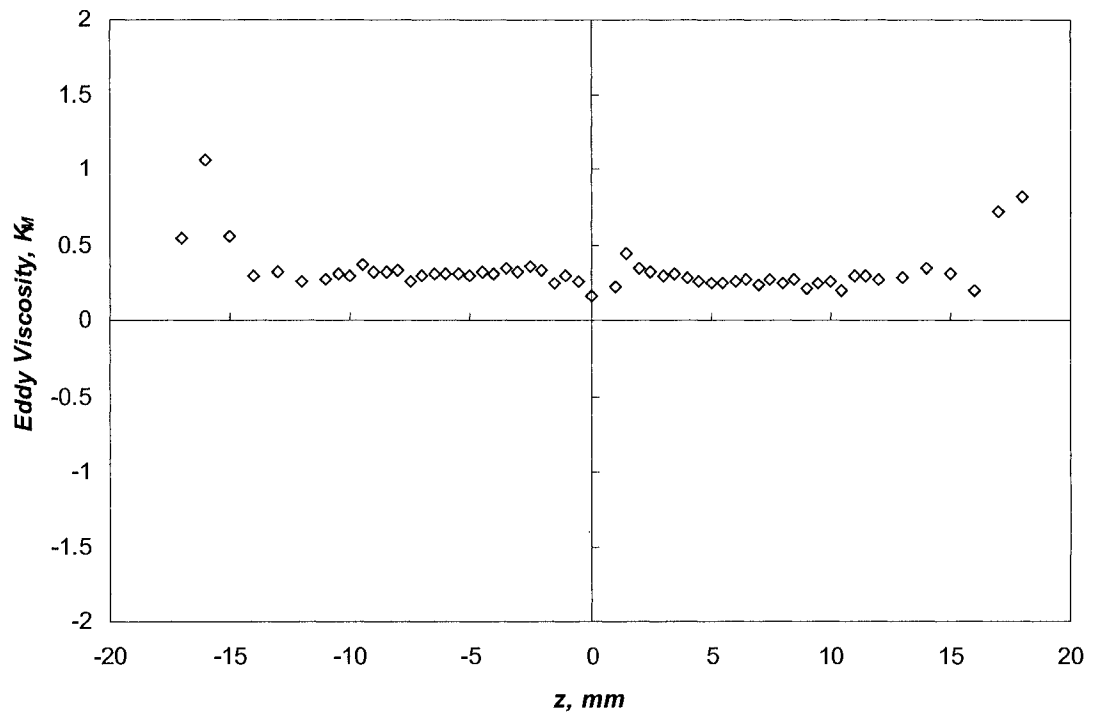
110

Figure 5.7: A plot of eddy viscosity with the wall located at h/d = 10 along a

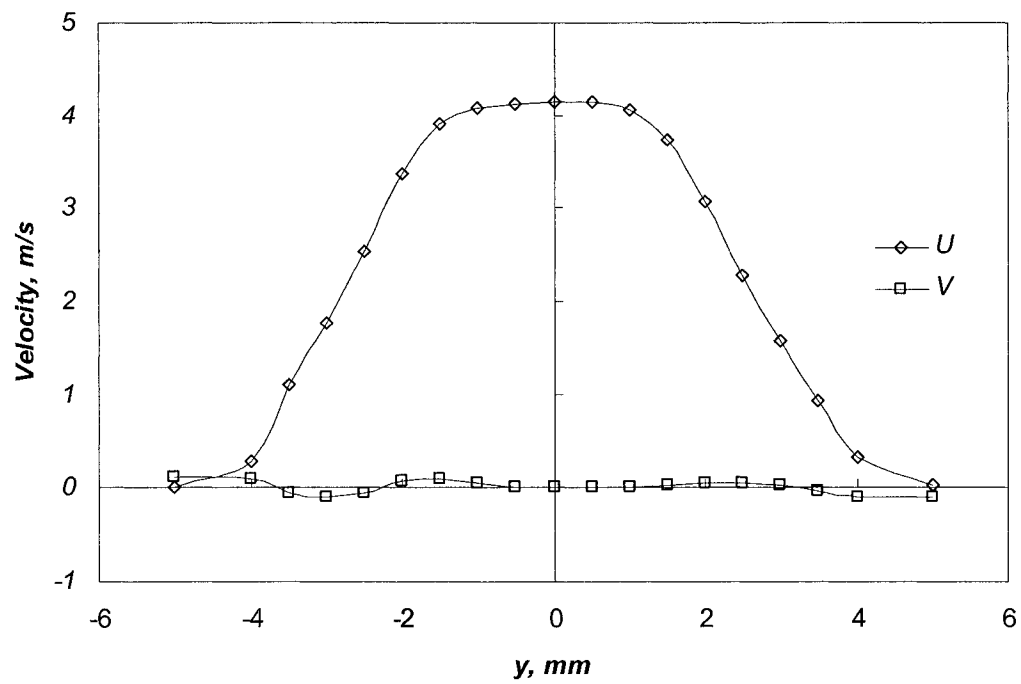traverse in the z-direction. The downstream distance is x/d = 15

111

Figure 5.8: A plot of U and V taken along a traverse in the y-direction at a downstream distance of $x/d = 2.5$. Points connected for visual continuity.

112
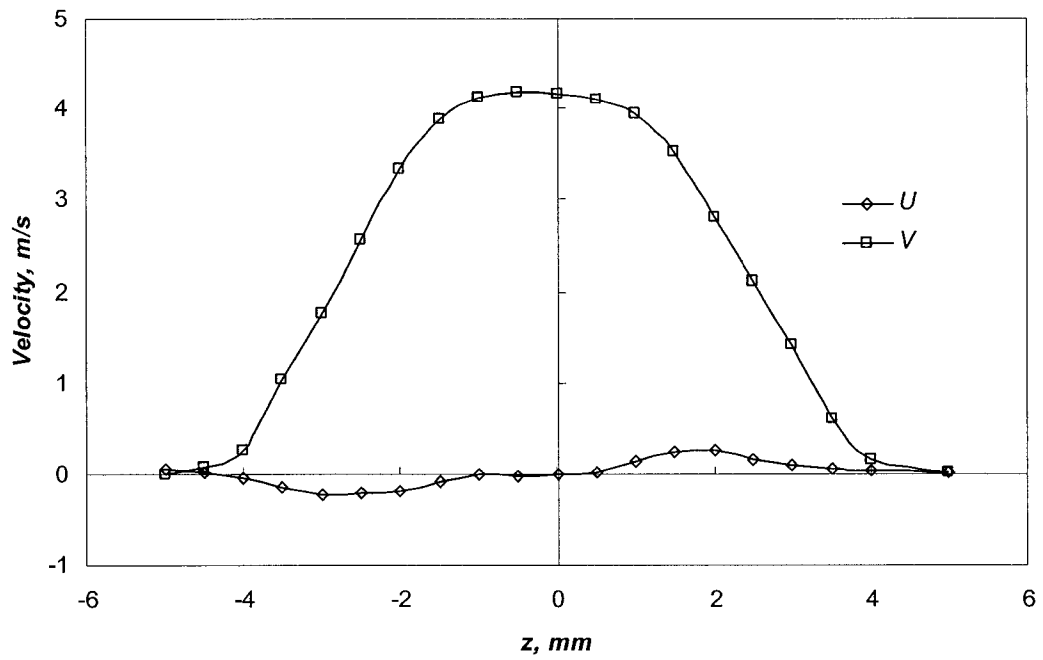
Figure 5.9: A plot of U and V taken along a traverse in the z-direction at a downstream distance of $x/d = 2.5$

113
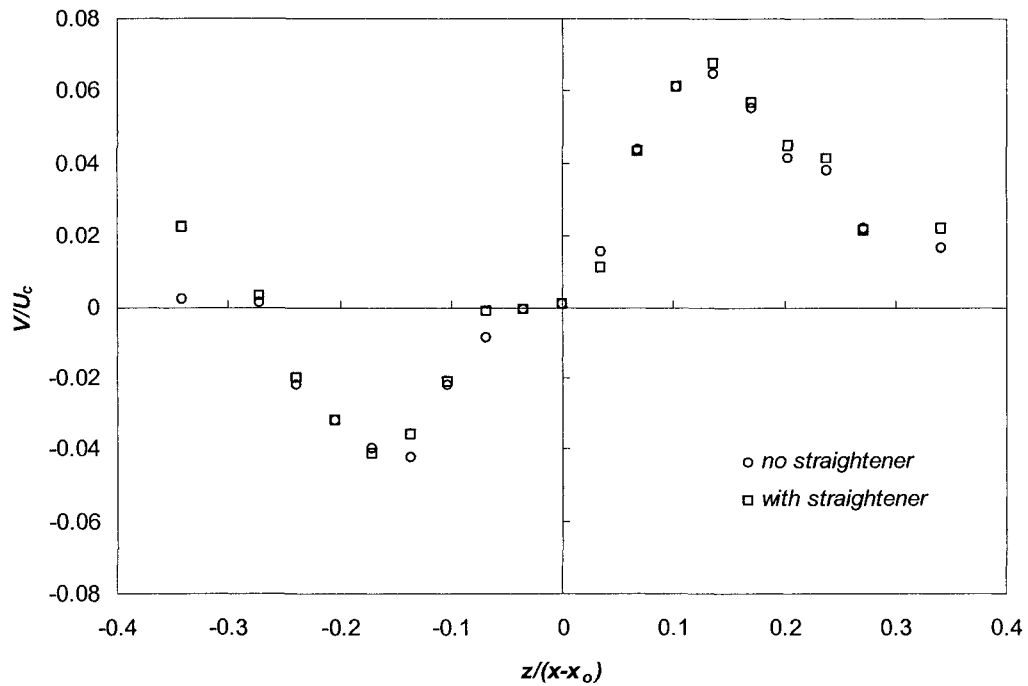
Figure 5.10: A plot of *V/Uc* taken with and without the flow straightening element present. It can be seen that the flow straightener has no significant effect on reducing the swirl present in the flow exiting the nozzle. This data was taken at a downstream location of x/d = 2.5

114

screen   flow element

Figure 5.11: A schematic representation of how a jet formed at the inlet to the nozzle settling chamber and caused swirl at the jet exit.

115

Chapter 6: Conclusions

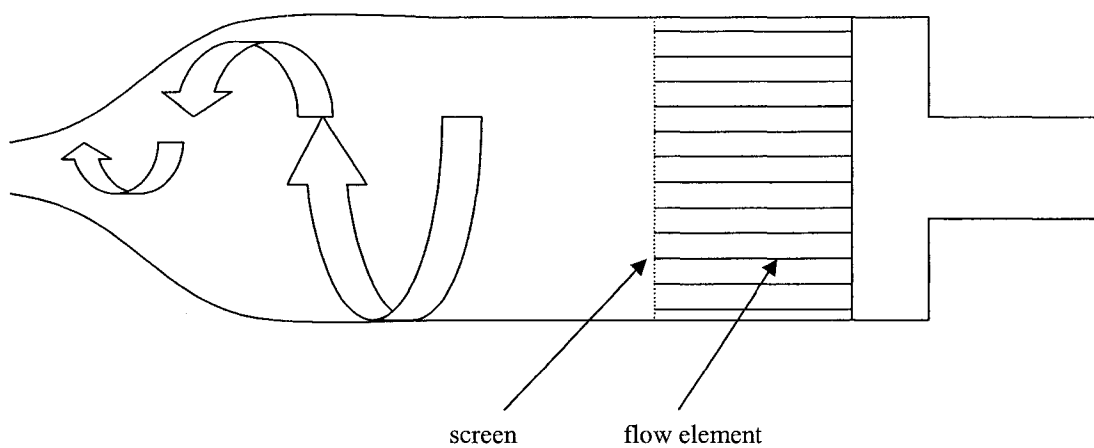LDA measurements of the near field (2.5 $\leq x/d \leq 20$) of a turbulent jet inside an enclosure were taken. The aim of taking these measurements was to use them as a benchmark in future research projects.

1.0   The second order moments obtained when the moveable interior wall of the enclosure was removed were consistently smaller than the results obtained by other researchers. This suggests that the geometry of the enclosure can have an effect on jet development even in the near and intermediate field of the jet.

2.0   The jet studied in this experiment did not satisfy the integral momentum conservation equation. This result was attributed to the re-circulation which was caused by the enclosure. Even in the near field it was found that the jet lost half of its initial momentum to the flow recirculation.

3.0   The turbulent eddy viscosity of the confined jet studied in this thesis was found to be constant across the jet. This is consistent with free jet theory. The jet studied in this thesis shared characteristics with both free and confined jets.

4.0   It was also found the presence of the wall had an effect on jet spreading as close as $x/d = 5$. The effects were not dramatic, but it was clear the presence of an adjacent wall does promote jet growth in the near field.

5.0 The swirl that was found in the jet at the exit of the nozzle is thought to be an artifact of the nozzle itself. More specifically it is due to vorticity in the y and z directions being accelerated in the nozzle contraction and bending into vorticity in the x direction at the jet exit. The effect of the swirl ($S = 0.03$) on the jet development in the near field is though to be insignificant.

6.0 The mean jet velocities studied in this thesis became self similar in the near field but the second order moments (Reynolds stresses) never followed suit. This is consistent with theory in that the second order moments become self similar well after the mean velocity components. It should also be stated that small inconsistencies in the enclosure boundary conditions should not be overlooked, especially when Reynolds shear stresses near the centerline are of interest. This is because the centerline is where the Reynolds shear stress has its maximum rate of change. As a consequence of this, shear stress measurements are very sensitive to small spatial errors in determining where the jet centerline is.

References

Adrian R.J. "Evaluation of laser Doppler velocimeter performance using Mie scattering theory" *Proc. Minnesota Symp. Laser Anemometry,* University of Minnesota, 1975.

Boersma, B.J. Brethouer, G. and Nieuwstadt, F. "A numerical investigation on the effect of the inflow conditions on the self-similar region of a round jet" *Physics of Fluids,* Vol 10, 1998 pp. 899-909

Bradbury, L. "The Structure of a self-preserving turbulent plane jet" *Journal of Fluid Mechanics,* Volume 23, 1965

Buchave, P. "The Accuracy of Flow Measurements by Laser Doppler Methods." Proceedings LDA-Symposium Copenhagen 1976

Chhabra, S. Shipman, T. and Prasad, A.K. "The entrainment behaviour of a turbulent axisymmetric jet in a viscous host fluid." *Experiment in Fluids* Vol 38, 2005 pp. 70-79

Chigier, N. and Chervinsky, A. "Experimental Investigation of Swirling Vortex Motion in Jets", *Journal of Applied Mechanics,* Vol 34, 1967, pp. 443 – 451

Craft, T.J and Launder, B.E. 2001 *"On the spreading mechanism of the three dimensional turbulent wall jet" Journal of Fluid Mechanics,* Vol 435, 2001, pp.305-326

Eriksson JG, Karlsson RI, and Persson J. "An Experimental Study of a Two Dimensional Plane Turbulent Wall Jet" *Experiments in Fluids,* Vol 25, 1998, pp.50-60

Ewing D, Hongguang S, 2002 "Development of Large Scale Structures in the Intermediate Region of the Three Dimensional Wall Jet" *2002 ASME Fluid Engineering Division Summer Meeting* July 14-18, 2002 Montreal Canada

Ewing, D. Benaissa, A. Pollard, A. "Contribution of Large structures to the anisotropic spread rate in a wall jet issuing from a round nozzle" *Abstract submitted to the Tenth International Symposium on Transport Phenomenon in Thermal Science and Process Engineering.*

Fukushima C, Aanen L, Westerweel J, "Investigation of the Mixing in an Axisymmetric Turbulent Jet Using PIV and LIF" *Proc.10th Int. Symp. on Applications of Laser Techniques to Fluid Mechanics* (Lisbon, Portugal) July 10-13, 2000. Paper 11.1

Glauser, M.N. "Coherent structures in the axisymmetric turbulent jet mixing layer." University of New York at Buffao, M.Sc Thesis, 1987

Hammad K.J, Shekarriz A, "Turbulence in Confined Axisymmetric Jets of Newtonian and non-Newtonian Fluids" 1998 ASME Fluids Engineering Division Summer Meeting, June 21-25, 1998 Washington DC, USA

Hess, S.L. "Introduction to Theoretical Meteorology" Holt Rinehart Winston. 1959

Hongguang S, Ewing, D. 2002 "Effect of Initial and Boundary Conditions on Development of Three-Dimensional Wall Jets" 2002 AIAA

Hussein H.J, Capp S.P, George W.K, "Velocity measurements in a high-Reynolds-number, momentum-conserving, axisymmetric, turbulent jet" *Journal of. Fluid Mechanics*, Vol 258, 1994, pp. 31-75

Kleppe, J.A. "Point Velocity Measurements." CRC Press Ltd 2000.
http://www.engnetbase.com

Morel, T. "Comprehensive Design of Axisymmetric Wind Tunnel Contraction". *Journal of Fluids Engineering*, Vol 97, 1975, pp. 225-233

Pani, B.S., Dash, R.N. "Three dimensional wall jets from circular outlets." *Proceedings of the Institution of Civil Engineers*, Vol 50, 1983, pp. 354-360

Panton, R.L. Incompressible Flow. Second Edition. John Wiley & Sons 1996

Patrick, W. "Error Sources in Laser Velocimeter Systems" Technical Report, University of Connecticut 1985

Rajaratnam, N. & Pani, B.S. "Three Dimensional Turbulent Wall Jets" Department of Civil Engineering, University of Alberta publication, 1970

Schlichting, H. Boundary Layer Theory. Sixth Edition. McGraw Hill 1968

Sforza, P.M and Herbst, G. "A study of three-dimensional, incompressible turbulent wall jets" *AIAA Journal* Vol 8, 1970, pp. 276-283

Tennekes, H. and Lumley, J.L. First Course in Turbulence. MIT Press, Cambrigde 1997

Stan, G. "Fundamental Characteristics of Turbulent Opposed Impinging" Jets University of Waterloo Thesis, 2000

Tatchie, M. Balachandar, R. Bergstrom, D. "Co-Flow and Counter-Flow Wall Jets: Current Status and Future Prospects", World Engineering Congress and Exhibition, Aerospace Engineering Session (Kuala Lumpur, Malaysia) 7 pages, July 19-22, 1999

Tropea, C. "Measuring Techniques in Experimental Fluid Mechanics" University of Waterloo. 1986

TSI Publication. "Laser Velocimetry...the Non-Invasive Flow Measurement Technique"

White, F.M. Fluid Mechanics. Fourth Edition. WCB McGraw Hill 1999

Wicker, R.B. and Eaton, J.K. "Near field of a coaxial jet with and without axial excitation", *AIAA Journal*, Vol 32, 1994, pp. 542-546

Westerweel, J. Hofmann, T. Fukushima, C. Hunt, J.C.R. "The turbulent / non-turbulent interface at the outer boundary of a self-similar jet" *Experiments in Fluids* Vol 33, 2002, pp. 873-878

Wygnanski, I. and Fiedler, H.E. "Some Measurements in the self-preserving jet" *Journal of Fluid Mechanics* Vol 38, 1969, pp. 577-612

Yue, Z. 2002 "An Experimental Investigation of Turbulent Wall Jets" ASHRAE Transactions: Research Vol 4512